STUDY OF WZ PRODUCTION WITH THE DØ DETECTOR

by

KETINO KAADZE

B.S., Tbilisi State University, 2003
M.S., Tbilisi State University, 2005

AN ABSTRACT OF A DISSERTATION

submitted in partial fulfillment of the
requirements for the degree

DOCTOR OF PHILOSOPHY

Department of Physics
College of Art and Sciences

KANSAS STATE UNIVERSITY
Manhattan, Kansas
2010

Abstract

In this Dissertation I present a detailed study of $p\bar{p} \to WZ$ production using fully leptonic decays of W and Z bosons with electrons and muons in the final state. Data used for the study were collected by the DØ detector at the Fermilab $p\bar{p}$ collider with a center-of-mass energy of $\sqrt{s} = 1.96$ TeV and correspond to 4.1 fb^{-1} of integrated luminosity. The most precise measurement of the WZ production cross section is obtained and found to be in a good agreement with the standard model prediction.

I also present a search for new phenomena in the WZ production by investigating the coupling between W and Z bosons and by searching for new charged particles that can decay into WZ boson pair. No evidence for new physics is found, and the most stringent limits are set on the anomalous WWZ coupling parameters and masses of charged resonances. This result also sets the stringest limit on one of the possible sources of electroweak symmetry breaking, a low-scale Technicolor with a typical heavy techni-pion hypothesis.

STUDY OF WZ PRODUCTION WITH THE DØ DETECTOR

by

KETINO KAADZE

B.S., Tbilisi State University, 2003
M.S., Tbilisi State University, 2005

A DISSERTATION

submitted in partial fulfillment of the
requirements for the degree

DOCTOR OF PHILOSOPHY

Department of Physics
College of Art and Sciences

KANSAS STATE UNIVERSITY
Manhattan, Kansas
2010

Approved by:

Major Professor
Yurii Maravin

Copyright

Abstract

In this Dissertation I present a detailed study of $p\bar{p} \to WZ$ production using fully leptonic decays of W and Z bosons with electrons and muons in the final state. Data used for the study were collected by the DØ detector at the Fermilab $p\bar{p}$ collider with a center-of-mass energy of $\sqrt{s} = 1.96$ TeV and correspond to 4.1 fb^{-1} of integrated luminosity. The most precise measurement of the WZ production cross section is obtained and found to be in a good agreement with the standard model prediction.

I also present a search for new phenomena in the WZ production by investigating the coupling between W and Z bosons and by searching for new charged particles that can decay into WZ boson pair. No evidence for new physics is found, and the most stringent limits are set on the anomalous WWZ coupling parameters and masses of charged resonances. This result also sets the stringest limit on one of the possible sources of electroweak symmetry breaking, a low-scale Technicolor with a typical heavy techni-pion hypothesis.

Table of Contents

List of Figures

List of Tables

Acknowledgments

I thank my mom and dad for their love and guidance in life. Thank you mom for supporting me throughout my studies in Georgia and my intentions to pursue degree Doctor of Philosophy in the United States. I express a gratitude to the whole family and many friends in Georgia who made my life there rich and full.

To my advisor, Yurii Maravin, thank you for introducing me to the field of high energy physics and for your patience and motivation in this process. I thank Yurii for invaluable guidance and direction throughout my graduate research at both CMS and DØ experiments, that resulted in number of successful achievements.

I owe a great debt of gratitude to the faculty members of High Energy Physics group at Kansas State University: Tim Bolton, Glenn Horton-Smith, Larry Weaver, Bharat Ratra, and Andrew Ivanov, for the support and numerous helpful advices.

I am grateful to all wonderful professors at Kansas State University and Tbilisi State University and teachers at school from whom I learnt a lot. They had a great impact on my development as a scientist.

I would like to thank my friends whom I met in the past several years while being at Kansas State University, Fermilab, and CERN. They have made my life at those places pleasant. The time spent with them will always be memorable.

My special thanks to my colleagues at the CMS experiment: Giovanni Franzoni, Seth Cooper, Stephanie Beauceron, Senka Djuric, Srecko Morovic, Vuko Brigljevic, and many others, for their help in my research at CERN. With them I worked on the commissioning of the CMS detector and learnt number of different data analysis techniques. Experience gained at the CMS experiment helped me to smoothly move to the DØ experiment. There, I owe a gratitude to many members of the DØ Collaboration for a guidance and suggestions in the data analyses. Those are Dmitry Bandurin, Alexey Ferapontov, Carrie McGivern, James Kraus, Andrew Askew, Thomas Gadfort, Rick Jesik, Marc Buehler, Heidi Schellman,

Junjie Zhu, Gustaaf Brooijmans, Arnaud Duperrin, Marco Verzocchi, and many others. I thank the Editorial Board, chaired by Marc Besancon, for reviewing my analyses and very useful discussions. I also thank all supporting entities at Kansas State University, Fermilab, and CERN for supplying the resources that made my graduate research possible.

Finally, there are many people not listed above who helped me to reach this point in my life and I would like to thank them all.

Dedication

To my mom and the memory of my dad.

Chapter 1

Introduction

The standard model (SM) is a fundamental theory of the elementary particle physics. It was developed in the early 1970's and describes the current understanding of the Nature combining the electromagnetic, weak, and strong interactions. The SM has been extensively tested during last four decades and found to be in an excellent agreement with the measurements and observations at different experiments. For this reason, the SM is considered as one of the biggest achievement in particle physics.

However, the SM is believed to be far from being complete. For example, the fourth and the last known fundamental force in the Nature, the gravitation, is not included in the SM. The model does not give an explanation to why there is three apparent copies of quarks and leptons, different only by mass. The standard model does not offer a candidate for a dark matter. It does not account for the recently observed neutrino mass and, moreover, does not explain such a wide variety of masses of fundamental particles. The corner stone of the mass generation in the SM is via interaction with the hypothetical Higgs boson, which quantum corrections has to be precisely tuned at 10^{-26} level. At last but not the least, the standard model is far away from being elegant. It has at least 19 free independent parameters the origin of which is not explained.

As a result, the standard model is considered of being a low energy approximation of a more general theory that describes the fundamental constituents and their interactions, just like the Newtonian mechanics was a low-energy approximation of a quantum mechanics.

Thus, many extensions of the SM has been developed that can explain some of the unresolved puzzles of the Nature.

Some of these models are a pure extension of the SM, assuming the existence of the Higgs boson, and with the Higgs mechanism being an explanation of the electroweak symmetry breaking (EWSB). While, the others develop different approach to explain EWSB without a need of a new scalar boson. However, most of the extension models rely on the gauge structure of the SM and allow the existence of the new resonances. To prove or disprove these extensions require an experimental input. A discovery of new physics, or phenomena beyond the SM predictions can lead scientists towards the more general model of the fundamental particles and their interactions.

This search for deviations can be done by either a careful study of the existing processes or by a search of new particles, not predicted by the SM. In this Dissertation, I describe a thorough and extensive study of one of the least explored area of the SM, the production of heavy gauge boson pair, WZ. The work is performed to test the electroweak sector of the SM, by measuring the production cross section, and search for the evidence of the non-SM production of gauge boson pair. This work results in the most precise measurement of the WZ boson production cross section and sets stringent limits on the parameters describing the coupling between heavy gauge bosons. It also provides very strong limits on new heavy hypothetical resonances decaying to the WZ boson pair, and exclude a large parameter phase space of one of the alternative to SM mass generation models, the Technicolor.

The outline of the thesis is as follows: in Chapter 2 I briefly introduce the SM, the mechanism of the SM WZ production, and discuss the different SM extensions predicting new heavy resonances that are used as benchmarks in my analysis. That is followed by Chapter 3, were the experimental apparatus is described. Different methods to identify WZ decay products are given in Chapter 4. The results on the WZ production cross section measurement, the constraints on WZ coupling parameters, and search for new resonances are given in Chapter 5, Chapter 6, and Chapter 7, respectively. Finally, the results of this

work are summarized in Chapter 8.

Chapter 2

Theoretical Background

2.1 The Standard Model

The standard model is a fundamental model described by the quantum field theory, that combines the quantum mechanics and the relativity. This model explains the interactions between the fundamental constituents of the Universe, so-called elementary particles. The SM is a gauge theory that implies the Lagrangian of the interaction is invariant under the local transformations. As a result, the SM interactions are described in terms of mathematical fields based on the gauge symmetry group $SU(3) \otimes SU(2) \otimes U(1)$, where the symmetry groups $SU(3)$, $SU(2)$, and $U(1)$ represent gauge fields for strong, weak, and electromagnetic interactions, respectively. The fourth and the last known interaction in the Nature, gravity, is not included in the SM and assumed to be negligible. Within the SM all fundamental particles are divided into two types: fermions and bosons.

Fermions

Fermions, half-integer spin particles, obey Fermi-Dirac statistics implying that more than one fermion can not occupy the same quantum state. The fermions are split into two groups, leptons and quarks, that make up the matter in the Universe.

The leptons and quarks are grouped in three families, or three generations. The particles across generations reveal identical properties with the exception of having different masses.

A typical family of fermions is comprised by the left-handed doublet of leptons, $\binom{\nu_l}{l^-}_L$, left-handed doublet of quarks, $\binom{q_u}{q_d}_L$, and right-handed singlets of antiparticles of charged leptons and quarks, $\bar{l}^+_R$, $\bar{q}_{uR}$, and $\bar{q}_{dR}$. Anti-particles have the same mass and spin as particles but opposite sign of all internal quantum numbers. The leptons having electric charge, *e.g.* electron (e), interact via the electromagnetic and the weak interactions, while ones being neutral, *e.g.* electron neutrino (ν_e), participate only in weak interaction. The quarks carry both electric and color charges. Thus, in addition to the electroweak interactions they also interact through the strong force. The electric charge of a quark is a fraction of an electron charge, e, either 2/3 (up-type quark) or 1/3 (down-type quark), while the color charge of a quark can be "red", "green", or "blue". That results in six left-handed quarks in each generation. Quarks cannot be found single, they are confined within a baryon (group of three quarks) or a meson (quark-antiquark pair). These systems are usually referred to as hadrons. An example of a very common baryon is a nucleus of a Hydrogen atom, a proton. Some of the properties of leptons and quarks are summarized in Table 2.1 and 2.2.

Generation	Lepton	Mass (MeV/c^2)	Charge (e)
first	e	0.511	-1
	ν_e	$< 2.2 \times 10^{-6}$	0
second	μ	105.65	-1
	ν_μ	<0.17	0
third	τ	1776.84	-1
	ν_τ	<15.5	0

Table 2.1: *The properties of leptons.*

Bosons

Fundamental interactions between elementary particles occur through the exchange of quanta of the SM gauge fields, spin-one gauge bosons. Bosons satisfy Bose-Einstein statistics that allows two or more bosons with the same quantum numbers such as energy, spin, *etc.* to occupy the same quantum state. Electromagnetic force carrier is a photon, γ, and it can interact with electrically charged particles, charged leptons, quarks, as well as other

Generation	Quark	Mass (MeV/c^2)	Charge (e)
first	u	0.003	2/3
	d	0.006	-1/3
second	c	1.3	2/3
	s	0.1	-1/3
third	t	175	2/3
	b	4.3	-1/3

Table 2.2: *The properties of quarks.*

charged gauge bosons that I describe below. The photon is massless, and therefore, the electromagnetic interactions have infinite range.

Weak interaction is mediated through three massive bosons, two charged bosons, $W^{\pm}$, responsible for a charged weak current, and a neutral boson Z^0, mediating a neutral weak current. Weak interaction happens between both leptons and quarks. It is the only interaction in the Nature changing the flavor of interacting particles. Due to relatively high masses of these bosons, the weak interaction fades rapidly with distance. For the strong interaction, there are eight massless, colored gluons, g. Since gluons carry color charge, they interact only between quarks and themselves. Although gluons are massless, the strong force range is not infinite. The strength of the strong force increases very rapidly with distances up to $\sim 10^{-15}$ m. At larger distances the strength becomes practically unobservable. Such property of strong force results in confinement of quarks in baryons and mesons (described above). The properties of the gauge bosons are summarized in Table 2.3.

Force	Carrier	Mass (GeV/c^2)	Charge (e)	Symmetry group
Electromagnetic	γ	0	0	$U(1)$
Weak	W^+	80.403	1	$SU(2)$
	W^-	80.403	-1	
	Z^0	91.188	0	
Strong	g	0	0	$SU(3)$

Table 2.3: *The properties of gauge bosons.*

Higgs Boson

The remaining particle in the SM is a neutral, spin-zero scalar particle, the Higgs boson. The Higgs boson is a quanta of a so-called Higgs field that has a non-zero expectation value at each point in space. Interactions with this non-zero field result in the origin of mass for elementary particles, including the Higgs boson itself. This mechanism of mass generation, usually referred to as Higgs mechanism, is the simplest way of forming a gauge theory with massive gauge bosons, W and Z^0, while keeping the photons and gluons massless.

Despite the simplicity, the Higgs mechanism has several drawbacks. One of them is usually referred to as a hierarchy problem: the mass of the Higgs boson must be light, but quantum corrections are quadratically divergent with energy, and therefore the model must by fine-tuned to work at high energies. Despite the number of direct and indirect experimental searches the Higgs boson is not discovered yet. This leaves the question of the origin of the electroweak symmetry breaking unanswered and drives much of the experimental research in the field of high energy physics.

2.2 WZ production

The electroweak interactions are based on the $SU(2) \otimes U(1)$ symmetry group described by the Lagrangian, $\mathcal{L}_{EWK}$, given in Eq. 2.1.

$$\mathcal{L}_{EWK} = \mathcal{L}_{gauge} + \mathcal{L}_{\phi} + \mathcal{L}_{f} + \mathcal{L}_{Yuk} \tag{2.1}$$

Here, $\mathcal{L}_{\phi}$ describes a scalar field, Higgs fields, of the electroweak interactions, $\mathcal{L}_{f}$ stands for interactions between three families of left-handed fermions and right-handed antifermions. The last term, $\mathcal{L}_{Yuk}$, describes the Yukawa interactions, interactions between the scalar field and fermions. The $\mathcal{L}_{gauge}$ term in Eq. 2.1 gives rise to couplings among the gauge fields and is represented as follows

$$\mathcal{L}_{gauge} = -\frac{1}{4} W^{i}_{\mu\nu} W^{\mu\nu i} - \frac{1}{4} B_{\mu\nu} B^{\mu\nu}, \tag{2.2}$$

where

$$W^i_{\mu\nu} = \partial_\mu W^i_\nu - \partial_\nu W^i_\mu - g\epsilon_{ijk} W^j_\mu W^k_\nu \tag{2.3}$$

$$B_{\mu\nu} = \partial_\mu B_\nu - \partial_\nu B_\mu \tag{2.4}$$

In these equations, W^i_μ $(i = 1, 2, 3)$ and B_μ represent $SU(2)$ and $U(1)$ fields, respectively and g is $SU(2)$ coupling constant. The electroweak bosons are the combinations of these fields:

$$W^\pm_\mu = \frac{1}{\sqrt{2}}(W^1_\mu \mp W^2_\mu) - The\ W^\pm\ boson \tag{2.5}$$

$$Z_\mu = -sin(\theta_W)B_\mu + cos(\theta_W)W^3_\mu - The\ Z^0\ boson \tag{2.6}$$

$$A_\mu = cos(\theta_W)B_\mu + sin(\theta_W)W^3_\mu - The\ \gamma\ photon \tag{2.7}$$

where, θ_W is the Weinberg angle and describes the relation between the $SU(2)$ and $U(1)$ couplings, g and g':

$$cos(\theta_W) = \frac{g}{\sqrt{g^2 + g'^2}} \tag{2.8}$$

As seen above, due to the gauge part of the electroweak Lagrangian, Eq 2.1, both triple and quadrupole couplings among the gauge fields are allowed with a requirement that at least two charged weak bosons are present. The $SU(2)$ symmetry group does not allow vertices with only Z bosons and photons.

Therefore, within the SM the WZ boson pair can be produced at the leading order (LO) via so-called t-, u, and s-channels. The Feynman diagrams describing this production are shown in Fig. 2.1. In the case of t- and u-channels, the W and Z bosons are radiated from initial state quarks and the production is fully described by boson to fermion couplings. These couplings are measured with a good precision by studying the single production of the W and Z bosons[1]. The s-channel production occurs via the triple gauge boson vertex. If only t- and u-channels would be used the production cross section would rise linearly

with an increase of the partonic center-of-mass energy, $\sqrt{\hat{s}}$ [1]. This means that at sufficiently high energies the probability for these processes would exceed 100%, *i.e.*, results become unphysical. This is often referred to as a violation of unitarity. The production of the WZ boson pairs via s-channel interfere with t- and u-channels and maintain the unitarity at high energies. Furthermore, s-channel production of WZ pairs allows us to measure the couplings between W and Z gauge bosons, so-called triple gauge couplings (TGC) which are precisely predicted in the SM. Unlike boson to fermion couplings, the triple gauge couplings are less precisely measured due to a relative rarity of the diboson production [2].

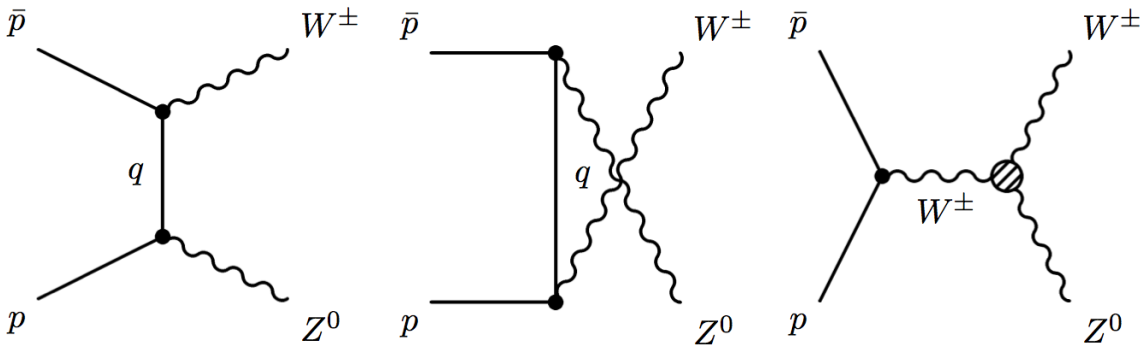

Figure 2.1: *Tree level Feynman diagrams of WZ production. t-, u-, and s-channel diagrams are given in the left, center, and right, respectively. The s-channel diagram contains the trilinear WWZ gauge boson vector vertex.*

With an assumption that there are new physics processes contributing to the WWZ vertex, it is desirable to express this interaction in a model independent manner by introducing a generalized Lagrangian[2,3] given below

[1]The $\sqrt{s}$ notation is used for the center-of-mass energy of two colliding beams, *e.g.* $\sqrt{s} = 1.96$ TeV for proton-antiproton beams at the Tevatron. However, since proton and antiproton are composite particles, the collision happens between constituents of protons, *i.e.* quarks, gluons, and their antiparticles. Those are often referred to as partons and carry only some fraction of the initial momenta of proton and antiproton. Thus, the center-of-mass energy of colliding partons is not constant, and is called partonic center-of-mass energy, noted as $\sqrt{\hat{s}}$.

[2]The first observation of the WZ production at Tevatron was done in 2007.

$$
\begin{aligned}
\mathcal{L}_{WWZ}/g_{WWZ} = & ig_1^Z(W^\dagger_{\mu\nu}W^\mu Z^\nu - W^\dagger_\mu Z_\nu W^{\mu\nu}) \\
& + i\kappa_Z W^\dagger_\mu W_\nu Z^{\mu\nu} \\
& + \frac{i\lambda_Z}{M_W^2} W^\dagger_{\rho\mu} W^\mu_\nu Z^{\nu\rho} \\
& - g_4^Z W^\dagger_\mu W^\nu(\partial^\mu Z^\nu + \partial^\nu Z^\mu) \\
& + g_5^Z \epsilon^{\mu\nu\rho\sigma}(W^\dagger_\mu \partial_\rho W_\nu - W_\nu \partial_\rho W^\dagger_\mu) Z_\sigma \\
& + \tilde{\kappa_Z} W^\dagger_\mu W^\nu \tilde{Z}^{\mu\nu} \\
& + \frac{i\tilde{\lambda}_Z}{M_W^2} W^\dagger_{\rho\mu} W^\mu_\nu \tilde{Z}^{\nu\rho},
\end{aligned}
\tag{2.9}
$$

where $W_{\mu\nu} \equiv \partial_\mu W_\nu - \partial_\nu W_\mu$, $Z_{\mu\nu} \equiv \partial_\mu Z_\nu - \partial_\nu Z_\mu$, $\tilde{Z}^{\mu\nu} \equiv \frac{1}{2}\epsilon_{\mu\nu\rho\sigma} Z^{\rho\sigma}$, and g_{WWZ} is defined as an overall WWZ coupling and is equal to $-ecot(\theta_W)$. Here, W^μ, Z^μ, and θ_W are the same as defined in Eqs. 2.5, 2.6, and 2.8.

There are seven coupling parameters in Eq. 2.9. Their SM values are $g_1^Z = \kappa_Z = 1$ and $\lambda_Z = g_4^Z = g_5^Z = \tilde{\kappa}_Z = \tilde{\lambda}_Z = 0$. Commonly only the coupling parameters conserving C, P, and CP operations, *i.e.* operations that conserve the symmetry between particles and antiparticles are considered, and this assumption is assumed in this Dissertation as well. This leaves only three out of seven coupling parameters, g_1^Z, κ_Z, and λ_Z, and 2.10 notation is used to describe the deviations from the SM predictions.

$$
\Delta g_1^Z \equiv g_1^Z - 1,\ \Delta\kappa_Z \equiv \kappa_Z - 1,\ \lambda_Z \tag{2.10}
$$

If coupling parameters have non-SM values, new physics is required to keep the gauge boson production from unitarity violation at high energy. A typical way to control the high energy behavior is to introduce the dipole form-factor scale Λ in the description of the couplings as follows

$$
\alpha(\hat{s}) \rightarrow \alpha_0/(1 + \hat{s}/\Lambda^2)^2, \tag{2.11}
$$

where $\hat{s}$ is a square of the partonic center-of-mass energy and α_0 is a coupling value in

the low-energy approximation. The value of Λ describes a characteristic energy at which unknown new physics processes contributions prevents the WZ production from violating unitarity. At Tevatron experiments, it is customary to choose $\Lambda = 2$ TeV, just beyond the energy reach of the accelerator.

The WWZ triple gauge couplings can be studied by direct and indirect measurement of the WWZ vertex. The first studies were done at the Large Electron-Positron Collider (LEP) at CERN measuring the coupling parameters from the $e^+e^- \rightarrow W^+W^-$ processes. The production of two W bosons can happen via an exchange of the Z and γ bosons. Thus, the measurements of WWZ coupling at the LEP experiments were model-dependent based on the relation between WWZ and $WW\gamma$ couplings. Directly, the WZ can be produced only at the hadron colliders as it is a charged final state, inaccessible in e^+e^- machines. Therefore, Tevatron data offer a unique opportunity to study the WWZ vertex in a model-independent way. An ever-increasing integrated luminosity of collected data at the Tevatron also allows to perform this measurement with a good accuracy.

2.3 New Heavy Resonances

As we know, the SM has a remarkable success to describe electroweak interactions at low energies. However, this does not exclude the possibility of having much reacher gauge boson spectrum at high energies. One of the extensions of the SM[4] predicts additional heavy W- and Z-like bosons as extension of the SU(2) symmetry, usually called sequential bosons and referred to as W' and Z' bosons. Those are narrow resonances and their coupling to the SM particles are similar to the couplings between the SM W and Z bosons. If such sequential W' exists, it would couple to the SM W and Z bosons (see in Fig. 2.2). This thesis describes the search for such hypothetical resonance.

The model with extended gauge boson sector is not the only model predicting the heavy resonances decaying to WZ boson pair. One of the alternative models that explain the mass generation is the Technicolor (TC)[5]. The electroweak symmetry is broken through

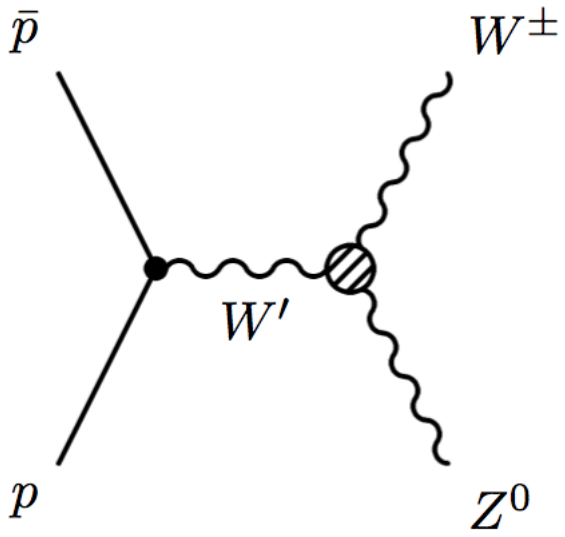

Figure 2.2: $W' \rightarrow WZ$ *Feynman diagram.*

the dynamics of new gauge interactions coupled to new massless fermions. The new strong interaction leads to new composite, short-lived particles, or techni-particles. Within the most modern version of this model, so-called low-scale Technicolor (LSTC)[6,7], the lightest particles can have mass below 500 GeV, and can be produced at the Tevatron.

The major decay channel for these new particles, such as techni-rho (ρ_T) and techni-a (a_T), is predicted to be dominated by a decay to two gauge bosons, such as WZ, to one gauge boson and a techni-pion (π_T), or to two technipions: $\rho_T^{\pm}/a_T^{\pm} \rightarrow W^{\pm}Z$, $\rho_T^{\pm}/a_T^{\pm} \rightarrow W^{\pm}\pi_T^0$, or $\rho_T^{\pm}/a_T^{\pm} \rightarrow \pi_T^{\pm}\pi_T^0$. However, within the LSTC, the mass of techni-pion is close to the mass of the techni-rho, which kinematically restricts techni-rho and techni-a decays to techni-pions. In this case, $\rho_T^{\pm}/a_T^{\pm}$ particles dominantly decay to a pair of the $W^{\pm}$ and Z^0 bosons with the decay branching fraction, defined on page 13, for $\rho_T^{\pm}/a_T^{\pm} \rightarrow W^{\pm}Z^0$ production being strongly dependent on the relative masses of the techni-pion and techni-ρ/techni-a [3].

[3]As the ρ_T and a_T have almost the same masses ρ_T will be used throughout this Dissertation to refer these two particles collectively.

2.4 Experimental Signature

There are several decay modes of the W and Z bosons. They can decay to either leptons or quarks. The W boson decays to either a pair of a lepton and a corresponding antineutrino or a pair of up-type quark and down-type antiquark. The Z^0 boson decays to a pair of a fermion and a same-flavor antifermion. Each decay mode of a given particle is parameterized by the branching fractions, $Br.$, that is the rate of how often the particle decays to a given mode. The branching fractions of the W and Z boson decays are given in Table 2.4.

	W^- Bosoon		
Decay	$l\bar{\nu}_l$	$q_u\bar{q}_d$	
$Br.$	10.80%	67.60%	
	Z^0 Bosoon		
Decay	ll	$q_u\bar{q}_u$	$\nu_l\bar{\nu}_l$
$Br.$	3.37%	69.91%	20.00%

Table 2.4: *The branching fractions for different decay modes of the W^- and Z bosons. The W^+ decays have the same branching fractions as the W^-.*

In this Dissertation only fully leptonic decays of the WZ boson pair are studied. The events with three charged leptons and neutrino are considered. As seen from the Table 2.4, such decay of boson pair has the smallest branching fraction ($Br(WZ \to 3\ell\nu) = 0.36\%$). However, it offers the background-free signal as the leptons have a much more distinct experimental signature in the detector than the jets produced by the hadronic W and Z boson decays (see Chapter 4).

The charged leptons from the WZ decays are electrons, muons, and tau leptons. A tau lepton is much heavier than either electron or muon and decays promptly in the detector. Some fraction of decays ($\sim 17.85\%$) is to electron or muon with two neutrinos, *e.g.* $\tau \to e\bar{\nu}_e\nu_\tau$. Thus, the experimental signatures of the WZ production decaying leptonically involve electrons, muons, and an imbalance in energy due to unobserved neutrinos.

2.5 Previous Studies

The WZ production cross section was previously measured by the CDF[8] and DØ[9] experiments at the Tevatron collider. The search for anomalous WWZ couplings was performed by the LEP experiments and the DØ experiment[9] at the Tevatron.

Both the CDF and D0 collaborations searched for heavy W-like bosons decaying to fermions[10–12]. The current limits on such W' bosons are near or below 1 TeV. The studies presented in this thesis are the first that search for the resonances primarily decaying to WZ gauge bosons and thus, it is complimentary to the previous searches. The searches for Technicolor was performed by the DØ collaboration in W+jets final state[13]. These searches are sensitive to a particular narrow Technicolor parameter phase space with the π_T mass is heavier than a half of the ρ_T mass, thus making the $\rho_T \to \pi_T\pi_T$ kinematically forbidden, and at the same it is lighter than the mass difference between ρ_T and W boson, thus making $\rho_T \to W\pi_T \to Wjj$ process the dominant ρ_T decay mode. The search for Technicolor particle production in WZ decay mode allows probing for Technicolor particle production with heavier π_T masses, where the dominant process is $\rho_T \to WZ$.

Chapter 3

Apparatus

Data used in this Dissertation is collected by the DØ detector at the Tevatron collider[14] from April 2002 through the end of 2008. The Tevatron is a proton-antiproton ($p\bar{p}$) collider at the Fermi National Accelerator Laboratory (Fermilab). It operates at a center-of-mass energy of $\sqrt{s} = 1.96$ TeV. The DØ detector is one of the two multi-purpose detectors at the Tevatron. Another detector is the Collider Detector at Fermilab (CDF).

3.1 The Accelerator Chain

Beam acceleration chain at the Fermilab consists of several complex steps (see Fig. 3.1). These steps include production of proton and antiproton beams, steering and cooling, accelerating and injecting of the beams into the Tevatron, and final acceleration of beams to 0.98 TeV each. The orbits of the accelerated beams are further steered to collide in the centers of the CDF and DØ detectors. As production of the antiprotons is extremely difficult task, the final step is to collect antiprotons in the recycler for later use. I briefly describe each of the steps of the accelerator chain below.

3.1.1 Creating the Proton Beam

The hydrogen atoms are used as a source of protons. The atom is ionized using a magnetron chamber[15]. The chamber consists of a cathode, located at the center, while the walls of the chamber serve as an anode. Due to a strong electric field in the chamber, the electron of

the hydrogen atom is stripped away leaving the ionized nucleus of a hydrogen atom (H^+). Further interaction with a cathode results in production of negative hydrogen ions H^- which are steered towards a Cockcroft-Walton generator, see Fig. 3.2, that accelerates H^- to the energy of 750 keV.

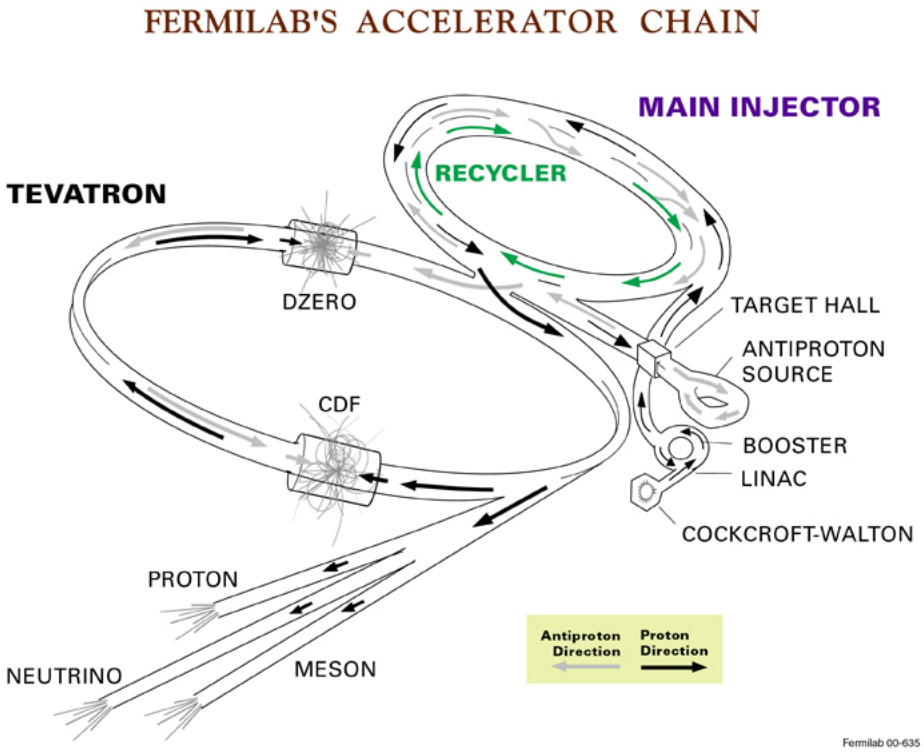

Figure 3.1: *Accelerator chain at Fermilab.*

The Cockcroft-Walton generator is followed by a linear accelerator (linac)[16]. Inside the linac, 750 keV energy ions are further accelerated to an energy of 400 MeV with radio frequency electric fields. At the end of the linac, the negative hydrogen ions pass through a carbon foil, that strips two electrons away, leaving only protons to pass through the foil.

The proton beam then enters a Booster[17], that is a circular accelerator, a synchrotron, with a 475 m of circumference. It uses magnets to keep protons on a circular orbit and by using radio frequency electric field synchronized with the position of the beam, the protons are accelerated to an energy of 8 GeV.

Figure 3.2: *Cockcroft-Walton generator at Fermilab.*

3.1.2 The Main Injector

The Main Injector[18] is a synchrotron with a circumference of 3.3 km. It receives beam of protons with an energy of 8 GeV, accelerates them to 150 GeV and injects it in the Tevatron. At the intermediate stage, when the the energy is ramped up to 120 GeV, some part of protons is directed to the Antiproton Source. Those participate in a production of $\bar{p}$s, as described below. Later the beam of antiprotons are injected back in the Main Injector for acceleration to 150 GeV prior to the injection in the Tevatron.

3.1.3 Creating the Antiproton Beam

The beam of 120 GeV protons, p, is directed to a nickel target. The collisions create a shower of particles, including antiprotons, $\bar{p}$, via $p + p \rightarrow p + p + \bar{p} + \bar{p}$ reaction.

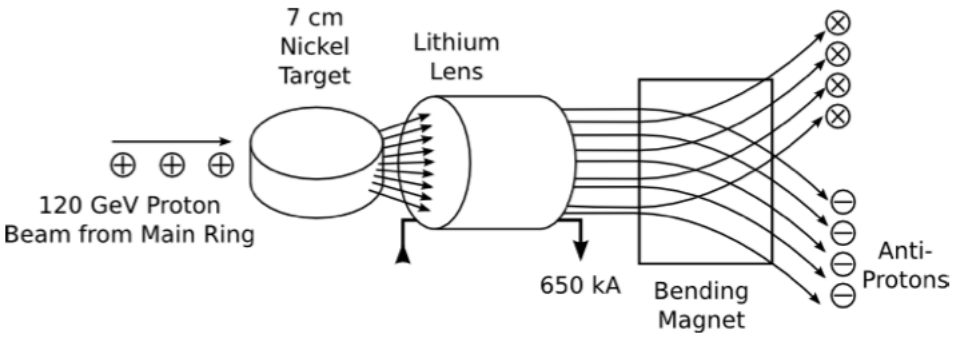

Figure 3.3: *120 GeV protons hit a nickel target producing wide range of particles. Those are focused by a lithium lens. The antiprotons are extracted by the magnetic field.*

A long lithium lens is used, see Fig. 3.3, to focus the resultant broadly-distributed beam. The beam then goes through the magnetic field which separates the positively and negatively charged particles. The extracted antiprotons are then sent to the Debuncher, another synchrotron, which accelerates the slowest particles and decelerates the fastest ones. At the next step the Accumulator separates the antiprotons into 8 GeV energy bunches. As the $\bar{p}$-s are produced at different angles and positions, stochastic cooling is used to correct the orbits of such particles. Once a sufficient quantity of antiprotons is collected and cooled down, they are sent to Main Injector to be accelerated up to 150 GeV before injection in the Tevatron.

The production of antiprotons is a costly procedure. About $\sim 10^5$ proton is needed to produce one antiproton. Due to this, the Antiproton Recycler[19] is used to store antiprotons at the end of a Tevatron store. Recycler is located along the Main Injector and stores the $\bar{p}$-s at a fixed energy of 8 GeV.

3.1.4 The Tevatron

The proton and antiproton beams at energy of 150 GeV are loaded in the Tevatron as 36 bunches and then accelerated up to 980 GeV. The protons circulate clockwise, while antiprotons - counterclockwise, inside the same beam pipe. The dipole magnets bend the beams allowing to travel along circular orbit. The quadrupole magnets are used to focus and compress beams to about 30 microns in radius. All magnets are cooled down to the temperature of liquid helium in order to sustain huge electrical current flowing through their coils. The Tevatron has a circumference of 6.28 km. At the two locations around the Tevatron ring, where CDF and DØ detectors are located, the p and $\bar{p}$ beams are brought into collisions every 396 ns.

The instantaneous luminosity is a measure of the collision rate per unit area per unit time. It is measured in units of $\mathrm{cm}^{-2}\mathrm{s}^{-1}$ and can be calculated as follows

$$\mathcal{L} = f\frac{n_1 n_2}{4\pi\sigma_x\sigma_y}. \tag{3.1}$$

Here, f is the collision rate, n_1 and n_2 are number of particles in two colliding bunches, and $\sigma_x\sigma_y$ is overlapping transverse area of the beams.

The instantaneous luminosity summed up over the time gives an integrated luminosity. As a result, it is measured in unites of cm^{-2}. This unit, more commonly, is called as inverse barn, b^{-1}, with the relation $1\ \mathrm{b}^{-1} = 10^{-24}\ \mathrm{cm}^{-2}$. Accordingly, data collected by the detector is measured in the same units. The results presented in this thesis are obtained using data 4.1 fb^{-1} of integrated luminosity.

3.2 The DØ Detector

The DØ detector[20–22] is a general purpose hermetic detector to study the high momentum particles created from proton-antiproton collisions at a center-of-mass energy of 1.96 TeV. The detector consists of different sub-detectors that play an important role in measurement of momentum and energy as well as identification of the particles produced by the $p\bar{p}$

collisions. Those sub-systems are:

- The central tracking system which consists of a silicon microstrip tracker (SMT) and central fiber tracker (CFT). These are surrounded by a 2 T superconducting solenoidal magnet. The tracking system is important to determine the location of interaction vertex, measure a momentum and a track of a charged particle.

- The pre-shower detectors which are used to improve the identification of electrons and photons.

- The calorimeter system that consist of electromagnetic (EM) and hadronic (HAD) layers and an inter-cryostat detector (ICD). The calorimeter system provides the energy measurement for EM particles, that are electrons and photons, as well as for showers of hadronic particles, such as pions, kaons, *etc.*.

- The muon spectrometer consists of scintillating material and drift tubes and is surrounded by the toroidal magnet. It plays an important role to identify muons, measure their momentum and position, and also provides information for triggering of the events.

The side view of the DØ detector is shown in Fig. 3.4.

3.2.1 The DØ coordinate system

In the detector description and data analysis the DØ experiment uses a right-handed coordinate system, where the z-axis is along the proton direction and the y-axis is directed upward, see Fig. 3.4. The angle ϕ is an azimuthal angle with respect to the x axis in the $x-y$ plane. This plane is also called the $r-\phi$ plane, where r defines the perpendicular distance between the position and the z axis. ϕ angle varies between 0 and 2π. The angle θ is a polar angle with respect to the z axis in the $y-z$ plane and varies from -π to π. The rapidity (y) and pseudorapidity (η) are defined as follows:

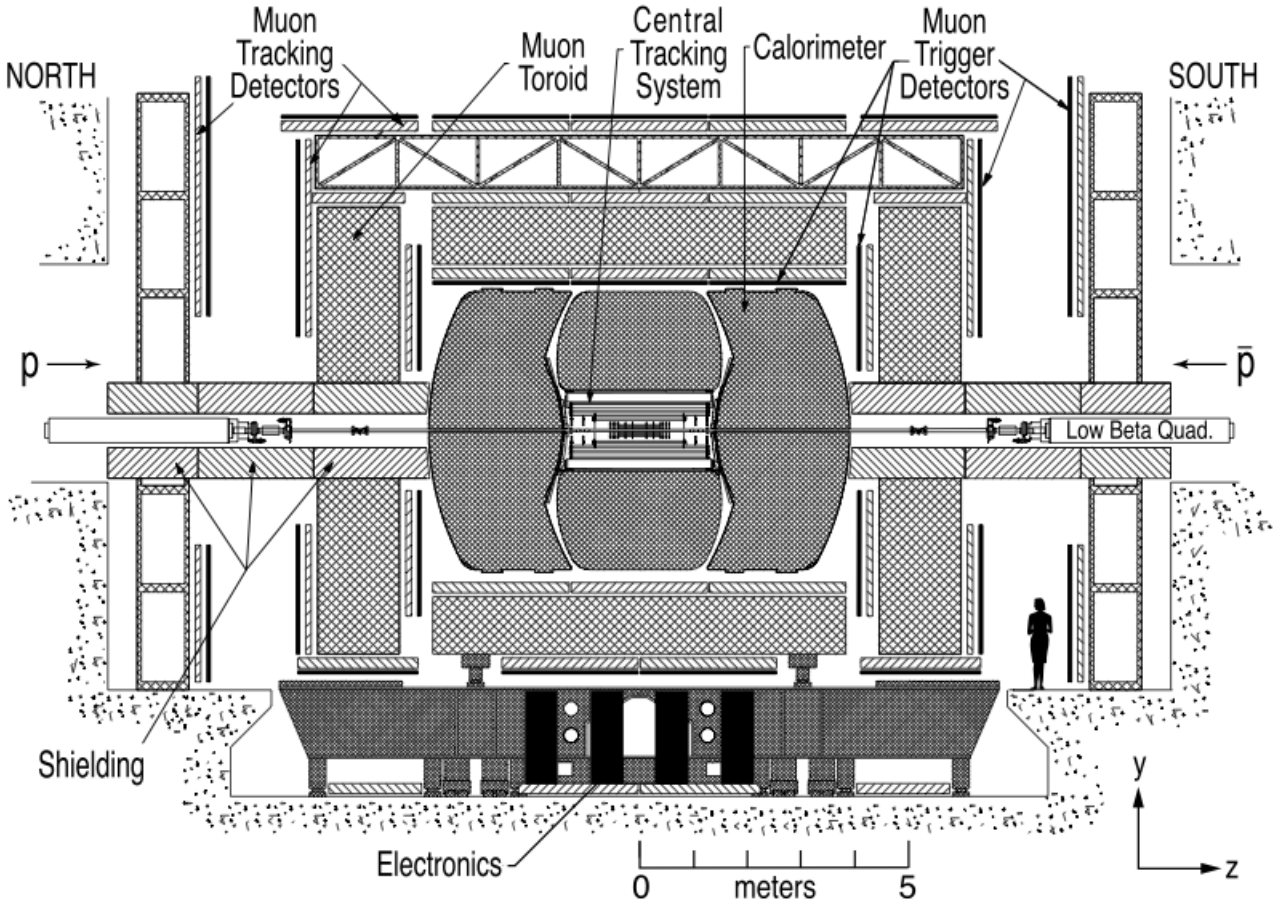

Figure 3.4: *The view of sub-systems of the DØ detector.*

$$y = \frac{1}{2} ln \frac{E + p_L}{E - p_L} \tag{3.2}$$

$$\eta = \frac{1}{2} ln \frac{|\vec{p}| + p_L}{|\vec{p}| - p_L}, \tag{3.3}$$

where E and $\vec{p}$ are energy and momentum of the particle, while p_L is a longitudinal component of the momentum. In the relativistic limit, when $(mc^2/E) \to 0$, the pseudorapidity approximates the rapidity. The pseudorapidity more commonly is defined in terms of polar angle as follows

$$\eta = -ln(tan\frac{\theta}{2}). \tag{3.4}$$

The distance in the $\eta - \phi$ plane, ΔR, is defined as given below:

$$\Delta R = \sqrt{\Delta\eta^2 + \Delta\phi^2}, \tag{3.5}$$

where $\Delta\eta$ and $\Delta\phi$ are differences between the two points in η and ϕ, respectively.

In addition there are number of variables used in analysis that are defined using energy, momentum and angles. The transverse energy and momentum are defined as follows:

$$E_T = Esin(\theta) = E/cosh(\eta) \tag{3.6}$$

$$p_T = |\vec{p}|sin(\theta). \tag{3.7}$$

The projection of the momentum on the coordinate axes are commonly calculated as

$$p_x = p_T cos(\phi),\ p_y = p_T sin(\phi),\ \text{and}\ p_z = p_T/tan(\theta). \tag{3.8}$$

3.2.2 Central Tracker

The inner most part of the central tracker is the Silicon Microstrip Tracker. It surrounds a beam pipe. The beam pipe of the DØ detector is made of beryllium with a wall sickness of 0.508 mm and dimensions of 38.1 mm and 2.37 m for an outer diameter and a length, respectively. The CFT is following part of the tracking system after the SMT. They both are surrounded by the solenoidal magnet, see Fig 3.5. The magnetic field acts on a charged particle passing through the tracking system and bends its trajectory. The path of the particle, with charge q, can be detected inside the tracking system and its radius, r, together with the magnetic filed of the magnet, B, allows us to measure a momentum of the particle, $p_T = kqrB$, where k is a constant 0.3 GeV/(cTm). The relative transverse momentum resolution is measured to be $\delta p_T/p_T = 0.002p_T\%$.

The Silicon Microstrip Tracker

The SMT is crucial for the determination of vertices over a wide pseudorapidity region of the calorimeters and muons systems. The schematic view of the Silicon Microstrip Tracker is shown on Fig. 3.6.

The SMT consists of thin layers of silicon arranged in readout layers and oriented either parallel or perpendicular to the beam pipe. Such orientation will result in charged tracks to be as perpendicular to the SMT sensors as possible. The detector has six barrels in the central region, individual of them having four silicon readout layers. The centers of barrels are located at $|z| \approx 6.2, 19.0, 31.8$ cm. Each barrel is capped at outer side from the center of the detector with "F-disk". These disks are twelve double-sided wedge detectors located at $|z| \approx 12.5, 25.3, 38.2, 43.1, 48.1$ cm. In the far forward region, $|z| \approx 100.4, 121.0$ cm, two large-diameter disks, "H-disks" provide tracking, allowing to measure tracks with small angles to the beam pipe.

The silicon tracker is functioning based on a charged particle ionization. When the charged particle passes though a silicon ionized pair travels towards electrodes under the influence of the electron field. The charge is collected by the capacitor arrays and then read out. It provides the measure of the energy of incident particle. Overall, the SMT provide tracking and vertexing in $|\eta| <3$ region with resolution of track position measurement of the order of 10 μm.

The Central Fiber Tracker

The CFT is made of scintillating fibers, with diameter of 835 μm, mounted on eight cylinders that enclose the SMT. To accommodate the forward SMT "H-disks", the two innermost cylinders are 1.66 m long; the outer six cylinders are 2.52 m long. The fibers are arranged as two layers on the cylinder walls: the fibers in one layer are aligned with the beam axis. Those are called axial layers. While ones in another layer, called a stereo layer, are at a stereo angle in ϕ of +3° or -3°. This allows to identify the trajectory of a charged track in three dimensions.

The principle of functioning of fiber detector is based on the ionization when a charged particle traverse through the material. Some fraction of particle's energy may excite the molecules in the material that will emit visible light during the subsequent de-excitation.

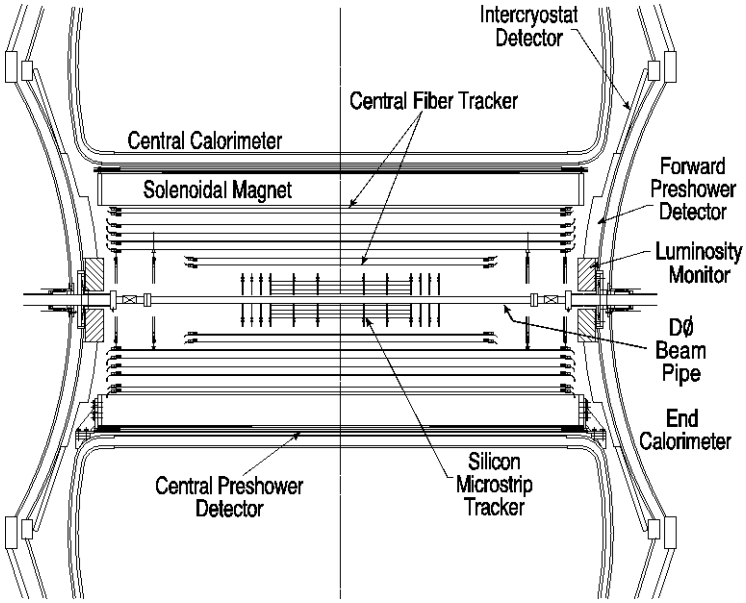

Figure 3.5: *Side view of the central tracking system of the DØ detector.*

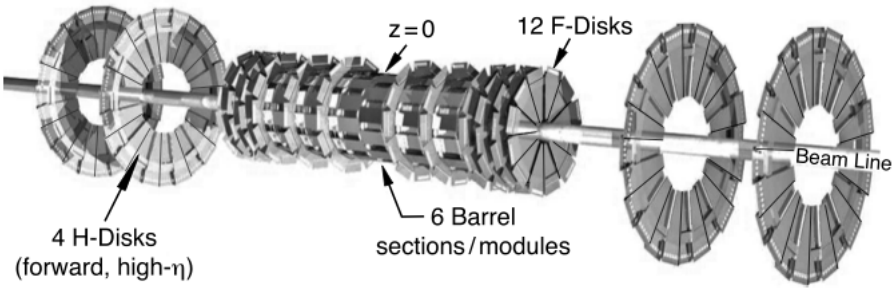

Figure 3.6: *The design of silicon microstrip tracker.*

One of the ends of scintillation fibers are coated with aluminum so that most of the light is collected by the waveguides (see Fig. 3.7). The photons will travel through the fiber and are collected in visible light photon counters (VLPCs) outside of the detector. From here, the signal is fed to analog front-end boards (AFE), which provide pre-amplifying services, temperature control of the VLPCs, and a so-called Level 1 trigger information. The latter is further discussed in Section 3.2.8 below. The CFT provides coverage for $|\eta| \leq 1.7$ and a resolution of about 100 μm given that the location of the individual fiber is known to better

than 50 μm.

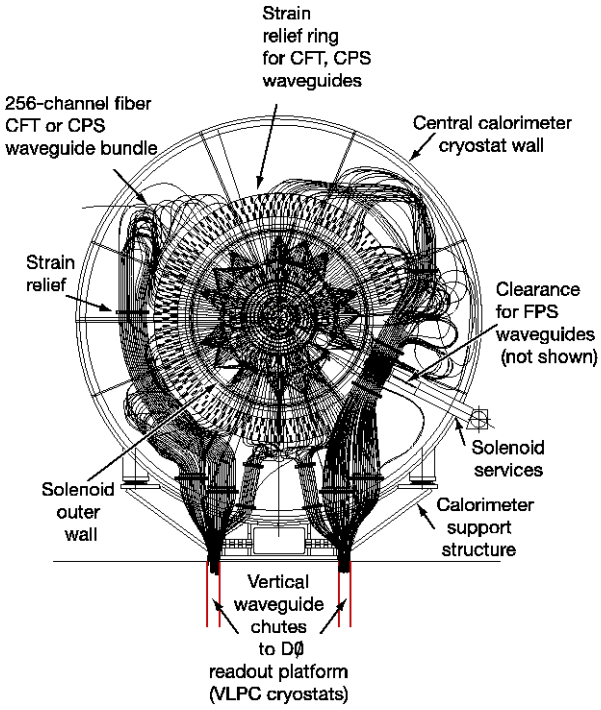

Figure 3.7: *The waveguides of the Central Fiber Tracker.*

3.2.3 Solenoidal Magnet

The goal of superconducting solenoidal magnet is to optimize the momentum resolution, $\delta p_T/p_T$, and tracking pattern recognition. It is 2.73 m in length and 1.42 m in diameter and has $\sim$ one radiation length [1] ($0.87X_0$) at $\eta = 0$. The magnet is cooled down at the temperature of liquid helium in order to operated with large current of 4,749 A. The magnet provides uniformly distributed 2 T magnetic field (see Fig. 3.8).

[1]The effective energy loss of an electron passing the material is described by the equation $E = E_0 e^{-x/X_0}$, where E_0 is the original energy, X_0 is the radiation length of the material, and x is the distance traveled by the electron. Hence, the radiation length of a material is a distance at which an electron looses all but $1/e$ fraction of its original energy.

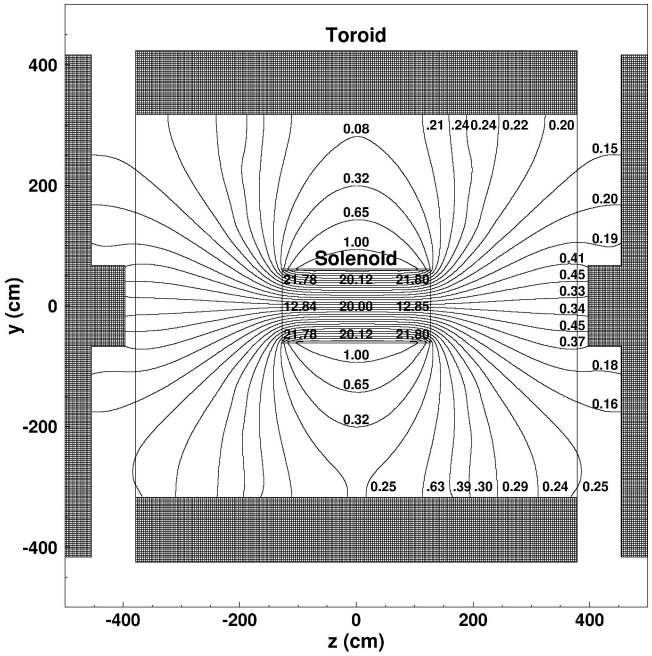

Figure 3.8: *2 T solenoidal magnet at DØ detector.*

3.2.4 Preshower detectors

Between the solenoidal magnet and the calorimeters there are preshower detectors. These are central preshower detector (CPS), covering the region $|\eta| < 1.3$, and forward preshower detector (FPS), covering the region $1.5 < |\eta| < 2.5$ (see Fig. 3.5). They function as both calorimeters and tracking detectors and provide valuable information in the electron and photon identification as well as background rejection. The information from the preshower detectors is successfully used in offline reconstruction to correct the electromagnetic energy measurements in the calorimeters for losses in the solenoid and the rest of the material, placed before the calorimeters, such as cables and supports. In addition to this, fast energy and position measurements within the CPS and FPS play an important role in the Level 1 trigger (see Section 3.2.8).

Both CPS and FPS are made of triangular strips of scintillation material, as shown in Fig. 3.9. Such design prevents a dead space between strips and results in the most of the

tracks traversing more than one strip. This improves of track position measurement. Each scintillating strip is wrapped in mylar for optical isolation and the ends are painted white that enhances reflectivity. Every single strip has wavelength-shifting fiber (WLS fiber) in the center that collects the scintillation light and re-emit it in the visible spectrum to increase the efficiency of the VLPs (Section 3.2.2).

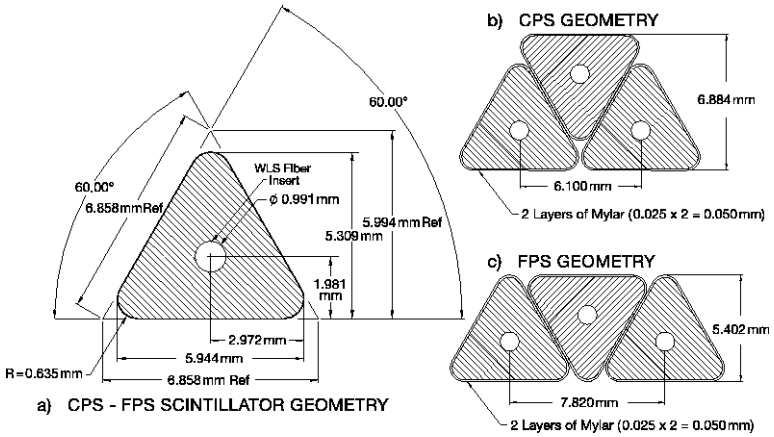

Figure 3.9: *The geometry of central and forward preshower detectors.*

The CPS is located in the 5 cm gap between the solenoid and the central calorimeter and consists of three concentric cylindrical layers of triangular scintillating strips. In front of the CPS there is a lead radiator with an additional $\sim 1X_0$. Thus, there is about two radiation lengths of material for particles at normal incidence, that increases up to about four radiation lengths at the largest angles. Each scintillating layer contains 1280 strips. Out of three scintillating layers the inner most layer is axially oriented, while the second and the third layers are oriented with a $u = 23.774°$ and $v = 24.016°$ stereo angles, respectively. The ends to the u and v layers are aligned along the end of the axial layer (see Fig 3.10).

The two FPS detectors (north and south) are made of two layers separated by a $2X_0$-thick lead-stainless-steel absorber (see Fig. 3.10). Each layer consists of two planes of scintillating strips. The layers closest to the interaction region are called as the minimum ionizing particle (MIP) layers, while the further ones are knows as the shower layers. The charged particle, passing though MIP layers, produces minimum ionizing signal, that is used to

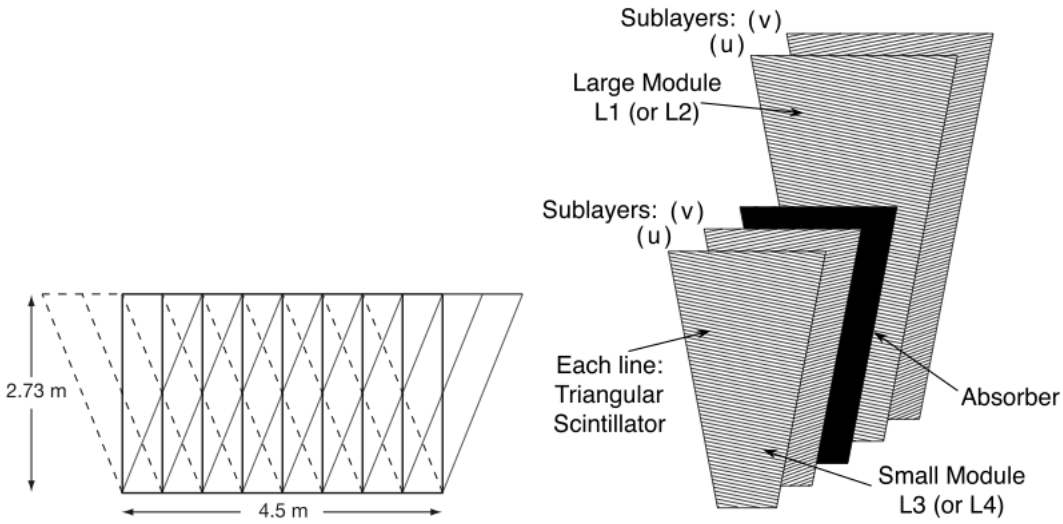

Figure 3.10: *The CPS (left) is made of three concentric cylindrical layers, one axial and two at stereo angles. The FPS (right) is made of two layers of scintillating strips and an absorber.*

measure the location of a track (in η, ϕ, and z). Electrons will dominantly shower in the absorber, producing rather wide cluster of energy in the shower layers that is spatially match to the signal from MIP layers. In contrary, photon will not interact much with the MIP layers but will produce shower signal in the shower layers. Heavy charged particles, such as hadrons, are less likely to shower, leaving additional MIP signal in the shower layers. These parameters are effectively used in identification of particles passing through the DØ detector.

3.2.5 The DØ Calorimeters

The calorimeters are designed to provide an energy measurement for electrons and photons as well as for jets, that are produced by showering of hadrons. The calorimeters also play an important role in identification of electrons, photons, jets, and muons and in the measurement of the energy balance in events.

The DØ calorimeter system (see Fig. 3.11) is made of depleted uranium and liquid argon. It is divided in two parts: a central calorimeter (CC) covering the region $|\eta| < 1.1$, two identical endcap calorimeters (North and South EC) with the coverage $1.4 < |\eta| < 4.2$,

and the intercryostat detector (ICD) covering the region between CC and EC. The CC and EC parts are located within its own cryostat that keeps the detector temperature at $\sim$ 90 K. Both CC and EC calorimeters have layers of three types: electromagnetic, finely segmented hadronic (FH), and coarsely segmented hadronic (CH). Side view of the CC and EC is shown on Fig. 3.11.

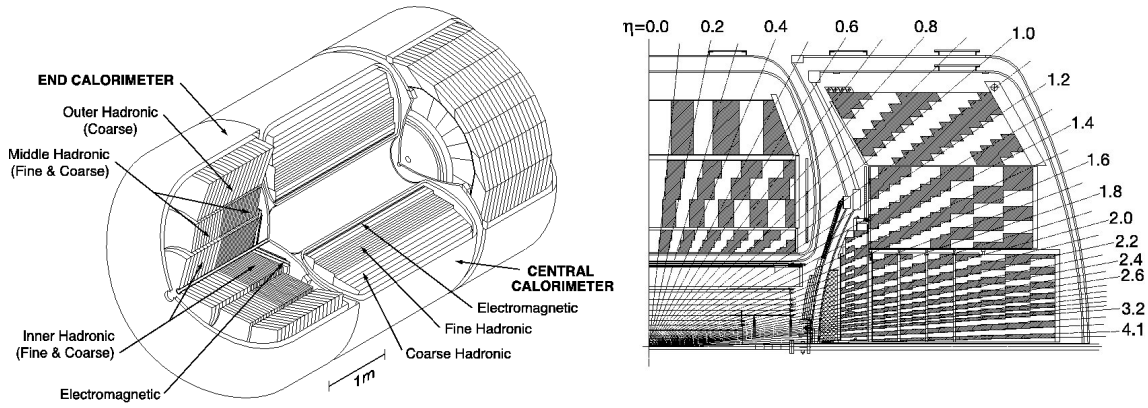

Figure 3.11: *The 3-D view of the DØ calorimeters with the layout of its EM, FH, and CH layers (left). The towers of calorimeter cells are shown on the side view of the central and endcap calorimeters (right).*

The DØ calorimeter is made so that the energy deposits are sampled at various depths of the shower. This is achieved by a presence of alternating layers of absorber and active medium. A typical calorimeter cell is shown on Fig. 3.12. Each cell has 2.3 mm liquid argon filled gaps with a grounded absorber on one side and a positively charged (2 to 2.5 kV) signal board on the other side. When particle passes though a cell, shower occurs within the absorber, the shower particles ionize the atoms within the liquid argon gap, producing a charge that is collected by the signal boards.

The electromagnetic showers, produced by particles with energies, common for those produced at Tevatron, are caused mostly by two processes: bremsstrahlung ($e \rightarrow e\gamma$) and photon conversion ($\gamma \rightarrow e^-e^+$). The EM layers of the calorimeter are characterized by the thickness in units of radiation length, X_0 (see Section 3.2.3). The hadronic shower happens due to strong interaction of hadrons, both charged and neutral, with the nuclei

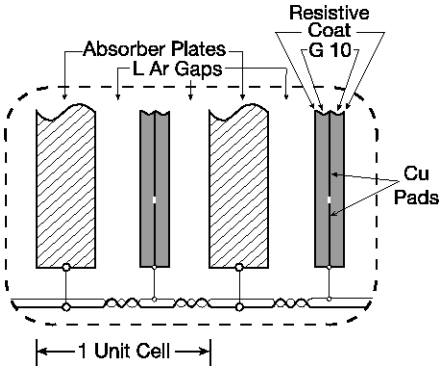

Figure 3.12: *The DØ calorimeter cell.*

of the calorimeter material. As a result, most commonly, charged and neutral pions are produced which the subsequent decay of neutral pions into photons ($\pi^0 \rightarrow \gamma\gamma$). Thus, a hadronic shower is a combination of both electromagnetic and pure hadronic interactions and those tend to be wider and longer than the EM showers. Due to this, width of hadronic layers of the calorimeter is described in units of absorption length (λ_A). λ_A is a mean free path of a particle before it has an inelastic collision with a nucleus.

The EM layer of CC and EC calorimeters consists of four sub-layers of 1.4, 2.0, 6.8, and 9.8 X_0 of thickness. In EC those sub-layers are 1.6, 2.6, 7.9, and 9.3 X_0-thick. Totally, EM calorimeters are 20 X_0 and 21.4 X_0-thick for CC and EC, respectively. The granularity is $\Delta\eta \times \Delta\phi = 0.1 \times 0.1$ for all layers but the third layer which has a finer granularity of 0.05×0.05. It is needed for more precise measurement of the energy deposition as the energy shower peaks in this layer.

In CC fine and coarse hadronic layers are made of three and one sub-layers, with 1.3, 1.0, 0.76, and 3.2 λ_A, respectively. In EC the design of hadronic part of the calorimeter system is a bit more complex. There are inner hadronic modules (fine and coarse layers with four and one readout cells, respectively) the closest to the beam line. That is followed by the middle hadronic modules, fine and coarse layers with four and single sections, respectively. The outer-most parts of the calorimeter are called the outer hadronic modules of ECs. The FH is made of niobium-uranium alloy while the CH is made of copper and stainless steel in

CC and EC, respectively.

Totally, the calorimeter has approximately 50,000 cells and a non-zero probability of false signal due to electronics noise or uranium decay in the calorimeter. To avoid the contribution from these effects in energy reconstruction a zero-suppression algorithm[23] is used. It removes the cells in which energy measurement is not significantly higher than the noise level. The drift time in the calorimeter cell is $\sim$ 420 ns that is longer than the bunch separation (396 ns) and can cause a "pile-up" of energy from previous event. This is resolved by a readout electronics using Base Line Subtraction algorithm(BLS).

The Intercryostat Detector

The ICD is located between the central and endcap calorimeters covering the region $1.1 < |\eta| < 1.5$ and helps to correct for the energy deposited in this poorly instrumented region. It consists of additional sampling layers divided into eight $\Delta\eta \times \Delta\phi = 0.3 \times 0.4$ octants (tiles). Each of the octants is made of 0.1×0.1 sub-tiles. The light produced within sub-tiles is collected by the fibers and is read out by photo-multiplier tubes (PMT).

3.2.6 The Muon System

Muons interact much less with the calorimeters depositing only MIP signal of the order of a few GeV. These particles are detected in the muon system that is the outer most part of the DØ detector. For measurements and triggering in central region ($|\eta| \leq 1.0$) the Proportional Drift Tubes (PDTs), and the Central Scintillation Counters are used. The forward muon system extends up to $|\eta| \approx 2.0$ and uses Mini Drift Tubes (MDTs), trigger scintillation counters and beam pipe shielding (see Fig. 3.13). The toroidal magnets are used to bend the trajectory of the muon and measure its momentum and a charge. This is done independently from the tracker. The magnetic fields of 1.8 and 1.9 T are produced by the central and forward toroids, respectively.

The PDTs (MDTs) are filled with a gas mixture of 84% argon, 8% CF_4, and 8% CH_4

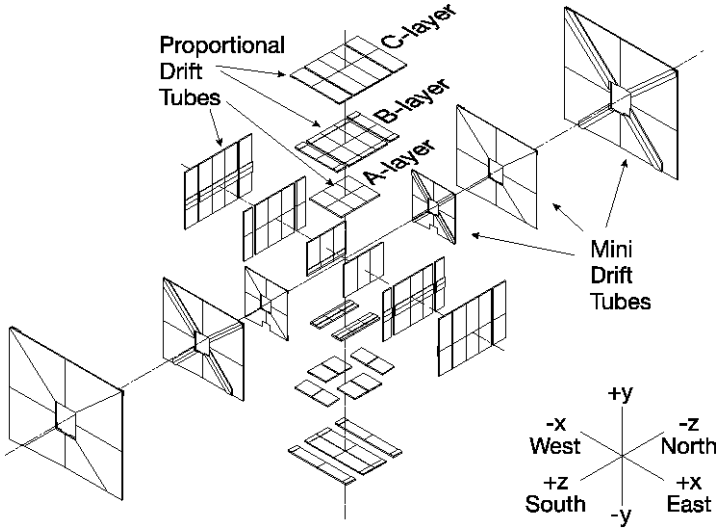

Figure 3.13: *The schematic view of central and forward components of the muon systems at DØ.*

(90% CF_4 and 10% CH_4). As a charged particle travels through the drift tube it ionizes the gas. The produced charge is collected by high-voltage wires and the position is extrapolated to multiple wires. In addition to this, in the forward region iron-polythylene-lead cover is used to reduce the background to muons from the beam halos. There are three drift tube layers in both the central and forward regions. The inner most A layer is located inside the toroidal magnet, while B and C layers are outside. The A layer is attached by two layers of pixel scintillators ($A-\phi$ counters). There is a support structure at the bottom of the central muon system leaving a hole in the coverage between $225^\circ < \phi < 310^\circ$. In forward region A, B, and C layers are located between scintillation counters (FSC). A good resolution of the scintillation counters in both central and forward regions allows associating a track to a particular bunch crossing and helps to reject cosmic muons. The information from muon system is used for identification of the muons, position/momentum measurement, and triggering.

3.2.7 The Luminosity Monitors

An important device for the data-taking at the DØ experiment is a pair of the luminosity monitors (LMs). As seen in Eq. 3.1, the luminosity is proportional to the number of inelastic $p\bar{p}$ collisions. The LMs measure the rate of these collisions. They are located near the beam pipe, at $z = \pm 140$ cm, covering the region $2.7 < |\eta| < 4.4$ (see Fig. 3.14). The LMs detect the forward particles produced in $p\bar{p}$ collisions that have low transverse momentum. A good time resolution (≤ 2.7 ns) of the LMs allows distinguish particles resultant of $p\bar{p}$ collisions from those originated from the beam halo, or the muons that are produced from interaction of protons and antiprotons with the beam material and traveling along the beam orbits. In the first case the particles detected on two monitors coincide in time, while in the latter case those are separated in time. The position of the interaction vertex can be calculated as follows

$$z_v = \frac{c}{2}(t_- - t_+), \tag{3.9}$$

where t_- and t_+ are the particles incident time on two monitors. The background from the beam halo events can be reduced significantly with the requirement $z_v < 100$ cm.

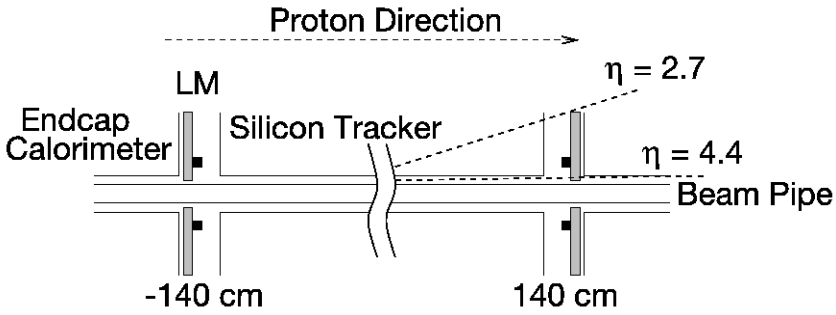

Figure 3.14: *The DØ luminosity monitors.*

The luminosity is calculated by the following formula

$$\mathcal{L} = f\frac{\bar{N}_{LM}}{\sigma_{LM}}, \tag{3.10}$$

where f is beam crossing frequency, $\bar{N}_{LM}$ is an averaged number of inelastic collisions per beam crossing, and σ_{LM} is the effective inelastic cross section of the monitors that takes into account acceptance and efficiency of the LM detectors. Knowing the fraction of beam crossings with no collisions the $\bar{N}_{LM}$ can be determined, following a Poisson statistics, that accounts for multiple $p\bar{p}$ collisions in a single beam crossing.

3.2.8 The Trigger at DØ

As mentioned above, there are 36 bunches of protons and antiprotons traveling around the Tevatron every 21 μs. This results in a collision rate of about 1.7 MHz. However, the resources to record the data on a tape allow us to handle the events with $\approx$ 100 Hz rate. The three level trigger system is used at the DØ experiment to reduce initial collision rate up to the final one. At the Level 1 (L1) a trigger accept rate is about 2 kHz. This step relies on hardware trigger elements. In the Level 2 (L2) trigger the information from different sub-detectors are collected in a global processor and a trigger decision is made based on individual objects and correlations between them. The resultant accept rate is $\approx$ 1 kHz. Accepted events are processed by a farm of Level 3 (L3) computers, using different algorithms and fast reconstruction of the processes from $p\bar{p}$ collisions, or so-called events. At L3 events are accepted with a rate of 100-150 Hz and recorded for the offline reconstruction (discussed in Chapter 4). The overview of the triggering at DØ is shown on Fig. 3.15. In the regime of high instantaneous luminosity more events can occur passing all three trigger levels so that the rate after the L3 might still exceed the target rate. To accommodate this, some of the triggers are assigned a prescale, predefined for a luminosity range. It selects the events based on the random number generator, "pass 1 of n". The triggers are combined into a trigger list. Periodically the trigger lists are updated to account for the upgrades of the detector as well as the changes in the reconstruction software and the profile of the instantaneous luminosity.

Level 1 Trigger

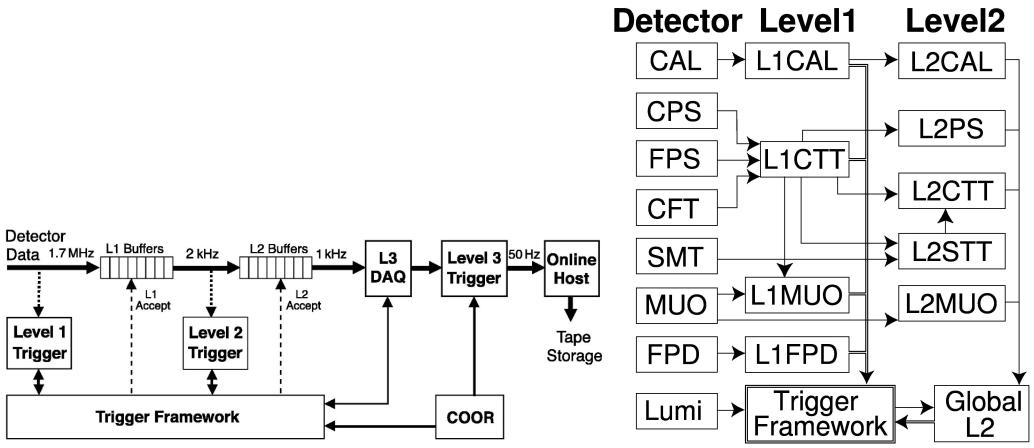

Figure 3.15: *Overview of the DØ trigger system (left). The diagram of the DØ L1 and L2 trigger systems (right). The arrows show the flow of data.*

The information from the central tracker, preshowers, calorimeters, and muon systems are used to make L1 decision (see Fig. 3.15). The L1 calculates trigger terms in 132 ns and stores them temporarily for 4.2 μs. It helps to avoid dead-time operation. The L1 decision is delivered at Trigger Framework (TFW) in ≤ 3.5 μs time. The TFW gathers information from each of L1 trigger devices and decides whether to accept a given event. In addition, TFW manages various vetoes and different trigger prescales.

- **Level 1 Calorimeter (L1CAL)** uses energy deposits in EM and EM + HAD layers of the calorimeters. The trigger decision is based on 1280 EM and 1280 HAD towers, with granularity of $\Delta\eta \times \Delta\phi = 0.2 \times 0.2$. The tower energy is corrected for energy scale, pedestal subtraction, and converted to E_T before input. In addition, different variables may also be used by the L1 calorimeter trigger, such as the sum of transverse energy in 4×8 cluster of towers, the total transverse energy, E_T, in the event, as well as an imbalance of the transverse energy in the event, $\not\!\!E_T$.

- **Level 1 Central Track Trigger (L1CTT)** makes a decision based on tracks reconstructed by the CFT, axial layers of CPS, and FPS. The hit patterns in the CFT are matched to 20,000 predefined tracks to identify the real trajectory which is then

spatially matched to the energy deposition in the preshower detectors. The trigger requirement applied on the number of tracks with p_T above the threshold.

- **Level 1 Calorimeter Tracks (L1CALTRACK)** is the combination of the L1CAL and L1CTT which helps to reject good fraction of background events. The L1CTT tracks are matched to the L1CAL objects, that can be electrons or jets, and additionally requires an isolation.

- **Level 1 Muon (L1MUO)** uses the information from the wire chambers, muon scintillation counters and L1CTT tracks to find a muon candidate. Additional quality requirements on matching is applied.

The Level 2 Trigger

The processing at L2 is more complex using a global processor (L2Global). It does detector-specific processing of an event, received from L1 trigger system, and tests the correlation between the physics objects in the event. The L2Global processor selects events based on both the selections applied at L1 and additional criteria. The events passing L2 are tagged for full readout and the next step of analysis at L3.

- **Level 2 Calorimeter (L2CAL)** preprocessor uses the EM and EM + HAD E_T from 2560 trigger towers of the EM and HAD layers of calorimeters, identifies electromagnetic and hadronic objects and calculates $\not\!\!E_T$of the event. Jets are reconstructed from the cluster (5×5) of calorimeter towers centered on seed towers with $E_T > 2$ GeV. The algorithm for electrons/photons uses similar clusters of towers though only from EM layers of the calorimeter and with $E_T > 1$ GeV requirement on seed towers. The 3×3 arrays of towers are used for isolation requirements. The list of electrons/photons/jets and $\not\!\!E_T$is fed to L2Global for further decision.

- **Level 2 Muon (L2MUO)** uses information from L1MUO and data from $\sim$ 150 front-end modules of PDTs, MDTs, and the scintillation counters and passes them

to corresponding preprocessors for central (L2MUC) and forward (L2MUF) regions. The L2MUO applies calibration and more precise timing information to improve the quality of the muon candidates. The charge, p_T, and angles (η, ϕ) of selected muon candidate are sent to L2Global.

- **Level 2 Preshower (L2PS)** allows to identify early showers from photons and electrons and provides a good spatial point that can be matched with the clusters in the calorimeter and tracks. These aid in detection of electrons and photons and background rejection at the trigger level.

- **Level 2 Central Track Trigger (L2CTT)** takes input from the L1CTT and the L2STT (discussed below) to analyze tracks either straight from L1CTT or together with tracks from L2STT. In the former case, L2CTT uses additional hit information to improve the measurement of the track p_T from L1CTT. In the second case L2STT provides improved p_T measurement. In both cases, additional isolation requirements are applied on selected tracks and p_T-sorted list of L2 tracks are sent to L2Global.

- **Level 2 Silicon Track Trigger (STT)** uses additional hit information and improves the measurement of the L1 tracks and reject false tracks. Improved spatial resolution allows trigger level tagging of long-lived particles.

The Level 3 Trigger and Data Acquisition

The L3 trigger provides an additional rejection of the events received from the L2. This is a software trigger using L3 trigger farm with 400 computer nodes. The data from the readout crates are transferred to the L3 farm using data acquisition system (L3DAQ) via Ethernet. The L3 trigger runs object-specific software algorithms (filter tools) of full data-readout. These algorithms perform several tasks: unpacking the raw data, finding hits, forming clusters, applying the calibration, and reconstructing the physics objects such as

electrons, photons, muons, taus, jets, interaction vertices, and $\not\!\!E_T$. The L3 decisions are based on complete physics objects as well as on the relationships between such objects.

Chapter 4

Event Reconstruction

Data, collected from the sub-detectors and stored on tape, are not directly applicable for physics analysis. It is first processed with the special reconstruction software, called DØ Offline Reconstruction Software (DØRECO). This software analyzes every single collision event and identifys, based on the information contained in the event, physics objects, which are interaction tracks of charged particles, vertices of these tracks, electrons, photons, muons, jets, and missing transverse energy. This chapter describes different algorithms used in the reconstruction procedure.

4.1 Track Reconstruction

A track does not represent any physics object, though it is used to measure a momentum of a charged particle, creating a track, as well as it provides information for identification of different physics objects. The charged particle traveling through the SMT and CFT leaves hits which are clustered and analyzed to reconstruct the trajectory of the particle. There are two algorithms used in this procedure: Histogramming Track Finder[24] (HTF) and Alternative Algorithm[25] (AA). Both algorithms use method called a Kalman filter[26] to reduce the dependence of the tracking algorithm on noise in the tracking systems.

The Histogram Track Finder

The magnetic field causes a charged particle to travel on a circular orbit, the curvature

of which is calculated as $\rho = qB/p_T$, where q is a charge of the particle, B is a magnetic field, and p_T is a transverse momentum of the particle. The position of the charged particle in each (x,y) point is defined by the ρ, DCA, that is a notation for a distance of closest approach or a distance between the particle's trajectory and the beam line in the $x - y$ plane, and ϕ, the azimuthal angle measured at the DCA. The HTF maps are collections of all possible circles corresponding to a given (x,y) point into a straight line in $\rho - \phi$ plane. A two-dimensional histogram ($vs.\rho\_\phi$) is filled for every hit. The bin with the highest number of entries defines the collection of hits belonging to the same track. To improve the quality of selected tracks the Kalman filter is applied which removes fake tracks or tracks with small number of hits in the detector.

The Alternative Algorithm

The AA method starts from the innermost layers of the tracking system, the SMT layers, and gradually moves outward. At first it finds a hit in the SMT barrel or "F-disks", then it searches for a second hit from the SMT layers, separated from the fist one in $\Delta\phi < 0.08$. Finally, the program further searches for the third hit, that would satisfy the requirement of forming a circle with the previous two hits. The circle must have a radius greater than 30 cm, DCA < 2.5 cm, and the quality of the fit must satisfy $\chi^2 < 16$ requirement. If more than one combination of these triplet hits is found, the Kalman filter is used to extrapolate all possible candidates to the following layers of the central tracking system. A new hit, found within a small window around the extrapolation, is included only if recalculated χ^2 is still less than 16. If more than one hit found in the small window two track hypothesis are made. The algorithm continues until all layers considered or at least three adjacent layers are found with no hits. Any two tracks must not share more than 2/3 of their hits between them. The final track candidate is chosen out of pool of candidates based on several criteria, such as the total number hits, number of layers with no hits, and χ^2. In case no hits found in the SMT, the preliminary vertex is reconstructed and is used by the AA algorithm together

with the CFT hits. At the last step, duplicate tracks are removed from the track list.

4.2 Primary Vertex Reconstruction

The point is the $x-y-z$ space where the $p\bar{p}$ collision takes place is called a vertex. There can be more than one vertex in per bunch crossing, which depends on the instantaneous luminosity. The width of the distribution of vertices in the $x-y$ plane is $\sigma_r = 40$ μm, while along the beam line it is $\sigma_z = 28$ cm. The vertex of the $p\bar{p}$ hard scatter collision from which an event of our interest was generated is called primary vertex (PV). It is very important to distinguish the PV from other vertices in the events, produced from the additional $p\bar{p}$ interactions, so-called minimum bias (MB) interactions, as the location of the PV is further used in calculation of the momentum of outgoing particles as well as the missing transverse energy in the event.

The PV vertex reconstruction uses tracks from Section 4.1 that satisfy requirements $p_T > 0.5$ GeV, at least two SMT hits and $\Delta z < 2$ cm. Then three major procedures are performed:

- The tracks in this collection are fit to find the best location for a vertex. If χ^2/ndf of the fit is greater than 10, the tracks, worsening the χ^2, are removed one by one and the remaining tracks re-fit after every removal until $\chi^2/ndf \leq 10$ requirement is satisfied. All removed tracks are considered in the same manner to find other collision vertices. All vertices found are used to determine a width and a location of the beam collision point, or a beam spot.

- Out of tracks in each group, the ones with $|\mathrm{DCA}| > 5\sigma_{\mathrm{DCA}}$ are rejected and the Kalman filter is used to find the final location of the vertex.

- The final step is to distinguish which vertices are from MB interactions and which one is a primary vertex. The tracks from the MB interaction tend to be softer, *i.e.*, with low transverse momentum than ones from hard scattering. The probability of

being originated from the MB interaction is calculated for each track, using its p_T. The product of probabilities for all tracks associated with a given vertex gives the probability of being a MB vertex (P_{MB}). The vertex with the lowest P_{MB} is selected as a primary vertex.

4.3 Electron and Photon Reconstruction

As mentioned previously, electrons and photons are called collectively as electromagnetic objects. Similarly, they both shower and deposit almost all their energies in the electromagnetic layers of the calorimeter. The major difference between these two particles is that the electron leaves track when passing through the central tracking system, while the photon is trackless. The latter plays an important role to distinguish electrons and photons in data analyses.

The EM showers from electron and photon are developed similarly, governed by the bremsstrahlung ($e \rightarrow e\gamma$) and conversion ($\gamma \rightarrow e^+e^-$) processes. The shower develops both in the longitudinal and transverse directions. The longitudinal development of the shower is characterized by a radiation length (X_0), a distance traveled by an electron in the matter before emitting a photon. The shower in the transverse direction is parameterized by the Molirère radius (R_M), which is as a radius of a cylinder that contains about 90% of energy deposition from the shower [1]. Approximately, 20-22X_0 and 3.5R_M are taken as the length and width of the shower, that contain ∼98% of the total energy.

A Simple Cone Algorithm[27] is used to reconstruct clusters of energy depositions in the calorimeter. It finds the calorimeter towers with $E_T > 0.5$ GeV as seeds and draws a cone with $R = 4$ around each seed. All the calorimeter towers within this cone are added to the seed and energy-weighted position of the cluster in the $\eta - \phi$ plane is recalculated each time. This new position is taken as the position of the cluster, new cone is drawn around it, and algorithm is performed until all towers are checked. The tower is kept if its total energy

[1] Both X_0 and R_M are characteristic constants of the material. They are related as $R_M = 0.0265X_0(Z + 1.2)$, where Z is the atomic number of the given matter.

exceeds 1.5 GeV and $fr_{\rm EM} > 90\%$. Here, $fr_{\rm EM}$ (EM-fraction) is defined as follows:

$$fr_{\rm EM} = \frac{E_{\rm EM}(0.2)}{E_{\rm total}(0.2)}, \tag{4.1}$$

where $E_{\rm EM}(0.2)$ is the electromagnetic energy of a cluster contained in a cone of radius $R = 0.2$, while $E_{\rm total}(0.2)$ is a total energy, sum of both EM and HAD energies, in the same cone.

As a next step, a calorimeter isolation variable ($\mathcal{I}$) is calculated for each cluster.

$$\mathcal{I} = \frac{E_{\rm total}(0.4) - E_{\rm EM}(0.2)}{E_{\rm EM}(0.2)}, \tag{4.2}$$

where $E_{\rm total}(0.4)$ is the total energy in a cone of radius $R = 0.4$ and $E_{\rm EM}(0.2)$ is the same as defined in Eq. 4.1. The requirement $\mathcal{I} > 0.2$ indicates that the most of the energy in a cluster is of hadronic origin and the cluster is kept only if $\mathcal{I} < 0.2$.

The energy measured at the calorimeter (E^{meas}) is expected to be different, systematically lower, from the true energy (E^{true}) of the particle. It is reflected clearly in dielectron mass resonance ($Z \rightarrow ee$) which is found to be sifted to lower side compare to the Z boson mass peak from previous precision measurements[28,29]. Due to this, an energy scale correction is applied on selected cluster candidates, following an assumption that

$$E^{meas} = \alpha E^{true} + \beta. \tag{4.3}$$

Here, α and β are energy scale and energy offset, determined for CC and EC clusters separately using a binned maximum likelihood method. Those are then applied in Eq. 4.3 to obtain the corrected energy of the cluster.

The EM-fraction and isolation are quite efficient to select good quality EM clusters, however additional variables and thresholds are defined and applied that allow significantly improve the purity of the selected objects used in the analysis. These variables are described below:

- **ID** The EM cluster can be later matched to a track reconstructed from the central tracking system. If such track is found the cluster is assigned an ID = $\pm$11, a sign indicating the charge of the track, and the cluster without a track match has ID = 10.

- **EM-fraction** $fr_{\rm EM} > 0.9$ is a basic requirement to select the EM cluster. EM shower is expected to deposit ∼100% of its energy in the EM section of the calorimeter. The tighter requirement, *e.g.* $fr_{\rm EM} > 0.97$, allows to select clusters, with almost no activity in hadronic layers of the calorimeter.

- **Isolation** Similar to the EM-fraction, more stringent requirement, such as $\mathcal{I} < 0.15$, can be used in the analysis.

- **Shower width** The width of the EM cluster at the third layer of the EM calorimeter is used to identify clusters produced by EM particles. For the clusters in central calorimeter only the width in $r-\phi$ plane, σ_ϕ, is used with a flat upper threshold of 14-18 cm^2. While for clusters in endcap calorimeter both σ_ϕ and the width in z direction, σ_z are applied and the thresholds vary with the pseudorapidity of the cluster:

$$\sigma_\phi < 7.3|\eta|^2 - 35.9|\eta| + 45.7 \tag{4.4}$$

$$\sigma_z < 7.5|\eta|^2 - 36.0|\eta| + 44.8. \tag{4.5}$$

- **H-Matrix** The $HMx7$ and $HMx8$ use 7 and 8 variables, respectively, to discriminate between electromagnetic and hadronic showers. These variables are shower energy fraction in four EM layers of the calorimeter, σ_ϕ, total shower energy, the position of the primary vertex, for $HMx7$ and an additional σ_z used in $HMx8$ only. Using a MC sample of N electrons the covariance matrix (M_{ij}) is constructed to determine an expected shower shape

$$M_{ij} = \frac{1}{N}\sum_{n=1}^{N}(x_i^n - \bar{x}_i)(x_j^n - \bar{x}_j), \tag{4.6}$$

where x_i^n is the value of variable i for the n^{th} MC electron and $\bar{x}_i$ is an expectation value of variable i. The H-Matrix is defined as the inverse of their covariance matrix, $\mathrm{H} \equiv \mathrm{M}^{-1}$. Then, the $\chi^2_{H-Matrix}$ is determined as

$$\chi^2_{HMx} = \sum_{ij}^{7\ or\ 8}(x_i - \bar{x}_i)H_{ij}(x_j - \bar{x}_j), \tag{4.7}$$

where, x_i is the value of variable i for the EM cluster being evaluated. The H-Matrix variables for real EM showers are smaller than those for showers from jets, and that allows distinguishing jets from true EM clusters.

- **Track Match** The matching between the EM cluster and a track from the central tracking system can be done in two ways, so-called *spatial track match* ($\chi^2_{spatial}$) and *track match* (χ^2) defined by following formulae:

$$\chi^2_{spatial} = \left(\frac{\Delta\phi}{\sigma(\phi)}\right)^2 + \left(\frac{\Delta z}{\sigma(z)}\right)^2 \tag{4.8}$$

and

$$\chi^2 = \chi^2_{spatial} + \left(\frac{E_T/p_T - 1}{\sigma(E_T/p_T)}\right)^2. \tag{4.9}$$

Here, $\Delta\phi$, Δz and σ_ϕ, σ_z are separation and resolution in ϕ and z coordinates between the position of the EM cluster at the third layer of the calorimeter and the central track, respectively. The last term in Eq. 4.9 places constraints on the ratio of the energy of EM cluster and track momentum taking into account the resolution of this ratio $\sigma(E_T/p_T)$.

- **Hits-on-the-Road (HoR)** This variable is defined as the probability of an EM object to have a track based on the density of hits in the central tracker. Often this variable is logically OR-ed with the spatial track match probability, *e.g.* ($\chi^2 > 0.001$ OR $HoR > 0.4$).

- **Track Isolation** This variable allows to distinguish between tracks from EM objects and ones produced by hadrons, traversing the tracking system. In the latter case the higher activity is expected in the tracker around the track associated to the EM object. The track isolation $IsoHC4$ is defined as sum of p_T of all reconstructed tracks in an annulus of $0.05 < \Delta R < 0.4$ around the EM cluster.

- **Electron Likelihood** The electron likelihood[30] ($Lhood8$) uses 8 variables: EM-fraction, $HMx7(8)$, E_T/p_T, $\chi^2_{spatial}$, DCA from the PV, number of tracks in a cone of

$R = 0.05$, and a sum of p_T of all tracks in a cone of $R = 0.4$. For each variable (x_i) the probability that an objects is an electron $P_e(x_i)$ or background $P_{bkg}(x_i)$ is calculated. Then, the likelihood that an object is an electron is evaluated as follows:

$$\mathcal{L}(x) = \frac{\prod_{i=1}^{8} P_e(x_i)}{\prod_{i=1}^{8} P_e(x_i) + \prod_{i=1}^{8} P_{bkg}(x_i)} \tag{4.10}$$

4.3.1 Reconstruction of electrons in ICR

Good understanding of the DØ detector allows us to make use of the electrons reconstructed in the inter-cryostat region, referred in the following as ICR electrons e_{ICR}. There is only a limited coverage of electromagnetic calorimeter in pseudorapidity range $1.1 < |\eta| < 1.5$ of the ICR detector. As a result, the electron does not shower enough and leaves a narrow cone of energy, with the major fraction of it identified as a non-EM energy. This signature is similar to the signature from tau leptons. Due to this, ICR electron is reconstructed first as a tau object, with $E_T > 10$ GeV, that is matched to a track from the central tracker, with $p_T > 20$ GeV. The ICR electrons are further required to pass the neural network discriminants that uses cluster's shower shape and associated tracking information. to reject more background due to hadrons.

4.4 Jet Reconstruction

An emitted parton at the hard interaction, such as quark and gluon, undergoes fragmentation and hadronization processes and appears as a group of hadrons commonly called a jet. The total momentum of hadrons in a jet is close to the momentum of the emitted parton. The jets vary widely in shape and particle content, but, while traveling through the detector, usually they all shower in the EM and HAD layers of the calorimeter that are accompanied by many tracks in the central tracking system. The most typical hadrons found in jets are both neutral and charged pions.

The jets are reconstructed using the Run II Cone Algorithm[31]. Only the cells with the energy greater than 2.5 times of the width of the electronic noise in the calorimeter are

considered. At first, the algorithm clusters the calorimeter cells into a tower and calculates its four-momentum that is the sum of four-momenta of all cells in the tower. Then, the Simple Cone Algorithm is used to reconstruct jet pre-clusters and select only ones with $p_T > 0.5$ GeV. The leading-p_T pre-cluster is selected as a seed and any item with $p_T > 1$ MeV and separated from the pre-cluster seed by $\Delta R < 0.3$ is added to it. The process iterates until all pre-clusters are considered and produces in the list of pre-clusters with decreasing p_T.

The pre-clusters are seeds for the Run II Cone Algorithm which constructs proto-jets with radius of 0.5 or 0.7 in rapidity-azimuthal ($y - \phi$) space. The pre-cluster is selected as a seed if the distance between it and the closest proto-jet is greater than half of the cone radius. All the pre-clusters within a cone of proto-jet are added and centroid weighted mean is recalculated each time. This process iterates until the change in mean is less than ΔR <0.001 or the list of pre-clusters are looped over 50 times. To suppress sensitivity to the soft radiation the midpoints between two proto-jets are added as seeds.

At last, all produced proto-jets are passed to the merging and splitting part of the Run II Cone Algorithm. The proto-jets are ordered by decreasing p_T. For each one the algorithm calculates p_T of the pre-clusters shared with any other proto-jet. If more than 50% of total p_T is shared the two proto-jets are merged. Otherwise, the proto-jets are split, by requiring that each one to be assigned only to its closest proto-jet in $y - \phi$ space and the list is reordered.

4.5 Muon Reconstruction

For the muon reconstruction information from the wire chambers and scintillation counters of the muon system as well as hits in the central tracking system are used. At first, the track in muon system, so-called a local track, is reconstructed. The hits in two or more decks of the A layer of the drift tubes are fit to form the segment of a track. The B and C layers are considered together and the similar fitting procedure is applied. If there is

more than one possibility of a track segment in A and BC layers one with better fit, *i.e.*, a smaller value of χ^2, is used. The next is to fit track segments at A and BC layers. The fit goes through the toroid magnet (see Section 3.2.6) and takes into account the bent of the muon traversing a magnetic field. This gives a local muon candidate whose momentum is determined by the curvature of its trajectory. However, the local muon track cab be matched to the track from the central tracking system that will allow to improve the muon momentum measurement. This matching is performed by extrapolating the local muon track inward, modeling minimum ionizing interaction with the calorimeter, and fitting to a central track.

In addition, to improve the quality of selected muons in the analysis, the isolation in the calorimeter ($etHalo$) and tracker ($etTrkCone5$) are defined as follows:

$$etHalo = E_T^{cal}(0.4) - E_T^{cal}(0.1) \tag{4.11}$$

$$etTrkCone5 = p_T tracks(0.5) - p_T(\mu), \tag{4.12}$$

where $E_T(0.4)$ ($E_T(0.1)$) is the transverse energy in all layers of the calorimeter inside a cone of radius 0.4 (0.1) around the muon track and $p_T^{tracks}(0.5)$ is the sum of p_Ts of all tracks inside a $R = 0.5$ cone and $p_T(\mu)$ is the muon momentum. The requirement of an upper threshold on these variables allows distinguishing between prompt muons, produced at the hard scatter, and muons originated from semi-leptonic decays of heavy flavor quarks in jets.

4.6 The $\not\!\!E_T$ Reconstruction

At hadron colliders the collisions happen between the partons comprised inside the initial state hadrons rather than hadrons directly. The complexity of hadron collisions is that the momenta carried by the colliding partons are not known initially. Thus, at the first sight, the momentum conservation cannot be applied. However, as the p and $\bar{p}$ beams are well steered and focused, almost all collisions at the Tevatron happen at a very small angle to the beam line, thus the initial momentum in the transverse $x - y$ plane is almost zero. Accordingly,

the vector sum of momentum of outgoing particles in the $x-y$ plane must be also close to zero. Thus, an important information can be revealed by calculating the imbalance of final state transverse energy ($\not{E}_T$)[32] in the event. A significant non-zero value of the $\not{E}_T$in the event indicate a production of weakly interacting particle, such as neutrino, or some of the exotic non-interacting particles, predicted by some extensions of the standard model.

The energy depositions in the calorimeter cells, except for the coarse hadronic layers, are used to calculate x and y components of total missing transverse energy in the event, see Eq 4.13.

$$\not{E}_{Tx} = -\sum_{i}^{N_{cells}} E_{Ti} cos(\phi_i),\ \not{E}_{Ty} = -\sum_{i}^{N_{cells}} E_{Ti} sin(\phi_i), \tag{4.13}$$

where E_T is calculated according to Eq. 3.7. Then, the missing transverse energy is calculated as follows:

$$\not{E}_T = \sqrt{\not{E}_{Tx}^{\ 2} + \not{E}_{Ty}^{\ 2}}. \tag{4.14}$$

This calculation does not take into account a potential presence of muons in the event, as those do not shower in the calorimeter. As muons carry some fraction of the initial momentum, the $\not{E}_T$is further corrected using the p_T of the muon's track. Additional corrections are also applied due to jet and EM object energy scales before using the missing transverse energy in the analysis.

Chapter 5

Measurement of the WZ Cross Section

The analysis of the WZ process with DØ data is described in the next several Chapters of this Dissertation. I first describe the measurement of the $p\bar{p} \to WZ$ production cross section below.

5.1 Data and MC Samples

In this measurement the DØ Run IIa and IIb data sets, collected between October 2002 and December 2008, are used. Data are first preselected (skimmed) by the Common Sample Group (CSG)[33] by selecting only events containing certain physics objects. As WZ leptonic decay process have multiple number of leptons in the final state 2EMhighpt, 2MUhighpt, and EMMU skims are used in this study. The collision events with at least two electromagnetic (muon) objects with $p_T > 15$ GeV are selected to produce the first (the second) skim, while the events with at least one muon and one EM object with $p_T > 15$ GeV are required for the third skim. The skims are further centrally processed by the Common Analysis Framework (CAF)[34] that allows selection of the physics objects described in the previous Chapter.

The events are required to satisfy standard DØ data quality (DQ) requirements to reject noisy collision events or remove events with malfunctioning sub-detector components. After application of these standard selection criteria, data correspond to 4.1 fb^{-1} of integrated

luminosity.

In this analysis the Monte Carlo (MC) simiulation of the WZ signal is used to estimate the geometrical acceptance of the selection criteria and to perform detailed study of systematic uncertainties in the analysis.

As mentioned above, the WZ production is a rare process, and it can easily be mimicked by so-called background processes, *i.e*, processes that have similar experimental signature as the signal. The major background is from processes with a genuine Z boson plus an additional object misidentified as a lepton from the W boson decay. These processes are $Z + jets$, ZZ, and $Z\gamma$. A small background contribution from $W + jets$ is included in the $Z + jets$ background. Therefore, I collectively refer to these processes as the $V + jets$ background. An additional but small background is from the $t\bar{t}$ process. The $V + jets$ and $Z\gamma$ backgrounds are estimated from data (see Section 5.4), while the ZZ and $t\bar{t}$ backgrounds are determined from the MC simulation.

All MC samples, used in this analysis, are officially produced by the CSG using the CTEQ6L1 parton distribution function (PDF)[35] set. Diboson production samples are generated using PYTHIA[36] generator and the $t\bar{t}$ production is generated using $m_{top} = 172$ GeV using ALPGEN[37] interfaced to PYTHIA for appropriate hadronization and showering. All MC samples are passed through a full GEANT[38] simulation of the D0 detector. Those are then properly re-weighted for instantaneous luminosity profile in data, the position of the beam, and normalized to the next-to-leading order (NLO) cross sections. The MC samples used for Run IIa and Run IIb are listed in Table 5.1.

5.2 Object Selection

The physics objects used in this analysis are electrons, muons, and missing transverse energy. In addition to electrons reconstructed using standard algorithms in the CC and EC, this study includes electrons identified in the ICR. This increases the geometrical acceptance of the final state and improves the precision of the measurement. Although the ICR electron

Process	Events before DQ	$\sigma_{NLO} \times Br$ (pb)
Run IIa		
$WZ \rightarrow 3l\nu$	188412	0.1064
$ZZ \rightarrow incl$	590647	1.334
$t\bar{t} + 0lp \rightarrow 2l2\nu2b + 0lp$ excl.	1516107	0.449
$t\bar{t} + 1lp \rightarrow 2l2\nu2b + 1lp$ excl.	963057	0.189
$t\bar{t} + 2lp \rightarrow 2l2\nu2b + 2lp$ incl.	701167	0.144
Run IIb		
$WZ \rightarrow 3l\nu$	363320	0.1064
$ZZ \rightarrow incl$	540273	1.334
$t\bar{t} + 0lp \rightarrow 2l2\nu2b + 0lp$ excl.	749642	0.490
$t\bar{t} + 1lp \rightarrow 2l2\nu2b + 1lp$ excl.	452177	0.198
$t\bar{t} + 2lp \rightarrow 2l2\nu2b + 2lp$ incl.	281453	0.094

Table 5.1: *MC samples used in analysis.*

identification is very novel for DØ data analyses, the resolution of the ICR is reasonably well modeled by the MC. The muon track over-smearing with an additional Landau term is applied to account for the additional radiative losses of the electron. However, as background discrimination for ICR electrons is worse compared to that for CC and EC electrons, only candidate events with an ICR electron associated with the Z boson decay are considered.

Thus, the WZ candidate events are split into the following six distinct experimental signatures (sometimes referred to as decay signatures or channels):

- $eee\nu$
- $ee\mu\nu$
- $\mu\mu e\nu$
- $\mu\mu\mu\nu$
- $ee_{ICR}e\nu$, where one lepton of the Z boson is in the ICR
- $ee_{ICR}\mu\nu$, where one lepton of the Z boson is in the ICR

The identification criteria used in this analysis to identify the decay products from W and Z bosons are all the standard DØ criteria. That allows to use officially obtained reconstruction and identification efficiencies and uncertainties.

The leptons from W and Z boson decays, so called signal leptons, can be mimicked by the different objects or by the leptons that are not produced by the signal process. For example, jet can produce significant energy deposit in EM calorimeter due to the decay $\pi \rightarrow \gamma\gamma$ that can be associated to a track from another charger particle within the jet. As a result, it might be reconstructed as an electron. Another example is a false muon signal from punch-through pions, *i.e.* pions that are energetic enough to penetrate through the calorimeter and reach the muon system. In addition to this, leptons from other decay processes can be selected as the WZ boson decay products. For instance, such processes are semileptonic decays of heavy flavor quarks or decays of pions contained in jets (*e.g.* $\pi \rightarrow \mu\nu_{\mu}$). In these cases the leptons are expected to be non-isolated and can be discriminated from the signal leptons. Electrons have additional source of background due to presence of photons. This can happen due to the $\gamma \rightarrow e^{+}e^{-}$ process when one of the leptons from the conversion is selected as a signal electron. In addition to this, a track mis-match to the energy cluster in the EM calorimeter, produced by the photon, can create a false electron candidate.

In order to diminish the misidentification of signal leptons due to the processes described above the identification criteria for electrons and muons are further optimized. The leptons from the Z boson decay have smaller chance to be misidentified than the lepton from the W boson decay due to an additional constraint on di-lepton invariant mass to the nominal Z boson mass. As a result, more stringent identification requirements are applied to the leptons from the W boson decays. For optimization purposes DØ utilizes different categories for lepton identification criteria. These criteria range from very efficient but with minimal background rejection capability, that is often referred to as loose selection, to the stringiest that is not so efficient but has the highest background discriminating power, so-called tight selection.

The efficiency of the lepton identification is measured by a so-called "$tag-and-probe$" method using $Z \rightarrow \ell\ell$ events. The Z boson production is a source of same-flavor genuine leptons and invariant mass constraint allows us to select a very pure dilepton sample. At first, a tight quality lepton, referred to as tag, is found in an event. Then, a loose quality lepton, probe lepton, is searched for with the requirement that the invariant mass of tag and probe lepton pair is consistent with the nominal Z boson mass. Using these events from $Z \rightarrow \ell\ell$ sample, a probability that the probe leptons will also satisfy the tight selection criteria yields the relative identification efficiency. As the DØ detector is not homogeneous, the lepton identification efficiency depends on its geometry. As a result, most commonly, the lepton identification efficiency is parameterized as a function of pseudorapidity with respect to the detector origin, so-called η_{det}, and azimuthal angle ϕ. The identification efficiency can also depend on different variables, such as lepton p_T or instantaneous luminosity. Sometimes, this dependence is also taken into account and efficiency is calculated in three-dimensional (3D) parameterization given that there is enough statistics in $Z \rightarrow \ell\ell$ sample. In this analysis, the 2D parameterization, $vs.$ $\eta_{det} - \phi$, of the identification efficiencies are used and additional effects are assigned as systematic uncertainties. The lepton identification efficiencies are usually calculated centrally by the DØ Object Identification groups and stored in so-called SPC files.

The detailed identification criteria for final state leptons are described below.

5.2.1 Electron Identification

The several discriminating variables, described in Section 4.3, are used to define different categories of electron identification at DØ. In this analysis, the electrons from the Z boson decay must satisfy "$MLoose1$" selection criteria. The electron from the W boson decay is identified differently depending whether it is in CC or EC. That is due to the limited coverage of the central tracker in the forward region resulting in larger number of false electrons in EC. Therefore, electron in CC must be of "$Medium$" quality, while one in EC must satisfy

"Tight" selection criteria. The details of these categories are summarized in Tables 5.2 and 5.3 together with the loosest selection criteria for electrons, so-called *"VLoose"*. The definitions in EC also have cuts on shower shape variables, σ_ϕ and σ_z, as given in Eqs. 4.4. The efficiencies for different electron definitions used in the analysis as a function of η_{det} and ϕ are shown in Fig. 5.1.

Variables	*"VLoose"*	*"MLoose1"*	*"Medium"*
$\mathcal{I}$ <	0.10	0.10	0.07
fr_{EM} >	0.95	0.97	0.97
$IsoHC4$ <	3.5	2.5	2.5
$HMx7$ <	35	25	25
$NNout7\_cc$ >	–	0.2	0.6
$Lhood8$ >	–	–	0.2
$\chi^2_{spatial}$ >	–	0.001	0.001
or HoR >	–	0.4	0.5

Table 5.2: *Selection criteria used to select "VLoose", "MLoose1", and "Medium" quality electrons in CC.*

Variables	*"VLoose"*	*"MLoose1"*	*"Medium"*
$\mathcal{I}$ <	0.10	0.10	0.07
fr_{EM} >	0.95	0.95	0.97
$IsoHC4$ <	3.5	2.0	2.0
$HMx8$ <	35	15	15
$NNout3\_ec$ >	–	0.4	0.4
$\chi^2_{spatial}$ >	–	–	0.0

Table 5.3: *Selection criteria used to select "MLoose1" and "Tight" quality electrons in EC.*

5.2.2 ICR Electron Identification

An ICR electron in this analysis is identified as track matched tau object (see Section 4.3.1) that satisfy following requirements:

- E_T >10 GeV

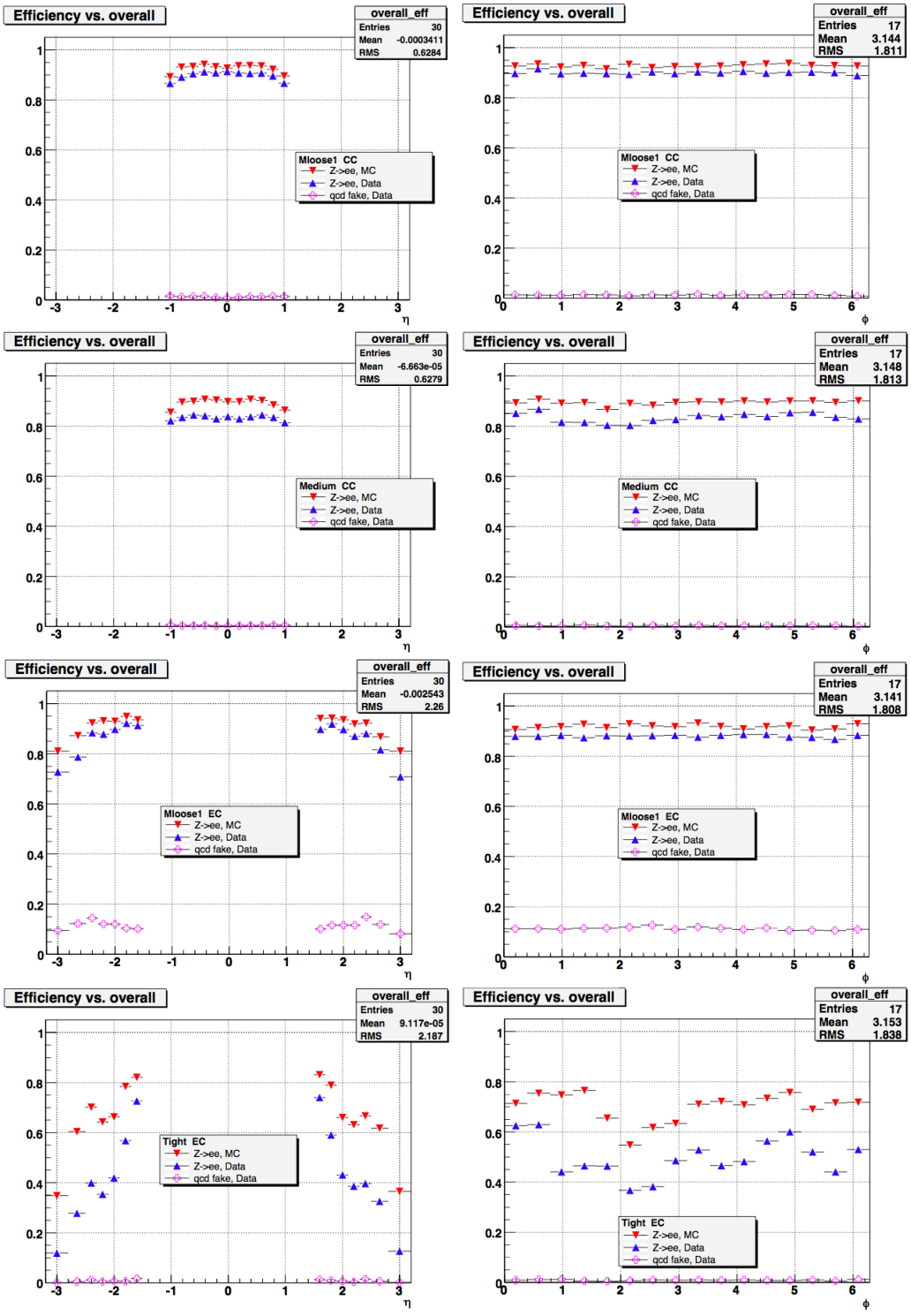

Figure 5.1: *Efficiency in data and MC vs. electron η_{det} (left) and ϕ_{det} (right). The first four distributions correspond to "MLoose1" and "Medium" definitions in CC, while the last four plots – to "MLoose1" and "Tight" definitions in EC.*

- $1.1 < |\eta_{det}| < 1.5$
- $p_T^{track} > 20GeV$
- Track is extrapolated to the calorimeter and is required to satisfy $1.1 < |\eta_{trkxtrp}| < 1.5$
- Track must have at least 1 SMT hit.

The tau hadronic neural net (NNh) is used to remove additional background from jets. Based on this cut three qualities of ICR electron is defined. This ICR electron is required to pass the ICR "$Medium$" quality requirements, $NNh > 0.7$. The efficiencies for track match to ICR electron and "$Medium$" quality NNh criterion are given in Figs. 5.2.

5.2.3 Muon Identification

The muons are defined in different types, qualified by a number of segments ($nseg$). The muon types are summarized in Table 5.4. The quality of a muon is defined based on $nseg$, number of hits in the wire chambers and scintillation counters, and a goodness of a match to a central track. Here, the central track must be identified as of "$Loose$" quality, *i.e.*, the muon track has $DCA < 0.2$ cm if $N_{SMT} = 0$ and $DCA < 0.02$ cm if $N_{SMT} > 0$, where N_{SMT} is number of SMT hits associated with the track. In this analysis, "$Medium$" quality muons are used, described in Table 5.5. To improve the quality of selected muons, additional isolation requirements are applied. The muons from the Z boson decay must satisfy so-called "$NPLoose$" isolation, $etTrkCone5 < 4.0$ GeV, while the muons from the W boson decay – "$NPTight$" isolation, $etTrkCone5 < 2.5$ GeV and $etHalo < 2.5$ GeV (see Section 4.5). The efficiencies for "$Medium$" quality muons, "$Loose$" tracks, and isolation requirements are shown in Fig. 5.3.

5.3 Event Selection

Candidate event selection is described below. Only events with at least one primary vertex within $\pm$ 60 cm around the detector origin are considered. Events must have at least

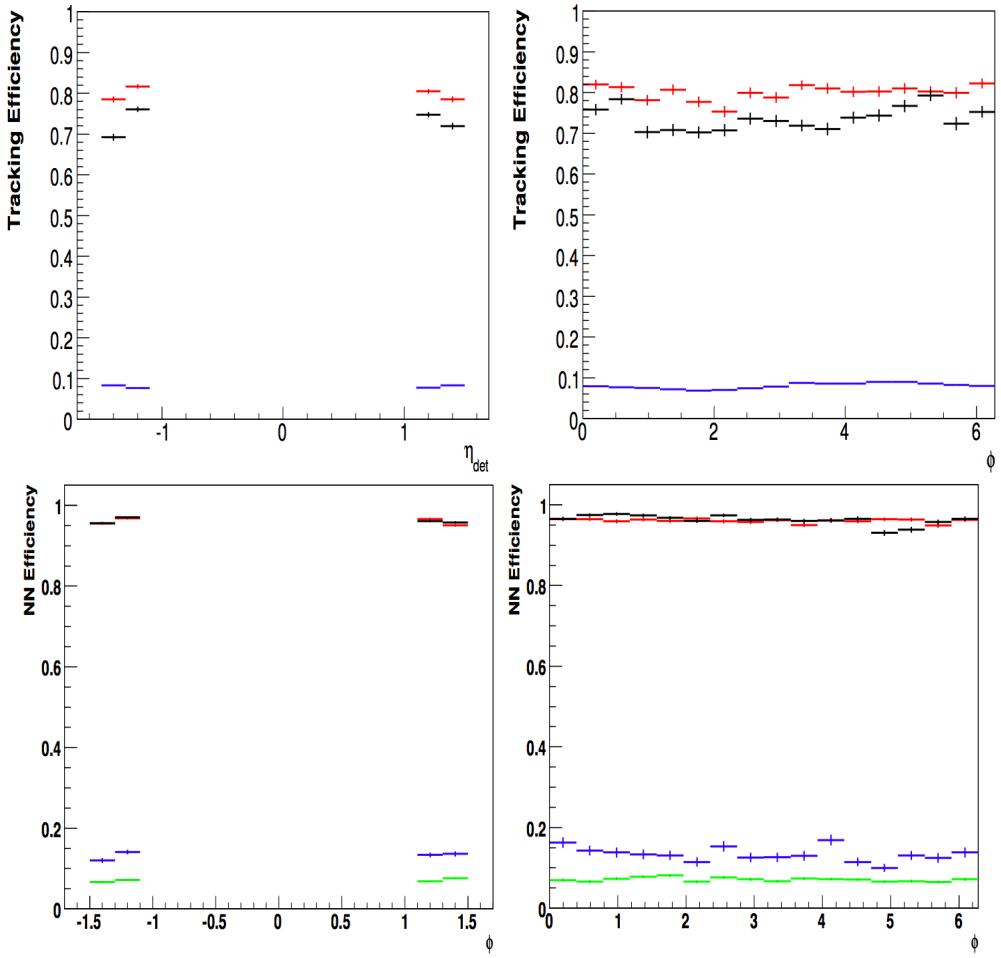

Figure 5.2: *Tracking efficiency in $Z \rightarrow ee$ data (black), $Z \rightarrow ee$ MC (red), and $\gamma + jet$ background data (blue) events vs. electron η_{det} (top left) and ϕ_{det} (top right). "Medium" NNh requirement efficiency in $Z \rightarrow ee$ data (black), $Z \rightarrow ee$ MC (red), $\gamma + jet$ background data (blue), and di-jet data events (green) vs. electron η_{det} (bottom left) and ϕ_{det} (bottom right).*

three energetic leptons, either electrons or muons, and significant missing transverse energy. Events are selected using the logical OR of single electron and/or the logical OR of single muon triggers. The single electron (muon) trigger implies at least one electron (muon) to be present in an event satisfying certain criteria in order the event to be recorder and used in analysis. Based on the criteria on electron (muon) different trigger terms are defined. The events in this study are selected using a logical OR of these trigger terms that significantly

nseg	Central track and muon system layers used
3	Central track + local muon track in A-, B-, and C-layer
2	Central track + local muon in B- and C-layers
1	Central track + local muon in A-layer
0	Central track + local muon hits
-1	Local muon in A-layer; no central track match
-2	Local muon in A- and B-layer; no central track match
-3	Local muon track in A-, B-, and C-layer; no central track match

Table 5.4: *The muon types.*

Muon quality	nseg	Number of hits
"$Medium$"	$\|nseg\| = 3$	$N_A^w \geq 2$, $N_A^{sc} \geq 1$, $N_{BC}^w \geq 2$, $N_{BC}^{sc} \geq 1$
"$Medium$"	$nseg = 2$	$N_{BC}^w \geq 2$, $N_{BC}^{sc} \geq 1$, located in octants 5 and 6 with $\|\eta\| < 1.6$
"$Medium$"	$nseg = 1$	$N_A^w \geq 2$, $N_A^{sc} \geq 1$, located in octants 5 and 6 with $\|\eta\| < 1.6$

Table 5.5: *The requirements for "$Medium$" muon quality.*

increases the trigger efficiency.

The trigger efficiency is estimated using officially produced $p_T - \eta_{det}$ and $\eta_{det} - \phi_{det}$ parameterization of single electron and single muon trigger efficiencies [1] using the following formula

$$\epsilon_{trigger} = 1 - \prod(1 - \epsilon_i), \tag{5.1}$$

where $\epsilon_{trigger}$ is the overall trigger efficiency for the event and ϵ_i is the trigger efficiency for a given lepton. Due to multiple, highly energetic leptons in the event the trigger efficiency is very high. It is estimated to be $\approx 98 \pm 2\%$ for each topology.

To identify WZ candidate events, at first the leptons from the Z boson decay are identified by selecting the same-flavor lepton pairs. As muon charge is identified very well at DØ, muon pairs are further required to have opposite electric charges.

The Z boson assignment for topologies that do not have ICR electrons goes as following. Out of all possible pairs, the pair with the invariant mass closest to the nominal Z boson

[1] Single electron (muon) trigger efficiencies are also calculated using the "$tag - and - probe$" method on $Z \to ee$ ($Z \to \mu\mu$) events in data. The efficiencies are obtained as a function of p_T and η_{det} (η_{det} and ϕ_{det}) and stored in SPC files.

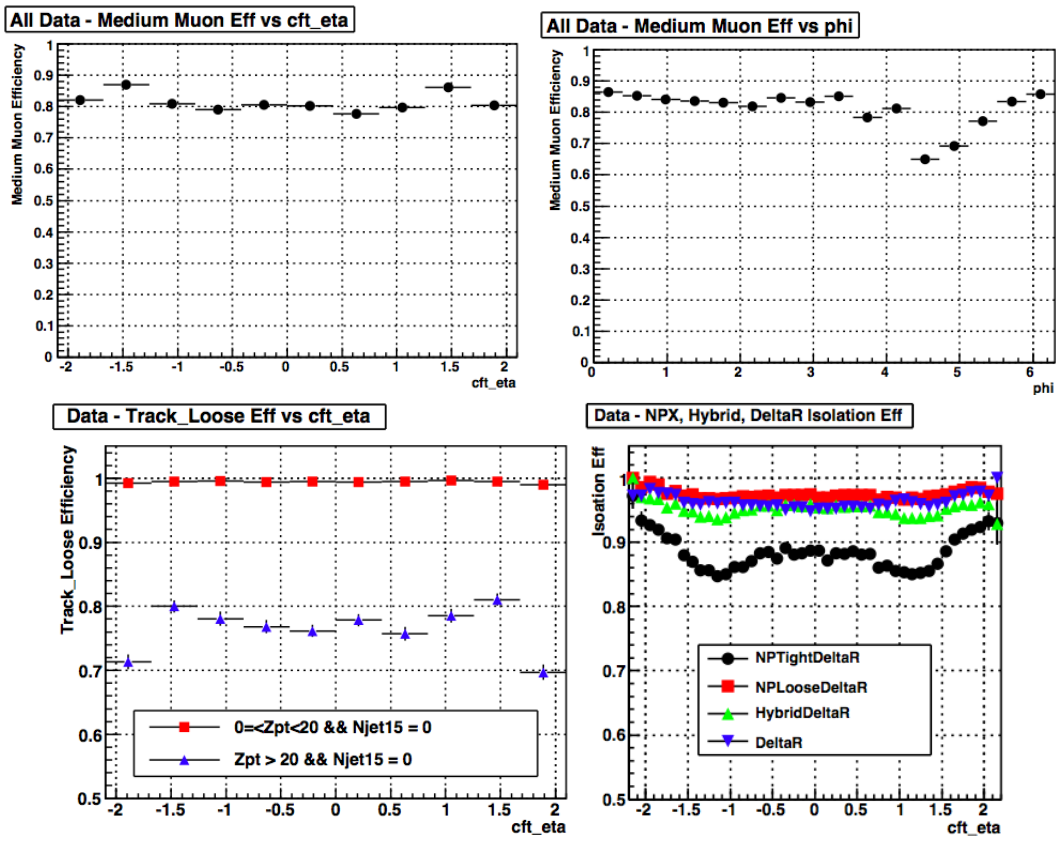

Figure 5.3: *The efficiency for "Medium" quality muons vs. η (top left) and ϕ (top right). The efficiency for selecting "Loose" track (bottom left) and different isolation requirements (bottom right).*

mass is selected and the leptons forming the pair are assigned as the Z boson decay products. This assignment is checked in MC simulation and found to be 100% correct for the channels with the Z and W bosons decaying to different flavor leptons. It is correct in 94% and 89% cases for eee and $\mu\mu\mu$ decay signatures, respectively.

The Z decay product assignment for the $ee_{ICR}\mu$ signature is unambiguous and thus, correct in 100% cases. In the case of $ee_{ICR}e$ channel, the following procedure is used to identify the Z boson decay leptons. Out of all possible, oppositely charged electron pairs, following mass differences are calculated: $|91\text{ GeV} - M_{ee}|$ for the pair electrons in CC or/and EC, and $|84.9\text{ GeV} - M_{ee}|$ [2] for the pairs with one ICR electron. The event is selected only if

[2]Mass window around 84.9 GeV is used due to a different energy scale for ICR electrons than for CC/EC

the pair with the ICR electron has the smallest mass difference. This assignment is checked and found to be correct in 85% cases.

Finally, out of the remaining leptons the lepton with the highest transverse momentum is selected as the W boson decay candidate.

The kinematic cuts and selection criteria are optimized according to $S/\sqrt{S+B}$ for each topology independently. Here, S is the expected WZ signal and is estimated from MC simulation, while B is the total background that comes from $V + jets$, ZZ, $Z\gamma$, and $t\bar{t}$ processes.

5.3.1 Selection of WZ candidates

The selection criteria for each experimental signature, obtained from the optimization, are summarized below.

Signatures with $Z \to ee$ decays

The electrons from the Z boson decay are required to be of "$MLoose1$" quality. In the case of the eee channel, the electron from the W boson decay must be of "$Medium$" quality if it is in the CC and "$Tight$" quality if it is in the EC. All three electrons must have a spatial track match probability greater than 0. For the $ee\mu$ channel, muons are required to pass "$Medium$" identification criteria, a "$Loose$" quality track and satisfy "$NPTight$" isolation criteria. The kinematic cuts to select $eee\nu$ events are given below:

- p_T of the most energetic electron from the Z decay must be greater than 30 GeV
- p_T of the two other electrons must be greater than 15 GeV
- $\not\!\!E_T > 25$ GeV
- 74 GeV $< M_{ee} <$ 108 GeV
- $\Delta R > 0.6$ between any two leptons

electrons[39,40].

- $\Delta z_{DCA} < 3$ cm between any two leptons' tracks

The kinematic requirements to select $ee\mu\nu$ events are:

- p_T of the most energetic electron from the Z decay must be greater than 30 GeV
- p_T of the two other leptons must be greater than 15 GeV
- $\not\!\!E_T > 20$ GeV
- 74 GeV $< M_{ee} <$ 108 GeV
- $\Delta R > 0.6$ between any two leptons
- $\Delta z_{DCA} < 3$ cm between any two leptons' tracks

Signatures with $Z \to \mu\mu$ decays

In both channels muons from the Z boson decay are required to be of "$Medium$" quality, have "$Loose$" track and satisfy "$NPLoose$" isolation. In the case of the $\mu\mu\mu$ channel, the muon from the W boson decay should be of "$Medium$" quality, with "$Loose$" track and satisfy "$NPTight$" isolation. For the $\mu\mu e$ channel, the electron must be of "$Tight$" quality in both the CC and EC regions. The electron is also required to have a spatial track match probability greater than 0. The kinematic cuts to select $\mu\mu e\nu$ events are given below:

- p_T of the most energetic muon from the Z decay must be greater than 20 GeV
- p_T of the two other leptons must be greater than 15 GeV
- $\not\!\!E_T > 25$ GeV
- 65 GeV $< M_{\mu\mu} <$ 115 GeV
- $\Delta R > 0.5$ between any two muons
- $\Delta R > 0.6$ between any two muons and the electron

- $\Delta z_{DCA} < 3$ cm between any two leptons' tracks

The kinematic cuts to select $\mu\mu\mu\nu$ events are:

- p_T of the most energetic muon from the Z decay must be greater than 20 GeV
- p_T of the two other muons must be greater than 15 GeV
- $\not\!\!E_T > 20$ GeV
- 65 GeV $< M_{\mu\mu} <$ 115 GeV
- $\Delta R > 0.5$ between any two leptons
- $\Delta z_{DCA} < 3$ cm between any two leptons' tracks

Signatures with $Z \to ee_{ICR}$ decays

The ICR electron is required to pass the "$Medium$" identification criteria, and all electrons in the EC must pass "$Tight$" quality selections. In the CC region, an electron from the Z boson decay must be "$Loose$" quality and from the W boson decay – "$Medium$" quality. The muon in the $ee\mu$ channel must be of "$Medium$" quality, have "$Loose$" track, and satisfy "$NPLoose$" isolation requirements. The kinematic cuts to select $ee_{ICR}e\nu$ events are given below:

- CC/EC electron $p_T > 15$ GeV
- ICR electron $p_T > 20$ GeV
- $\not\!\!E_T > 25$ GeV
- 60 GeV $< M_{ee} <$ 120 GeV
- The electrons from Z boson decay must have opposite charges
- $\Delta R > 0.5$ between any two leptons

- $\Delta z_{DCA} < 3.0$ cm between any two leptons' tracks

The kinematic cuts to select $ee_{ICR}\mu\nu$ events are:

- CC/EC electron $p_T > 15$ GeV
- ICR electron $p_T > 20$ GeV
- Muon $p_T > 15$ GeV
- $\not\!\!E_T > 20$ GeV
- 60 GeV $< M_{ee} <$ 120 GeV
- $\Delta R > 0.5$ between any two leptons
- $\Delta z_{DCA} < 3.0$ cm between any two leptons' tracks

In order to avoid any overlap between the eee and $ee_{ICR}e$ ($ee\mu$ and $ee_{ICR}\mu$) channels in MC samples, any ICR electron that is within ΔR <0.5 of a CC/EC electron is not considered.

5.3.2 Acceptance and efficiencies for event selection

The geometrical acceptance for the WZ signal is estimated with the MC simulation. The acceptance is measured on reconstructed events applying the kinematic cuts on selected objects, such as $z_{vtx} < 60$ cm, p_T thresholds, η, ΔR, mass window on the Z boson candidate, and $\not\!\!E_T$ requirement. The electrons and muons are selected as very loose quality objects: "*VLoose*" electrons are considered and muons must be of "*Loose*" quality with "*Loose*" track match. Both these requirements have > 95% efficiency. The acceptances for all channel and their uncertainties are summarized in Table 5.6. The systematic uncertainties are 5% due to the PDFs.

Channel	$Acc.$	ΔAcc (Stat.)	ΔAcc (Syst.)	ΔAcc
eee	0.0246	0.0003	0.0012	0.0012
$ee\mu$	0.0278	0.0003	0.0014	0.0014
$\mu\mu e$	0.0274	0.0002	0.0014	0.0014
$\mu\mu\mu$	0.0305	0.0002	0.0015	0.0015
$ee_{ICR}e$	0.0077	0.0001	0.0004	0.0004
$ee_{ICR}\mu$	0.0083	0.0001	0.0004	0.0004

Table 5.6: *Acceptances for each topology with statistical, systematic, and total uncertainties.*

Channel	ϵ	$\Delta\epsilon$	$Acc \times \epsilon$	$\Delta(Acc \times \epsilon)$
eee	0.4146	0.0532	0.0102	0.0014
$ee\mu$	0.4136	0.0336	0.0115	0.0011
$\mu\mu e$	0.3905	0.0448	0.0107	0.0011
$\mu\mu\mu$	0.4382	0.0478	0.0134	0.0013
$ee_{ICR}e$	0.4286	0.9469	0.0033	0.0004
$ee_{ICR}\mu$	0.5060	0.0415	0.0042	0.0004

Table 5.7: *The efficiency of the selection criteria and Acceptance $\times$ efficiency values for each topology with total uncertainties.*

The event selection efficiency is estimated by using the officially available SPC files for electron and muon identification efficiencies. The efficiency (ϵ) and product of the acceptance times efficiency ($Acc \times \epsilon$) for each decay signature are summarized in Table 5.7.

Systematic effects due to the misassignment of the W and Z boson decay products on the acceptance times efficiency values for the event selection criteria are estimated by comparing the $Acc \times \epsilon$ with the values estimated from MC truth information. The difference is measured independently for each final state signature and found to be of the order of 1%.

Another source of systematic uncertainty on $Acc \times \epsilon$ in $ee_{ICR}e$ and $ee_{ICR}\mu$ channels is a charge misidentification. Since the event selection requires two oppositely charged electron candidates from the $Z \rightarrow ee$ boson decay, differences between the charge misidentification rate in data and MC simulation can affect the acceptance. To test this effect, the weight of the events where the electron charge has been assigned incorrectly is increased by a factor of 5. This leads to a 5% change in the acceptance in this channel. A conservative 10%

uncertainty us assigned due to a potential misassignment in this final state signature. Due to large statistical uncertainties in the $ee_{ICR}e$ and $ee_{ICR}\mu$ final states, this has a negligible effect on the accuracy of the final, combined cross section of the WZ boson pair production.

An additional source of systematic uncertainty is the modeling of the WZ system that can affect on the $Acc \times \epsilon$. We rely on the WZ MC sample generated with PYTHIA in cross section measurement. However, more proper description of the NLO WZ diboson production is given with MCFM[41] generator. To estimate the effect due to the modeling of the WZ production in PYTHIA, the system p_T from PYTHIA WZ sample is reweighed by one from MCFM sample while the normalization of the sample is preserved. Then, this sample is used to calculate $Acc \times \epsilon$ for each signature. The difference is found to vary from couple of percent up to 5% for different final states. Thus, conservatively, 5% uncertainty is taken for all signatures.

5.4 Background Estimation

The methods used to estimate the $V + jets$ and $Z\gamma$ backgrounds are described below.

5.4.1 Vector Boson plus jets Background

A misidentified jet or genuine lepton produced from a semi-leptonic decay of a heavy quark in $V+jets$ process can be identified as a lepton from the WZ process. The contribution from this background is estimated in two steps. At first, the ratio of the number of objects that pass the W boson decay lepton identification requirements ("$true$" lepton) to the number of objects that pass a poorly-isolated ("$false$" lepton) requirement is measured in p_T or η_{det} bins, $\epsilon_f(p_T) = \frac{dN_{\text{“}true\text{”}}/dp_T}{dN_{\text{“}false\text{”}}/dp_T}$ or $\epsilon_f(\eta_{det}) = \frac{dN_{\text{“}true\text{”}}/d\eta_{det}}{dN_{\text{“}false\text{”}}/d\eta_{det}}$, using the multijet[42] sample in data. The definitions are constructed so that there is no overlap between the "$true$" and "$false$" lepton definitions, and that the "$false$" leptons are more likely to be misidentified jets or non-isolated leptons. Next, a normalization sample is produced by selecting the events with two "$true$" leptons, significant missing transverse energy, and additional lepton(s),

satisfying the "$false$" lepton selection criteria. Two of such "$true$" leptons are required to be identified as the Z boson decay products. The p_T (η_{det}) distribution of "$false$" leptons in the normalization sample is further multiplied by measured misidentification ratios, $\epsilon_f(p_T)$ ($\epsilon_f(\eta_{det})$). The integral of this product distribution gives an estimated $V+$ jets background.

Electron Misidentification Ratios

The events in the multijet sample, used to measure the lepton misidentification ratios, must be collected using a QCD trigger and have a high p_T jet, that is a trigger object, passing the following selection criteria:

- $p_T > 15$ GeV
- $|\eta_{det}| < 1.1$
- Satisfies jet identification requirements established by the Jet ID Group[43,44]

This ensures a trigger-unbiased estimation of the misidentification ratios. The event is further required to have a non-isolated electromagnetic object spatially separated from the trigger jet by $\Delta R > 1.57$. The electromagnetic object must satisfy the "$false$" electron definition given below

- EM fraction > 0.9
- Isolation < 0.15
- HMx7(8) > 35 in the CC (EC)
- $p_T > 15$ GeV
- $|\eta_{det}| < 1.1$ or $1.5 < |\eta_{det}| < 2.5$

In order to avoid signal contamination from $W \rightarrow e\nu$ candidates, *e.g.* $W + jets$ process, the $\not\!\!E_T$ is required to be less than 10 GeV. The misidentification ratios for the standard

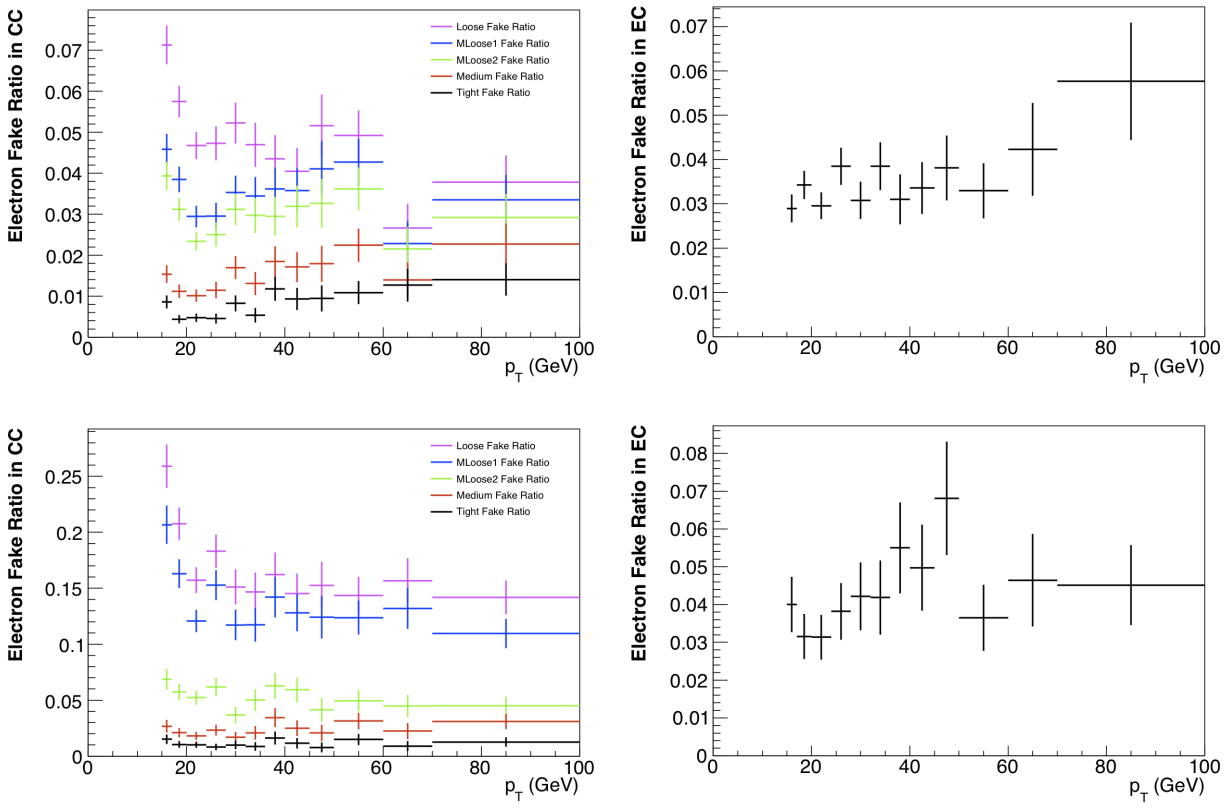

Figure 5.4: *The electron misidentification ratios vs. p_T for different identification criteria in CC (left) and for "Tight" electron misidentification ratio in EC (right). The first two plots correspond to Run IIa data and the next two plots correspond to Run IIb data.*

electron definitions ("*Loose*", "*MLoose*1", "*MLoose*2", "*Medium*", and "*Tight*") *vs.* p_T are shown in Fig. 5.4 for both Run IIa and Run IIb.

The misidentification ratios are obtained with no trigger requirements on the "$false$" electron. Therefore, to avoid a trigger bias, the ratios can be applied only in the case when W electron is not considered to fire a trigger, *i.e.* *eee* channel. To estimate the background contribution for the candidate events with the electron from the W boson decay to be a trigger object (such events are selected for $\mu\mu e$ and $ee_{ICR}e$ signatures), the rates are recalculated following the procedure described above with an additional trigger requirement that the selected events have also fired at least one of the single electron triggers. Obtained ratios are given in Fig. 5.5 for both Run IIa and Run IIb.

Muon Misidentification Ratios

A similar procedure is used to calculate the misidentification ratios for muons. Events with a high p_T jet, satisfying the jet requirements described in Section 5.4.1, are selected from the multijet data sample. These events are further required to have a muon candidate spatially separated from the trigger jet by $\Delta R > 1.57$ and $\not\!\!E_T < 10$ GeV. In this procedure a "$false$" quality muon is defined as follows:

- "*Loose*" quality
- "*Loose*" quality track
- $nseg > 0$
- $etTrkCone5 > 5$ GeV
- $p_T > 15$ GeV
- $|\eta_{det}| < 2$

The misidentification ratios are measured as a function of the pseudorapidity η of muon candidate. The ratios for "*Medium*" quality muons with all possible combination of track

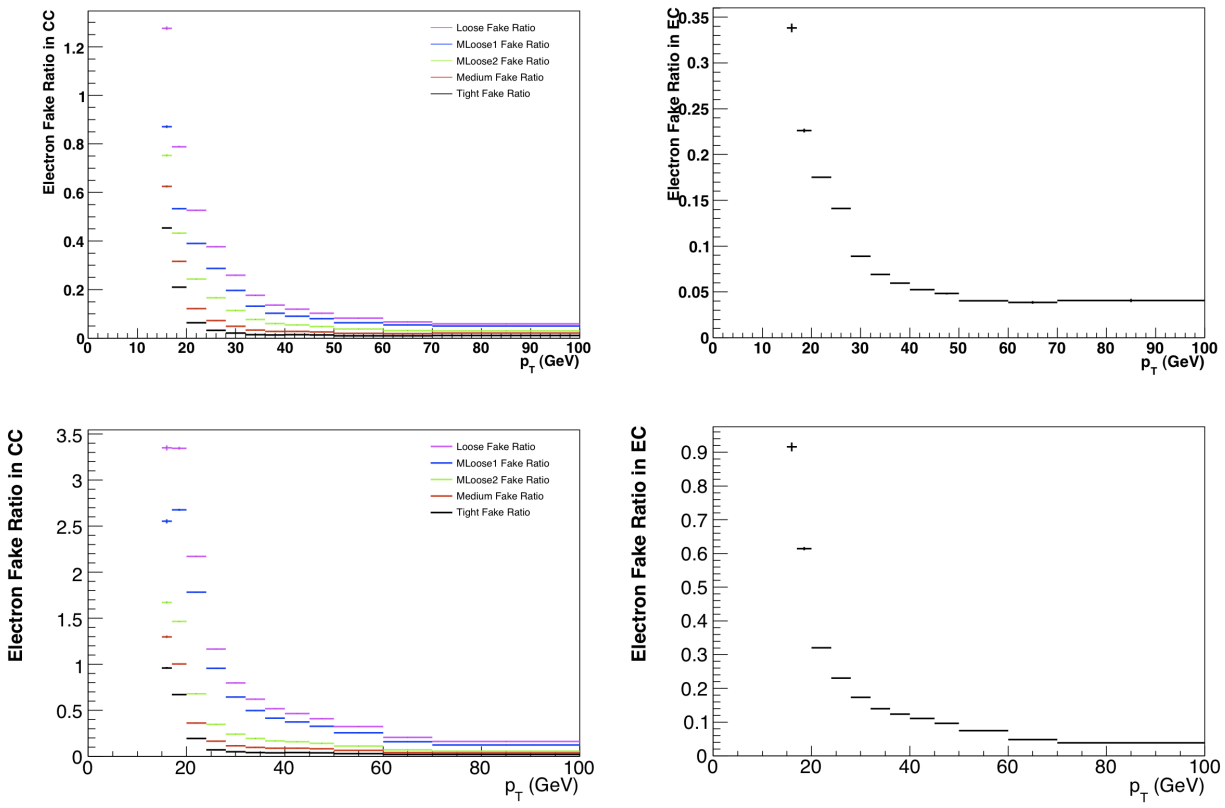

Figure 5.5: *The electron misidentification ratios vs. p_T for different identification criteria in CC (left) and for "Tight" electron misidentification ratio in EC (right) with trigger requirement. The first two plots correspond to Run IIa data and the next two plots correspond to Run IIb data.*

quality and isolation requirements are shown in Fig. 5.6 for Run IIa and Run IIb.

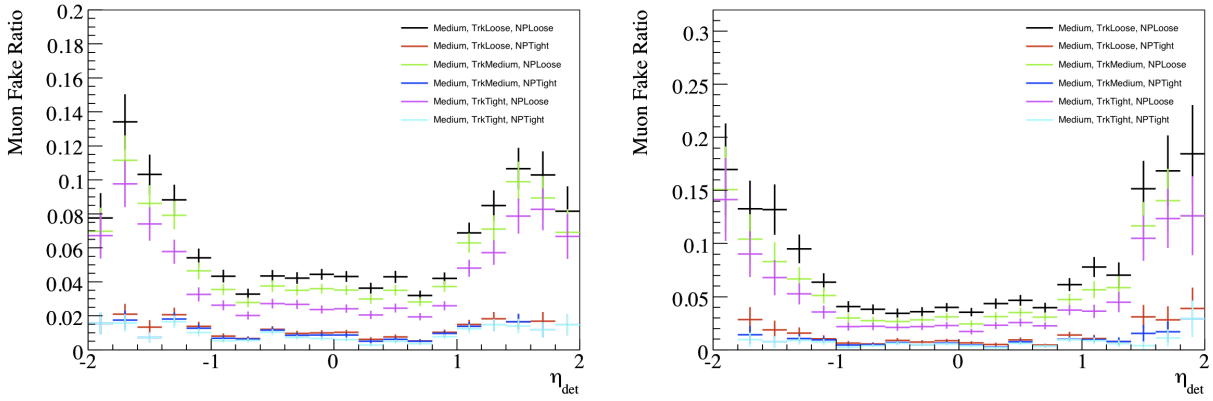

Figure 5.6: *The "Medium" quality muon misidentification ratios vs. η_{det} for the Run IIa (left) and Run IIb (right) datasets.*

Systematic Effects on $V + jets$ Background

Both electron and muon misidentification ratios can be overestimated if the skims have a sufficient number of $W \to \ell\nu$ events. Although the contamination from these processes is highly suppressed by the $\not\!\!E_T < 10$ GeV requirement, the $\not\!\!E_T$ threshold is loosened to 20 GeV and the misidentification ratios are recalculated to estimate the systematic effect. The newly obtained ratios are found to agree with those obtained from the original $\not\!\!E_T$ threshold within statistical uncertainties. To describe the effect of the small discrepancy in ratios, the $V+jets$ background is estimated using new ratios (*i.e.* the ratios with $\not\!\!E_T < 20$ GeV requirement) and a deviation from the original estimation is assigned as a systematic uncertainty on estimated $V + jets$ background. The misidentification ratios are also recalculated with the original $\not\!\!E_T$ threshold and different ΔR separation to study a potential systematic effects due to the trigger jet fragmentation. Varying ΔR requirement by ± 0.2 yields almost no change in misidentification ratios, and thus, the jet fragmentation systematic uncertainty is assumed to be negligible.

Another source of significant systematic uncertainty on the $V + jets$ background esti-

mation is a statistics in the multijet sample that limits the precision of the measurement of the misidentification ratios.

5.4.2 $Z\gamma$ Background

The channels with $W \to e\nu$ decays can be mimicked by the $Z\gamma$ process when a photon is either wrongly matched to a charged track or converts and one of the conversion particles is selected as an electron from the W boson decay. This background is not expected to be large, and it is estimated from the $Z\gamma$ Monte Carlo simulation. However, a potentially incorrect DØ material description in the simulation can affect the misidentification rate and result in the wrong estimate of the $Z\gamma$ background.

To ensure reliable estimation of this background, a thorough study of probability of a photon to be identified as an electron candidate in the MC simulation and data is performed. The only virtually background-free source of photons in hadron collisions is the final state radiation $Z \to \ell\ell\gamma$ process, where a photon is emitted from one of the final state charged leptons. The requirement of the invariant mass of the final state leptons and the photon to be consistent with the Z boson mass eliminates the largest background to this process, the $Z + jets$ production with one of the jets misidentified as a photon.

For this study, the $Z \to ee\gamma$ events cannot be used, as it is impossible to unambiguously identify a converted photon and two electrons in the final state. Therefore, $Z \to \mu\mu\gamma$ production is used. We select events with two muon candidates and one electromagnetic object using "2MUhighpt" DØ data sample. The "three-body" invariant mass distribution, shown in Fig. 5.7 exhibits a peak at the nominal Z boson mass, consistent with the final state $Z \to \mu\mu\gamma$ production.

Then, a probability that a photon in the $Z \to \mu\mu\gamma$ data sample will be identified as an electron candidate is calculated as a function of p_T. This probability measured in data agrees well with that obtained from the MC simulation of $Z \to \mu\mu\gamma$ initial state radiation process with the full simulation of the DØ detector using GEANT (see Fig. 5.8). The misidentification

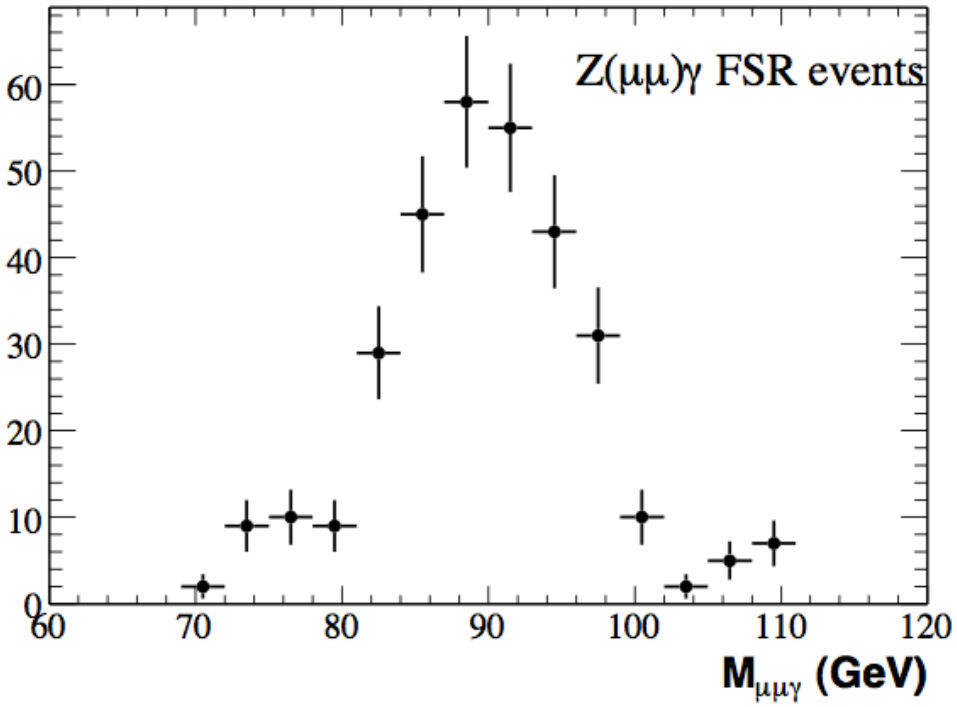

Figure 5.7: *Three-body mass of $Z(\mu\mu\gamma)$ FSR events from Run II data.*

rates for different electron selection criteria are shown in Fig. 5.9.

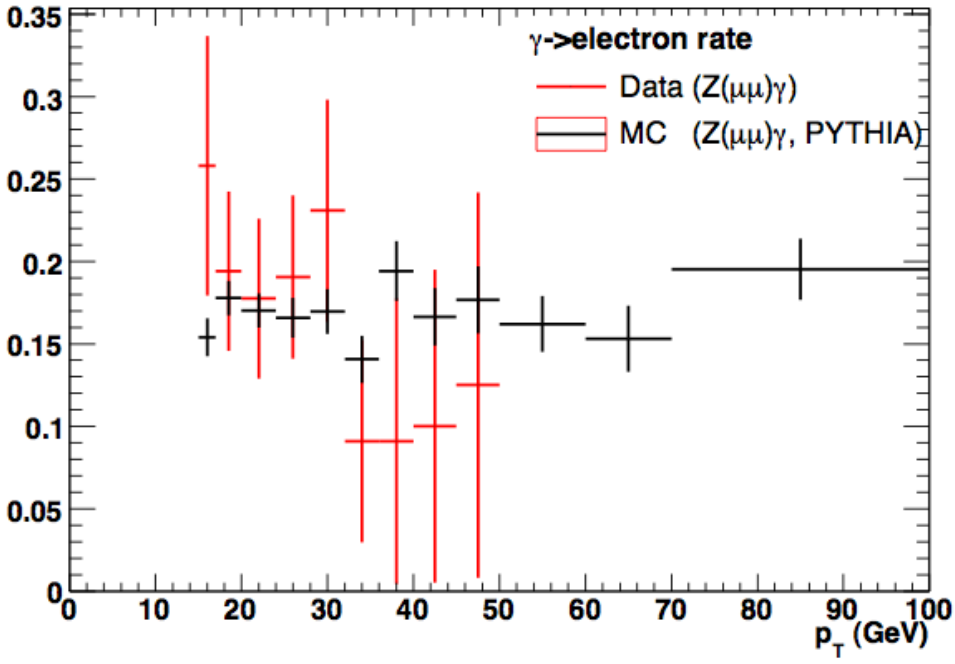

Figure 5.8: *The rate at which a photon can be reconstructed as an electron as a function of p_T from data (in red) and $Z\gamma$ Monte Carlo (in black).*

To estimate the $Z\gamma$ contribution, the $f_{\gamma\to e}(p_T)$ is folded with the photon p_T distribution in the $Z\gamma$ NLO Baur[45] Monte Carlo simulation for CC and EC regions separately as follows:

$$N_{Z\gamma} = \sigma_{\ell\ell\gamma} \times \mathcal{L}_{data} \times Acc \times \epsilon_{final\ state} \times f_{\gamma\to e}(p_T). \tag{5.2}$$

Here, the NLO cross section $\sigma_{\ell\ell\gamma}$, corresponding to the generator level cuts $p_T^{\gamma} > 15$ GeV, $M(\ell\ell) > 20$ GeV, $\Delta R(l_{1,2}, \gamma) > 0.4$, is 2.90 $\pm$ 0.2 pb, $\mathcal{L}_{data}$ is the integrated luminosity in data, and $Acc \times \epsilon_{final\ state}$ is the acceptance times efficiency of the selection criteria measured for the $Z\gamma$ process. As the Baur generator is a 4-vector particle generator, a fast parameterized Monte Carlo simulation of the DØ detector (PMCS)[46] is used to simulate the acceptance of the DØ detector, while the muon and electron identification efficiencies are obtained in data.

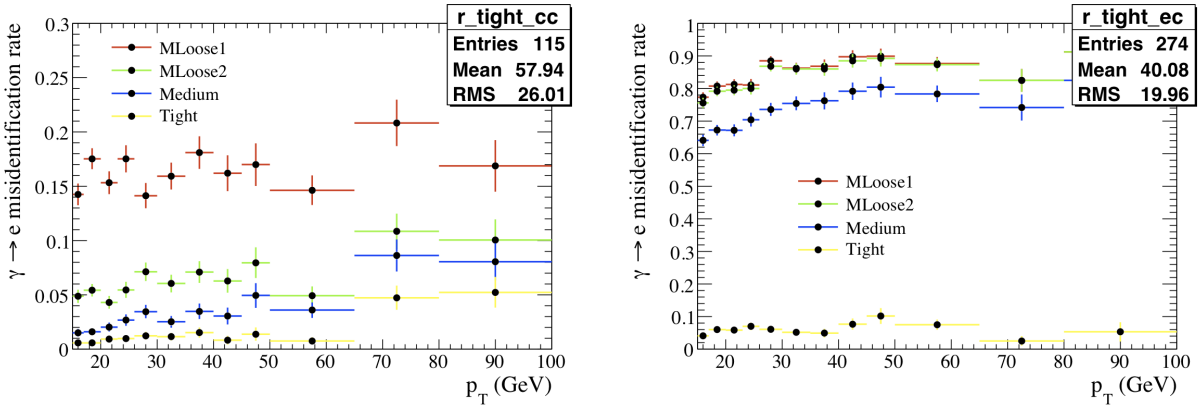

Figure 5.9: *The rate at which a photon is misidentified as an electron as a function of p_T for different electron definitions in the CC (left) and in the EC (right).*

Systematic Effects on $Z\gamma$ Background

The signal selection requirement that introduces the largest systematic uncertainty on the $Z\gamma$ contribution is the requirement of the $\not\!\!E_T$ in the event. As the $Z\gamma$ final state does not have true missing transverse energy, the efficiency of the $\not\!\!E_T$ requirement depends very strongly on how well the simulation describes the $\not\!\!E_T$ resolution in MC and also how well the simulation describes the composition of final state particles in the inclusive $Z\gamma$ production. To estimate these effects, the efficiency of the $\not\!\!E_T$ requirement in data and $Z\gamma$ PYTHIA MC simulation is compared after applying the same selection criteria. The distribution of $\not\!\!E_T$ in data and PYTHIA samples for three relevant final states are given in Fig. 7.6. Obtained difference in $\not\!\!E_T$ efficiency is taken as a systematic uncertainty on the estimated $Z\gamma$ background.

5.5 Results

5.5.1 Systematic uncertainties

Several sources of systematic uncertainty are considered in this analysis. Systematic uncertainty assigned to the lepton identification efficiency is 5%, 4%, and 6% for electron,

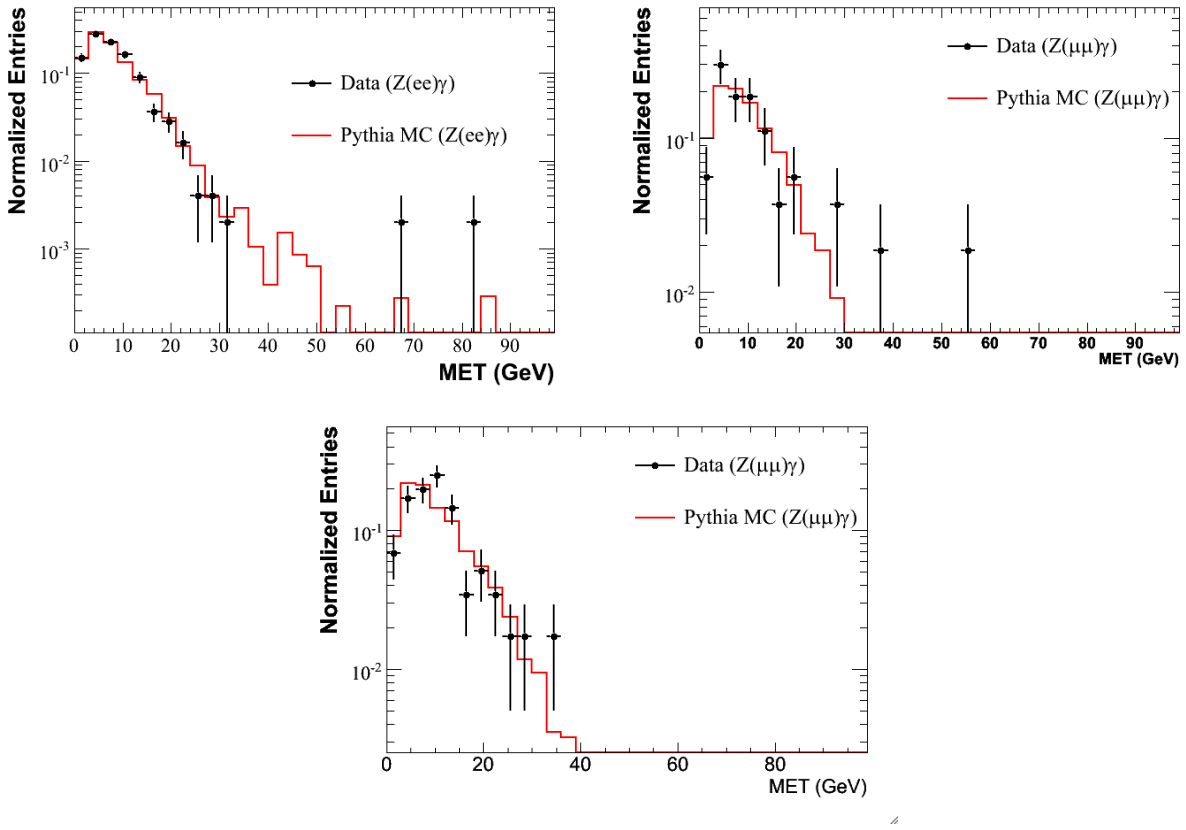

Figure 5.10: *$\not\!\!E_T$ distribution obtained from data (black histogram), $Z\gamma$* PYTHIA *Monte Carlo simulation (red histogram) for $Z \to e^+e^-\gamma$ (top left), $Z \to \mu^+\mu^-\gamma$ (top right), and $Z \to e^+e^-\gamma$ (bottom) with one electron from the Z boson in the ICR.*

Source	eee	$ee\mu$
ZZ	$0.29 \pm 0.04 \pm 0.05$	$0.99 \pm 0.07 \pm 0.17$
$V + jets$	$0.41 \pm 0.11 \pm 0.08$	$0.21 \pm 0.05 \pm 0.06$
$Z\gamma$	$0.18 \pm 0.01 \pm 0.07$	< 0.001
$t\bar{t}$	$0.03 \pm 0.01 \pm 0.01$	$0.02 \pm 0.01 \pm 0.003$
Total bkg.	$0.03 \pm 0.01 \pm 0.01$	$0.02 \pm 0.01 \pm 0.003$
WZ signal	$4.4 \pm 0.1 \pm 0.8$	$5.0 \pm 0.1 \pm 0.7$
Observed	8	8

Table 5.8: *Number of observed data events, expected number of signal events, and expected number of background events for signatures with $Z \to ee$ decays with statistical and systematic uncertainties.*

muon, and ICR electron, respectively. Systematic uncertainty assigned to the PDF choice is 5% and uncertainty due to modeling of the WZ system is also 5%. In addition, 5% and 10% systematic uncertainties are assigned on the estimated $t\bar{t}$[47,48] and ZZ[49] backgrounds, respectively, due to the uncertainty in their theoretical cross sections. The major sources of systematic uncertainty on the estimated $V +$ jets contribution are the $\not\!\!E_T$ requirement and the statistics used in the measurement of the lepton misidentification ratios. Those effects are estimated independently for each topology (see Section 5.4.1) and found to be between 20-30%. The systematic uncertainty on the $Z\gamma$ background is estimated (see Section 5.4.2) to be 40%, 58%, and 30% for eee, $\mu\mu e$, and $ee_{ICR}e$ channels, respectively. Systematic uncertainty due to the integrated luminosity is 6.1%[50].

5.5.2 Event yields

The event selection yields 34 WZ candidate events with an estimated 23.3 ± 0.2 signal, and 6.0 ± 0.4 total background events (uncertainties are statistical only). Observed candidates, signal and background events for each signature are summarized in Tables 5.8, 5.9, and 5.10.

The invariant mass and transverse mass for selected Z and W candidates in data, with expected signal and backgrounds overlaid, are given in Figs. 5.11 and 5.12, respectively.

Event displays of some of the observed candidates are shown in Figs. 5.13-5.15.

Source	$\mu\mu e$	$\mu\mu\mu$
ZZ	$0.40 \pm 0.04 \pm 0.06$	$1.26 \pm 0.07 \pm 0.22$
$V + jets$	$0.03 \pm 0.01 \pm 0.01$	$0.17 \pm 0.04 \pm 0.03$
$Z\gamma$	$0.66 \pm 0.02 \pm 0.34$	< 0.001
$t\bar{t}$	$0.04 \pm 0.01 \pm 0.01$	$0.03 \pm 0.01 \pm 0.01$
Total bkg.	$1.13 \pm 0.05 \pm 0.35$	$1.46 \pm 0.08 \pm 0.23$
WZ signal	$4.7 \pm 0.1 \pm 0.6$	$5.8 \pm 0.1 \pm 0.8$
Observed	9	5

Table 5.9: *Number of observed data events, expected number of signal events, and expected number of background events for signatures with $Z \to \mu\mu$ decays with statistical and systematic uncertainties.*

Source	$ee_{ICR}e$	$ee_{ICR}\mu$
ZZ	$0.10 \pm 0.02 \pm 0.02$	$0.49 \pm 0.05 \pm 0.08$
$V + jets$	$0.22 \pm 0.07 \pm 0.08$	$0.35 \pm 0.16 \pm 0.16$
$Z\gamma$	$0.10 \pm 0.01 \pm 0.03$	< 0.001
$t\bar{t}$	$0.001 \pm 0.001 \pm < 0.001$	$0.03 \pm 0.01 \pm 0.004$
Total bkg.	$0.42 \pm 0.08 \pm 0.09$	$0.88 \pm 0.17 \pm 0.18$
WZ signal	$1.5 \pm 0.1 \pm 0.2$	$1.9 \pm 0.1 \pm 0.2$
Observed	1	3

Table 5.10: *Number of observed data events, expected number of signal events, and expected number of background events for signatures with $Z \to ee_{ICR}$ decays with statistical and systematic uncertainties.*

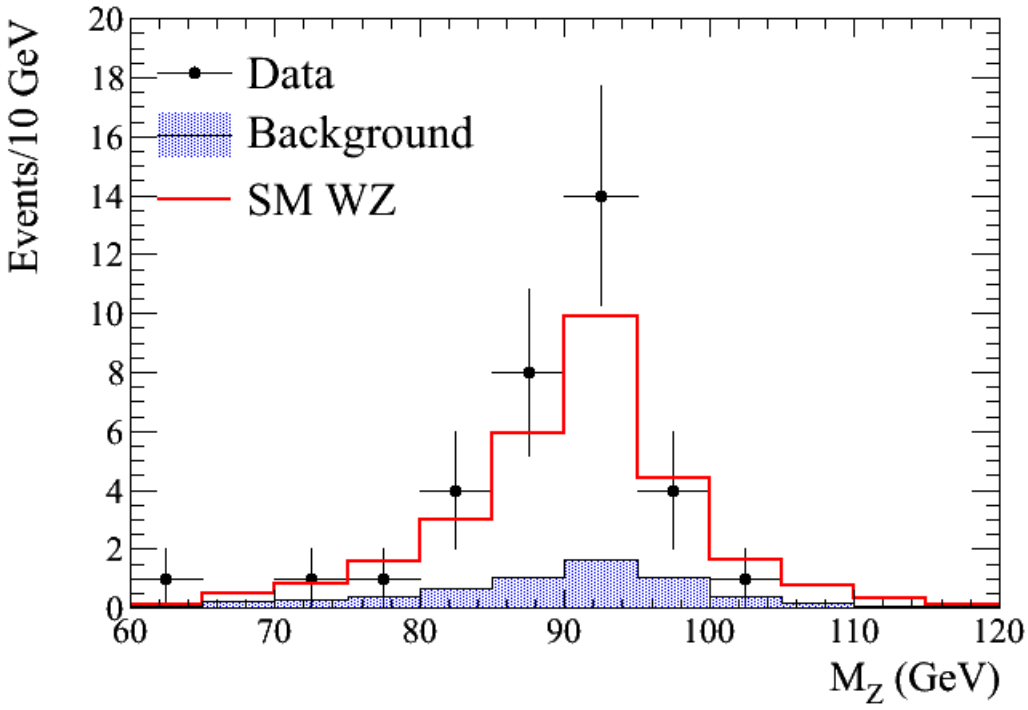

Figure 5.11: *Invariant mass of selected Z candidates in data (black points), with WZ signal (red histogram) and total background (blue histogram) overlaid.*

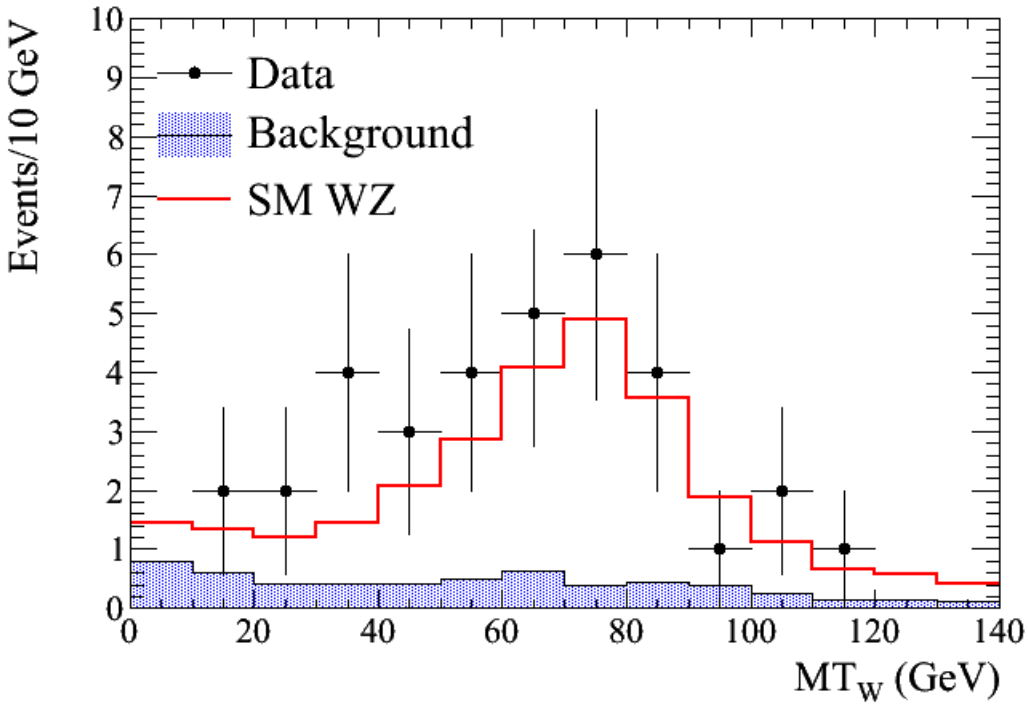

Figure 5.12: *Transverse mass of selected W candidates in data (black points), with WZ signal (red histogram) and total background (blue histogram) overlaid.*

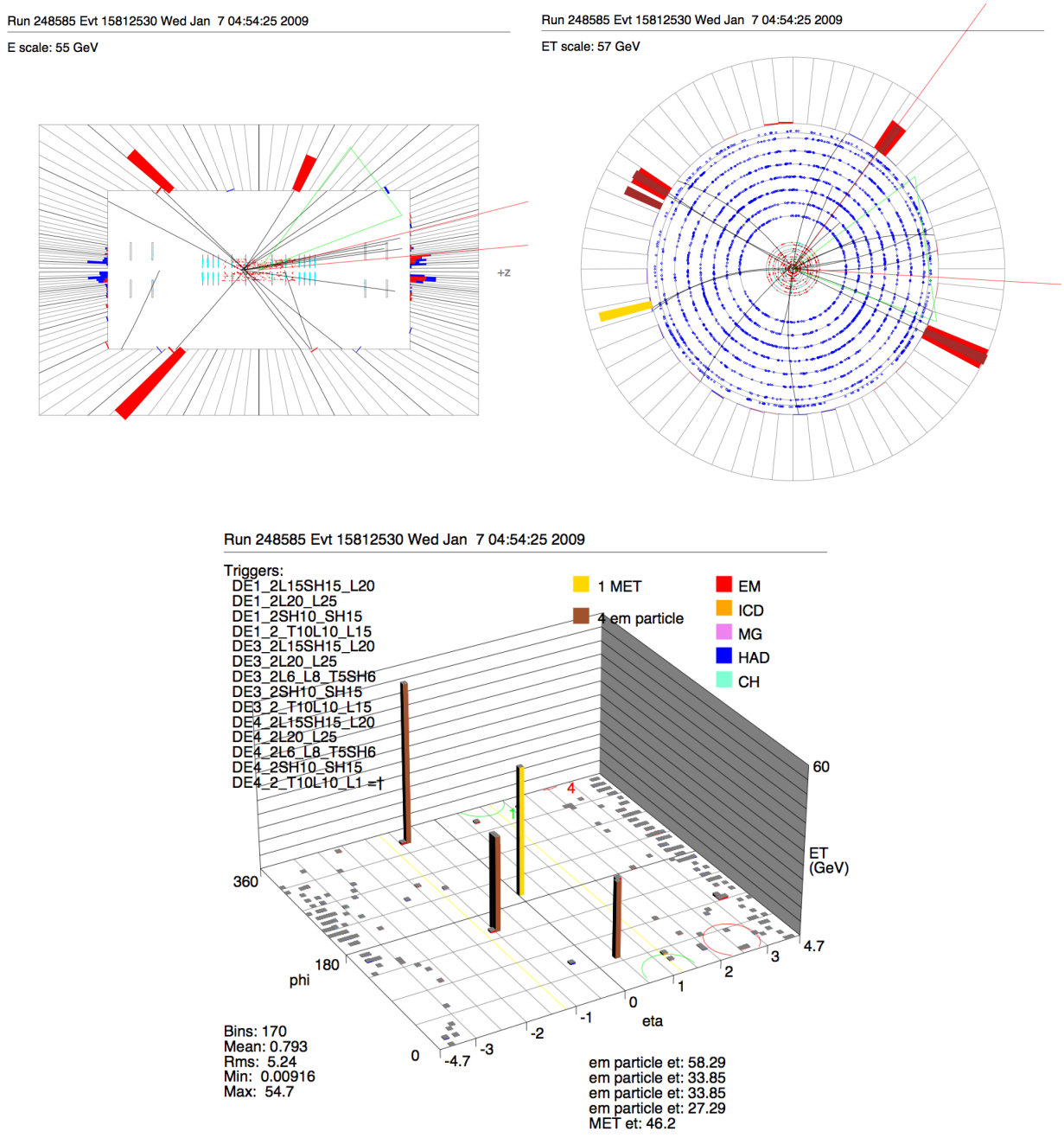

Figure 5.13: *Event display of a $WZ \rightarrow eee\nu$ candidate event is given in the $y-z$ plane (top left), the $x-y$ plane (top right), and 3D lego plot (bottom).*

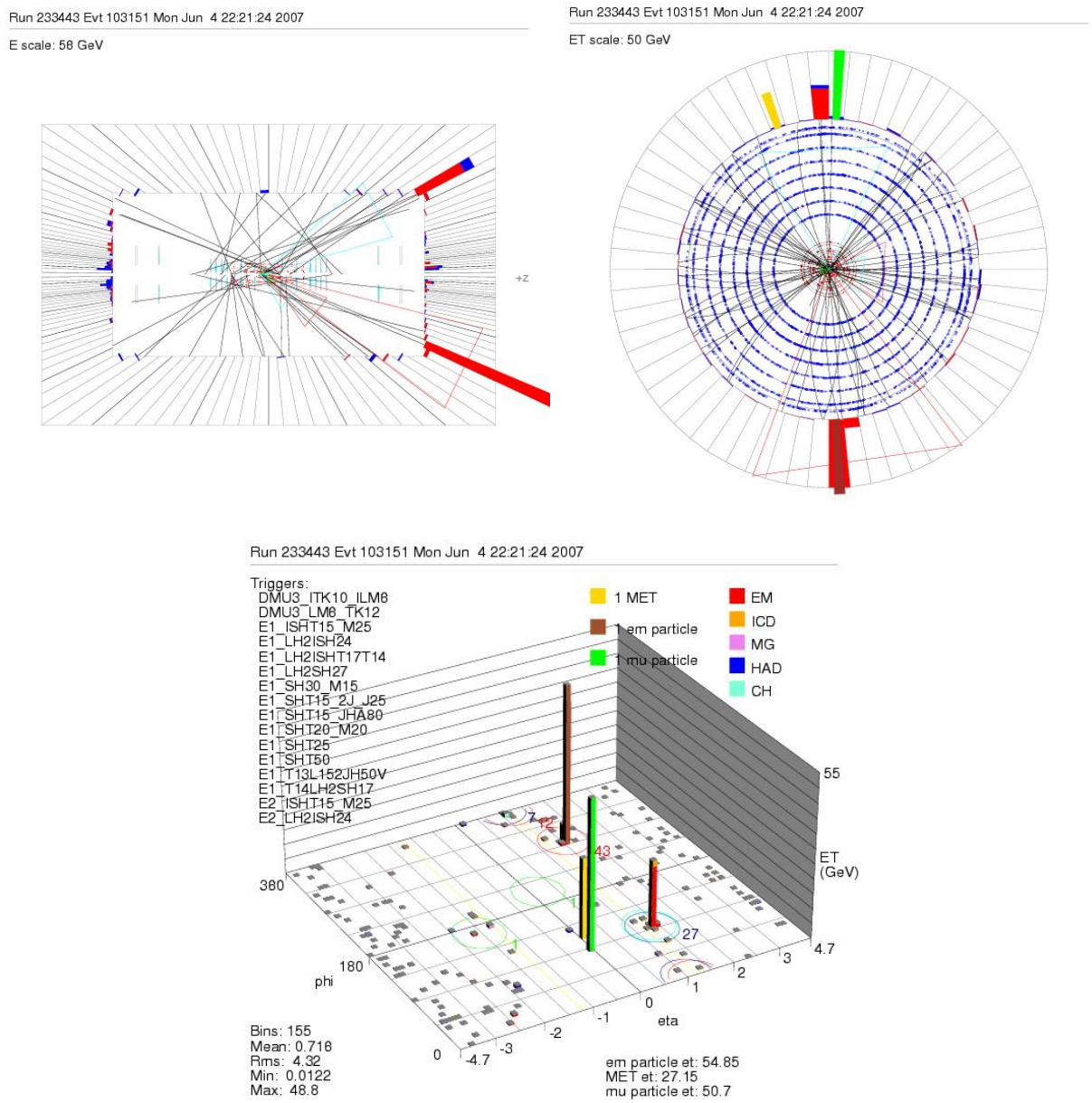

Figure 5.14: *Event display of a $WZ \rightarrow ee_{ICR}\mu\nu$ candidate event is given in the $y-z$ plane (top left), the $x-y$ plane (top right), and 3D lego plot (bottom).*

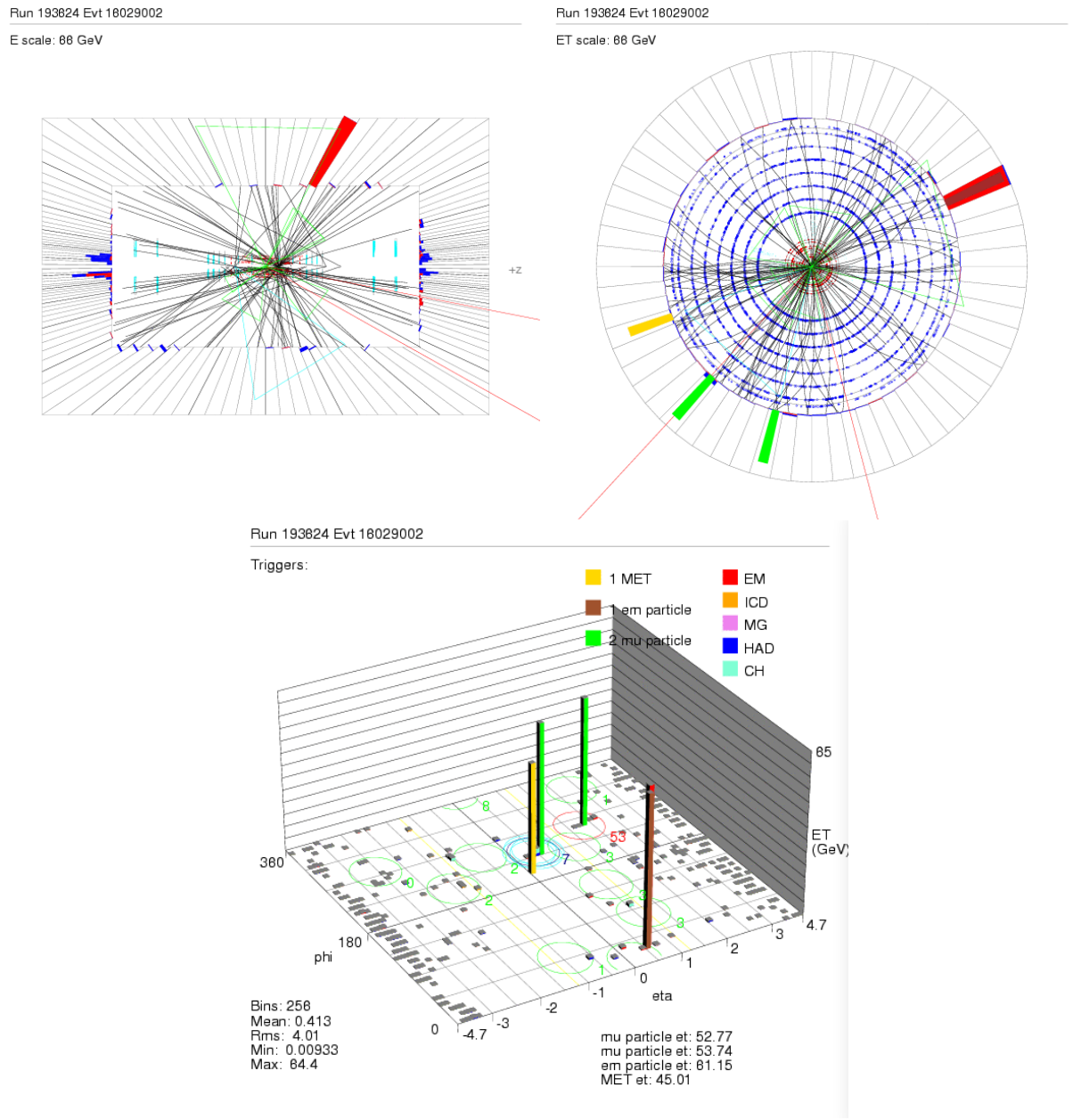

Figure 5.15: *Event display of a $WZ \to \mu\mu e\nu$ candidate event is given in the $y-z$ plane (top left), the $x-y$ plane (top right), and 3D lego plot (bottom).*

5.5.3 Cross section measurement

The cross section of WZ production times $Br(WZ \to \ell\nu\ell\ell)$ is given by the following formula

$$\sigma \times Br(WZ \to \ell\nu\ell\ell) = \frac{N_{obs} - N_{bkg}}{Acc \times \epsilon \times \mathcal{L}}, \tag{5.3}$$

where N_{obs} and N_{bkg} are the number of observed candidates and the number of estimated background events and Acc, ϵ, and $\mathcal{L}$ are acceptance, efficiency of selection criteria, and integrated luminosity, respectively. However, N_{obs} in each final states is small enough that the usual approximation of Poisson statistics to Gaussian statistics does not apply. Therefore, to calculate the uncertainties on the individual cross section a log-likelihood method[51] with Poisson statistics is used.

From Poisson statistics, given a number of measured events in the i^{th} final state, n_i, the likelihood that a predicted number of events, λ_i, is consistent with n_i is

$$L_i = \text{Poisson}(n_i, \lambda_i) = \frac{\lambda_i^{n_i} e^{-\lambda_i}}{n_i!}. \tag{5.4}$$

Here, λ_i is equal to the total predicted signal plus background events as follows

$$\lambda_i = \sigma'_{WZ} \times \mathcal{L} \times \alpha_i + \lambda_{bkgi}, \tag{5.5}$$

where σ'_{WZ} is the cross section which is being varied to minimize the negative log-likelihood, $\mathcal{L}$ is the total luminosity, α_i is the total acceptance times efficiency for a given final state, and λ_{bkgi} is the total expected background in that final state. The total likelihood is determined by

$$L = \prod L_i \tag{5.6}$$

The log-likelihood takes into account the systematic uncertainties by performing a multidimensional integration over all systematic uncertainties using Gaussian statistics. The integral is numerically calculated in the range of $(-3\sigma_j, 3\sigma_j)$, where σ_j corresponds to one

standard deviation (s.d.) in λ due to the j^{th} systematic uncertainty. The negative log-likelihood for a single final state is:

$$-lnL_i = -ln \int \cdots \int \text{Gaus}(x_1, \sigma_1) \cdots \text{Gaus}(x_{N_{syst}}, \sigma_{N_{syst}}) \text{Poisson}(n_i, \lambda_i + \sum x_j frac \partial \lambda_i \partial x_j) dx_1 \cdots dx_{N_{syst}} \tag{5.7}$$

where $\text{Gaus}(x, \sigma) = \frac{1}{\sqrt{2\pi}\sigma} e^{-\frac{x^2}{2\sigma^2}}$ and N_{syst} is the number of independent systematic uncertainties.

The cross section values measured from individual channels, with Poisson uncertainties, are summarized in Table 5.11.

Channel	Cross section (pb)
eee	$5.18 + 2.61 - 1.92(stat + syst) \pm 0.34(lumi)$
$ee\mu$	$4.41 + 2.22 - 1.68(stat + syst) \pm 0.32(lumi)$
$e\mu\mu$	$5.48 + 2.48 - 1.91(stat + syst) \pm 0.36(lumi)$
$\mu\mu\mu$	$1.95 + 1.51 - 1.08(stat + syst) \pm 0.14(lumi)$
$ee_{ICR}e$	$1.32 + 3.17 - 1.32(stat + syst) \pm 0.09(lumi)$
$ee_{ICR}\mu$	$3.80 + 3.78 - 2.54(stat + syst) \pm 0.29(lumi)$

Table 5.11: *Cross section measured from individual channels with statistical, systematic and luminosity uncertainties.*

Full correlation between systematic uncertainties in individual decay signatures is taken into account by integrating over them at the same time. The final log-likelihood is determined by

$$-lnL = -ln \int \cdots \int \text{Gaus}(x_1, \sigma_1) \cdots \text{Gaus}(x_{N_{syst}}, \sigma_{N_{syst}}) \prod_i \text{Poisson}(n_i, \lambda_i + \sum x_j \frac{\partial \lambda_i}{\partial x_j}) dx_1 \cdots dx_{N_{syst}} \tag{5.8}$$

The measured value of the cross section is taken from the minimum of the negative log-likelihood. The negative log-likelihood *vs.* the combined cross section is shown in Fig. 5.16. The uncertainty on this value is estimated by moving up 0.5 units in negative log-likelihood,

yielding an asymmetric error. The resultant combined cross section is $3.90^{+1.01}_{-0.85}(stat+syst)\pm 0.31(lumi)$ pb.

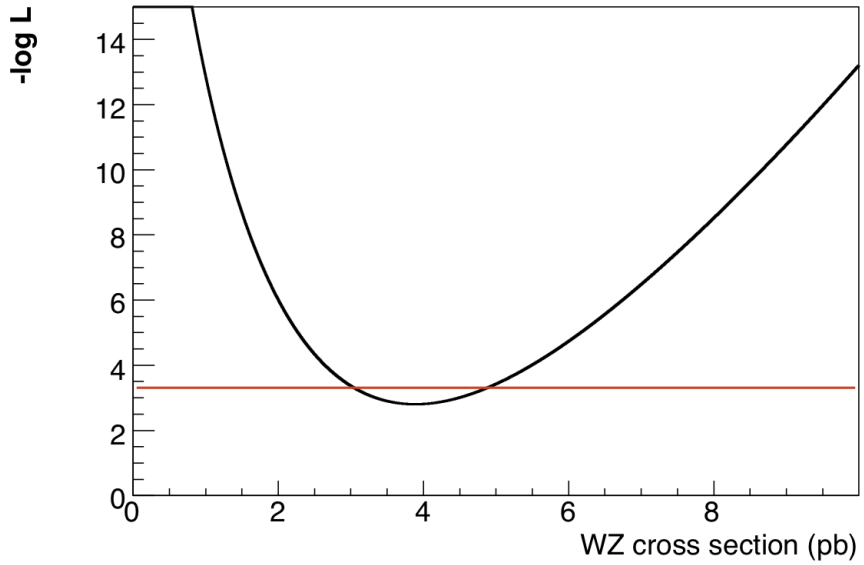

Figure 5.16: *Negative log-likelihood vs. the value of the combined cross section. Intersections of the red line and the likelihood curve indicate a one sigma uncertainty interval.*

Chapter 6

Limits on Anomalous WWZ Triple Gauge Couplings

The presence of WWZ anomalous triple gauge couplings (aTGC) would lead to both an increase in the cross section and an enhancement of the p_T spectra of the W and Z bosons. The Z boson p_T distribution is used as an observable to probe the WWZ couplings in this analysis. The Z boson p_T spectra from data, the SM WZ signal and background processes, and two anomalous coupling predictions are shown in Fig. 6.1. The difference is most appreciable in the last bin, which includes all of the overflows. For example, the event displays of couple of the observed candidates with the high transverse momentum Z boson are shown in Figs. 6.2 and 6.3. Since data is in agreement with the standard model prediction, limits on the anomalous coupling parameters are set.

The misassignment of the WZ decay products, described in Section 5.3.2, might affect the p_T spectrum of the Z boson candidate, used in limit setting procedure. Using the signal MC sample and following the assignment procedure described above, a comparison of the Z boson p_T spectrum for correctly and wrongly assigned decay products is performed, see Fig. 6.4. As seen, the distributions agree well for high p_T region which has more sensitivity to anomalous production of the WZ. For low p_T region there is some discrepancy. However, knowing that the inefficiency of assignment is only 6%, 11%, and 15% for eee, $\mu\mu\mu$, and $ee_{ICR}e$ channels, respectively, the effect on the limits due to the misassignment is only a few

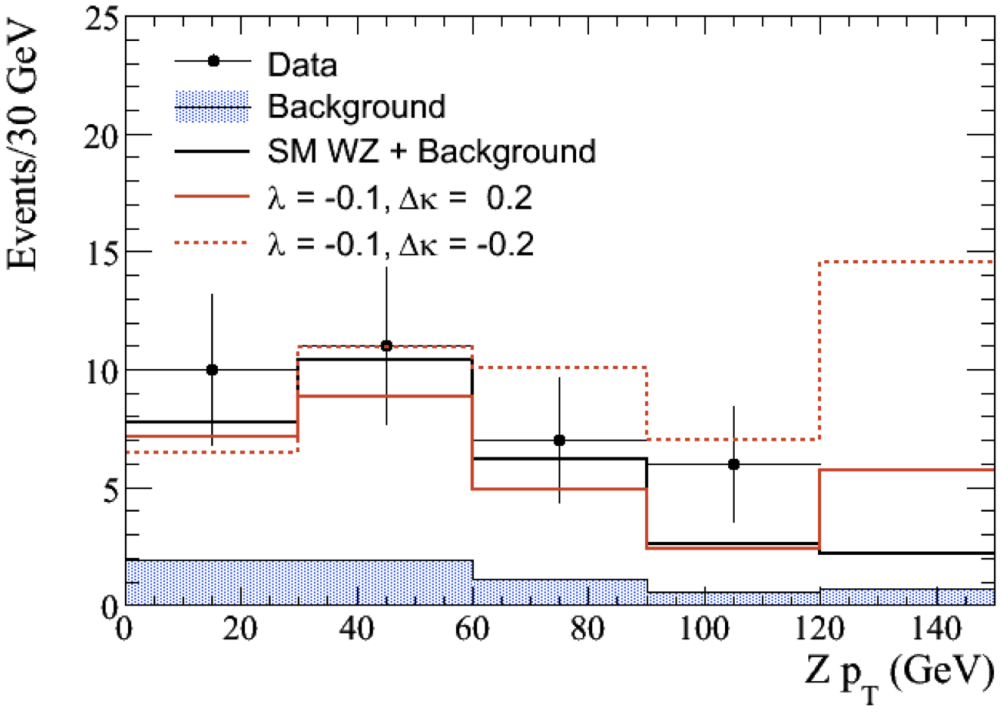

Figure 6.1: *The Z boson p_T spectrum from data (points), total background (solid grey), the SM WZ single plus total background (black), and two anomalous coupling models (red). The last bin includes overflows.*

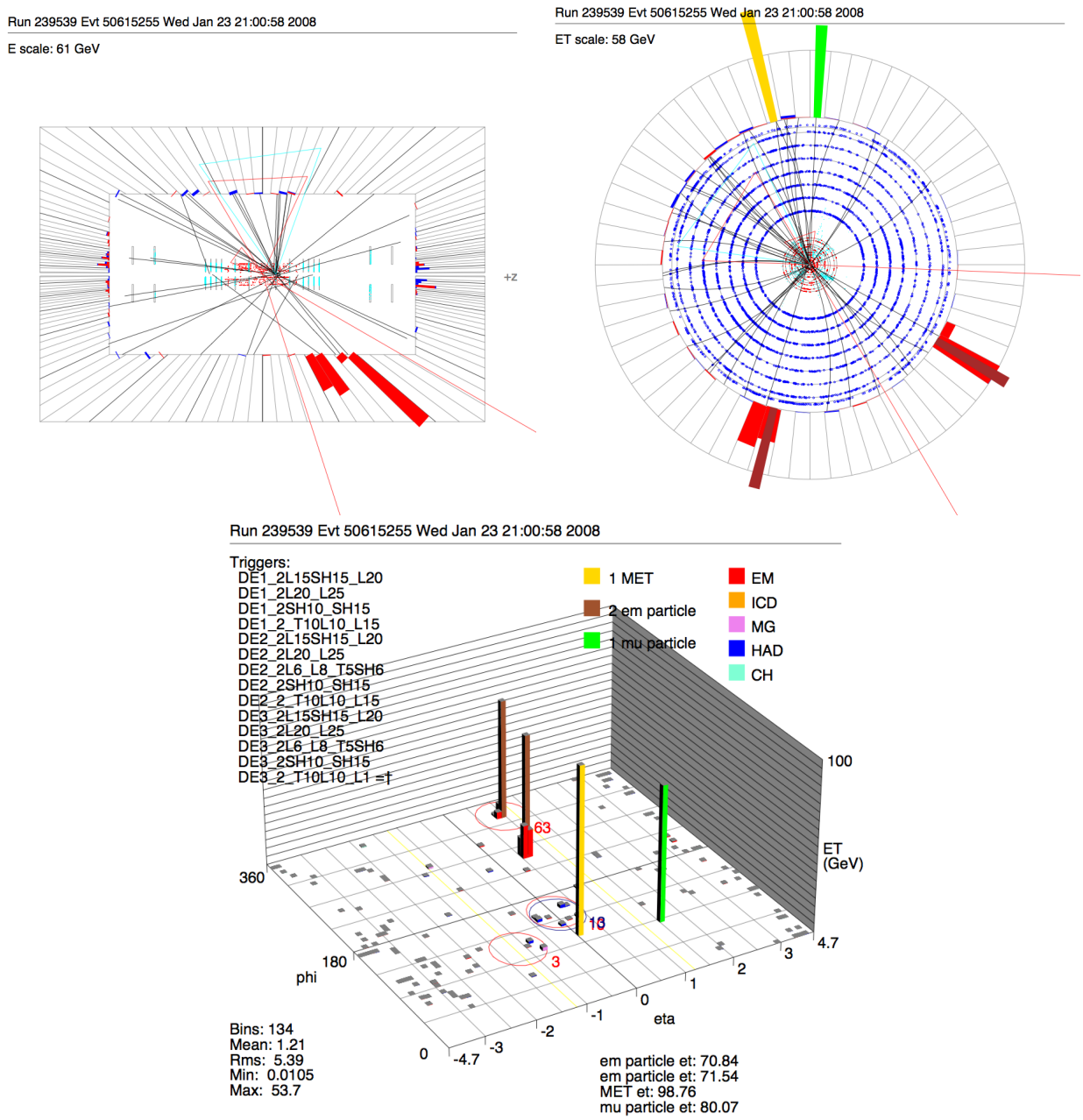

Figure 6.2: *Event display of a $WZ \rightarrow ee\mu\nu$ candidate event is given in the $y-z$ plane (top left), the $x-y$ plane (top right), and 3D lego plot (bottom). The p_T of the Z boson in this event is measured to be 109 GeV.*

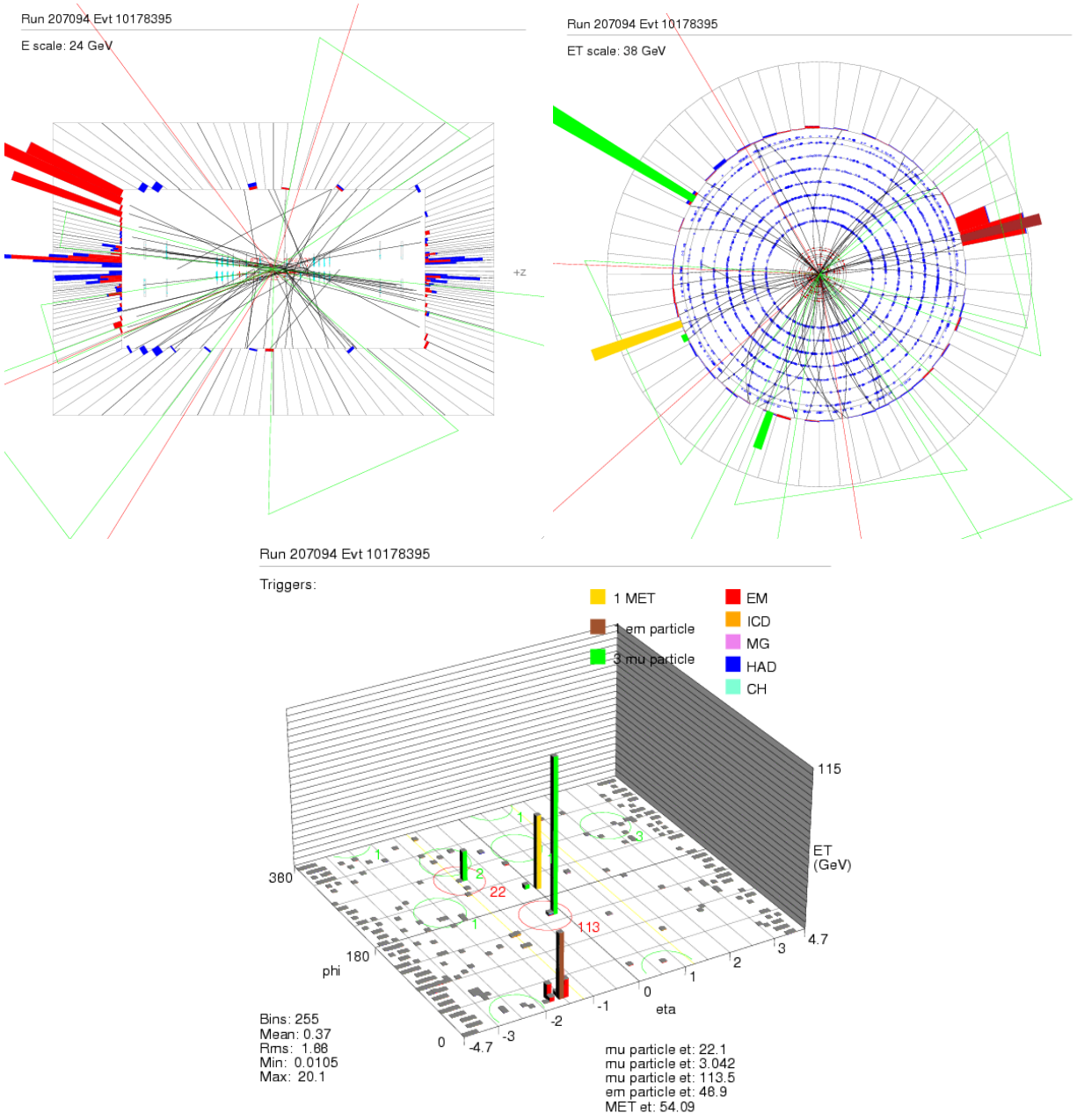

Figure 6.3: *Event display of a $WZ \to \mu\mu e\nu$ candidate event is given in the $y-z$ plane (top left), the $x-y$ plane (top right), and 3D lego plot (bottom). The p_T of the Z boson in this event is measured to be 111 GeV.*

percent and can be neglected.

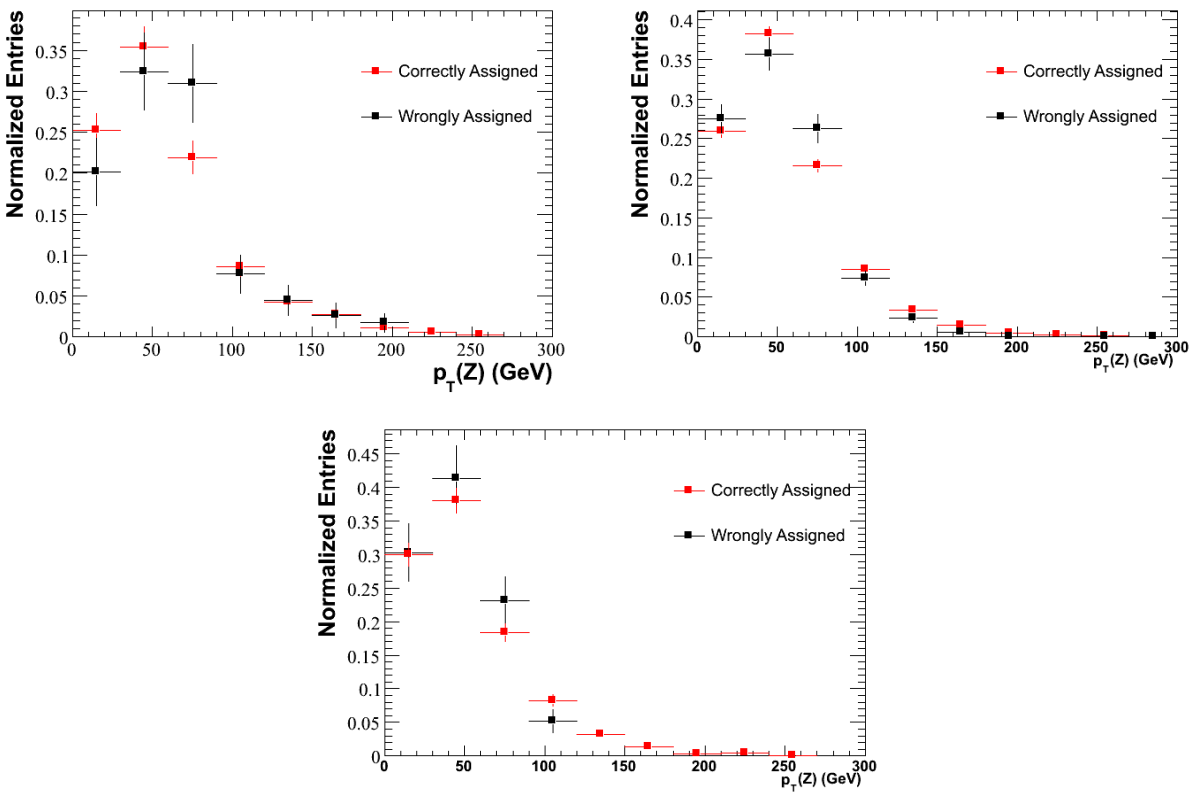

Figure 6.4: *The p_T distribution for the Z bosons with correctly (red) and wrongly (black) assigned decay products for eee (top left), $\mu\mu\mu$, (top right) and $ee_{ICR}e$ (bottom) signatures.*

In interpretation of the results on WWZ aTGC, three commonly known relations between the WWZ and $WW\gamma$ couplings are used. Similarly to WWZ (see Section 2.2), there are three C, P, and CP conserving couplings for $WW\gamma$ vertex[2,3], g_1^γ, κ_γ, and λ_γ. However, $g_1^\gamma = 1$ at all times due to electromagnetic gauge invariance. The WWZ and $WW\gamma$ coupling relations considered in this thesis are following:

- LEP parameterization[52]: $\Delta\kappa_Z = \Delta g_1^Z - \Delta\kappa_\gamma tan^2\theta_W$, $\lambda_Z = \lambda_\gamma$. As the WZ boson pair production is insensitive to the strength of the $WW\gamma$ couplings, we choose to fix λ_γ to zero, *i.e.* its standard model value.

- HISZ relation[53,54]: $\Delta\kappa_Z = \Delta\kappa_\gamma(1 - tan^2\theta_W)/2$, $\Delta g_1^Z = \Delta\kappa_\gamma/2cos^2\theta_W$, and $\lambda_Z = \lambda_\gamma$.

- Equal coupling relation: $\Delta\kappa_Z = \Delta\kappa_\gamma$, $\lambda_Z = \lambda_\gamma$, and $\Delta g_1^Z = \Delta g_1^\gamma = 0$.

A two-dimensional (2D) grid of anomalous coupling values is produced for each parametrization. For each point on the 2D grid, MCFM[41] generator is used to generate Monte Carlo events for non-SM WWZ production and to obtain the corresponding cross section values. These events are processed with PMCS to simulate the detector response for acceptance calculation, while trigger and object identification efficiencies are estimated using the officially produced SPC files. Then, the reconstructed Z p_T distribution from the WZ sample, produced with the full GEANT simulation of the DØ detector, is re-weighted to describe the shape of the anomalous Z p_T using the following formula:

$$\frac{dN}{dp_T}(aTGC, NLO) = \frac{dN}{dp_T}(pythia)\frac{\frac{dN}{dp_T}(mcfm, NLO, aTGC)}{\frac{dN}{dp_T}(mcfm, LO, SM)}. \quad (6.1)$$

The Z boson p_T distribution obtained from the NLO MCFM sample, simulated with PMCS, is similar to one obtained using PYTHIA WZ sample, processed with GEANT simulation, for both $Z \to ee$ and $Z \to \mu\mu$ decay signatures (see Fig. 6.5). However, any potential discrepancy due to both modeling the WZ system with MCFM or PYTHIA and using fast or full simulation of the DØ detector is still quantitatively estimated by comparing the $Acc \times \epsilon$ in these two samples. The comparison yields $\sim$ 12% difference. Therefore, a conservative 15% systematic uncertainty is assigned when setting limits on anomalous triple gauge couplings.

The distribution for each anomalous coupling point on 2D grid is further normalized using the obtained cross section, acceptance, and efficiency to correspond to the integrated luminosity in data.

The binned likelihood method is used to set limits on aTGC. It calculates the likelihood in each bin of the Z boson p_T distribution, shown in Fig. 6.1. The likelihood for the whole distribution is a product of likelihoods in individual bins.

The calculated likelihoods are shown in Figs. 6.6-6.8. In each case, Gaussian uncertainties are assumed for the background and resolution integration. The one-dimensional limits on

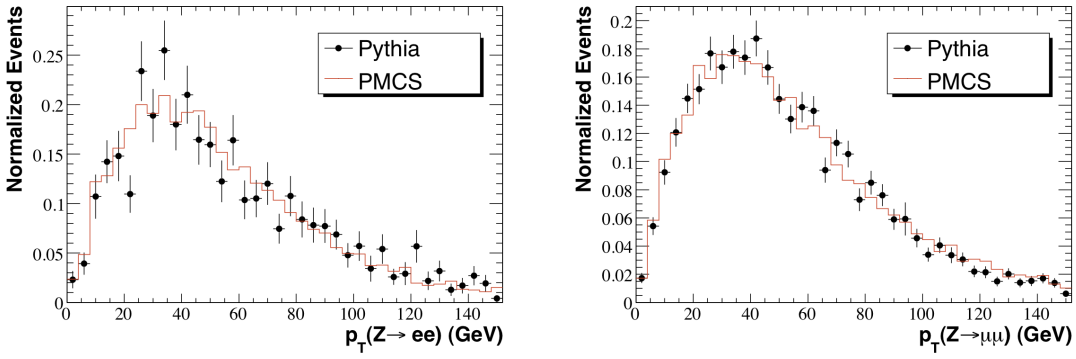

Figure 6.5: *Z boson p_T spectrum from the SM WZ production in* PYTHIA *(black points) and* MCFM+PMCS *(red histogram) for $Z \to ee$ (left) and $Z \to \mu\mu$ (right) decays.*

the couplings for three different parametrizations are summarized in Table 6.1. The two-dimensional anomalous coupling limits, shown in Figs. 6.9-6.11, correspond to a "*slice*" of the likelihood at the appropriate value for 95% C.L. in two dimensions, *i.e.*, $\Delta L = 2.99$.

Coupling Relation	95% C.L. Limit
LEP	$-0.08 < \lambda_Z < 0.10$ $-0.05 < \Delta\kappa_Z < 0.15$
HISZ	$-0.08 < \lambda_Z < 0.10$ $-0.06 < \Delta\kappa_Z < 0.17$
EQUAL	$-0.08 < \lambda_Z < 0.10$ $-0.28 < \Delta\kappa_Z < 0.76$

Table 6.1: *One dimensional 95% C.L. limits on anomalous coupling paramters for three different parametrizations.*

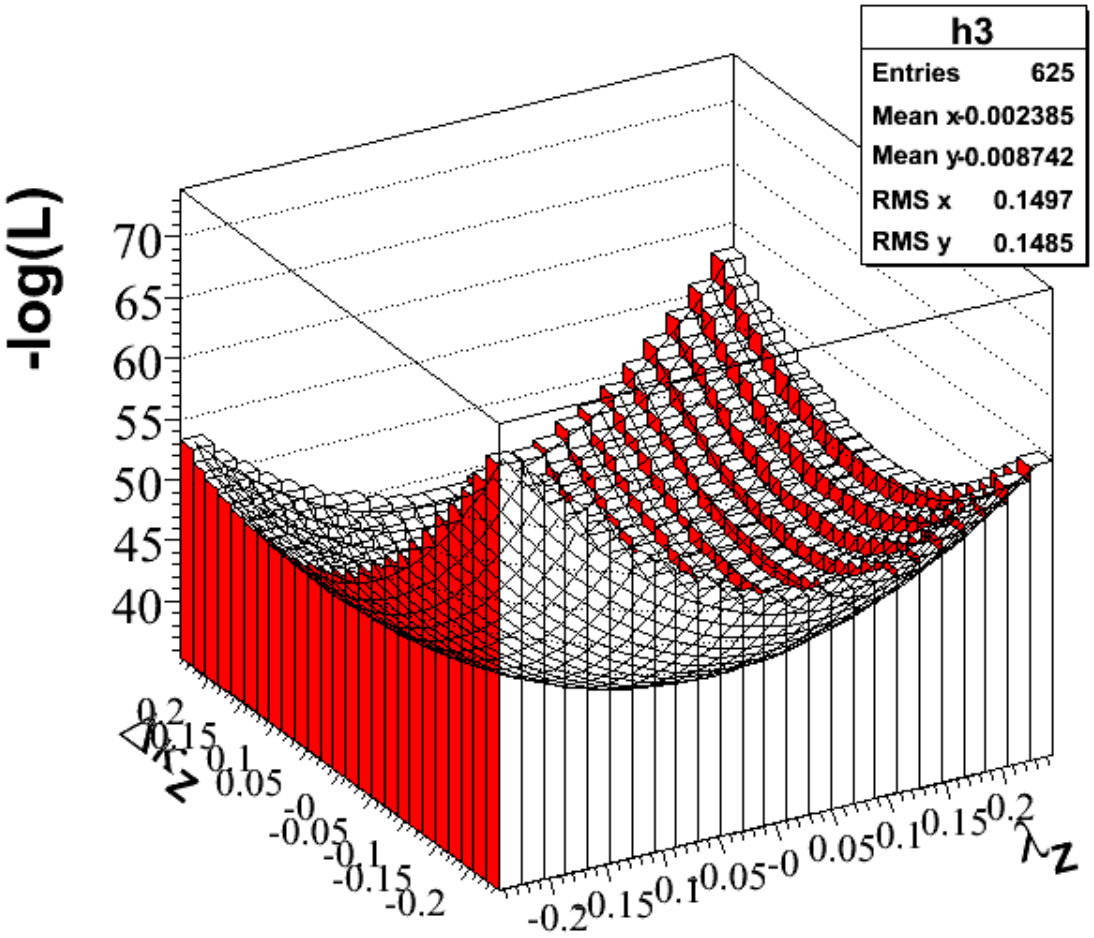

Figure 6.6: *Likelihood surface calculated for the LEP parametrization. The overlayed surface is the fit to the likelihood used to interpolate the one- and two-dimensional anomalous coupling limits.*

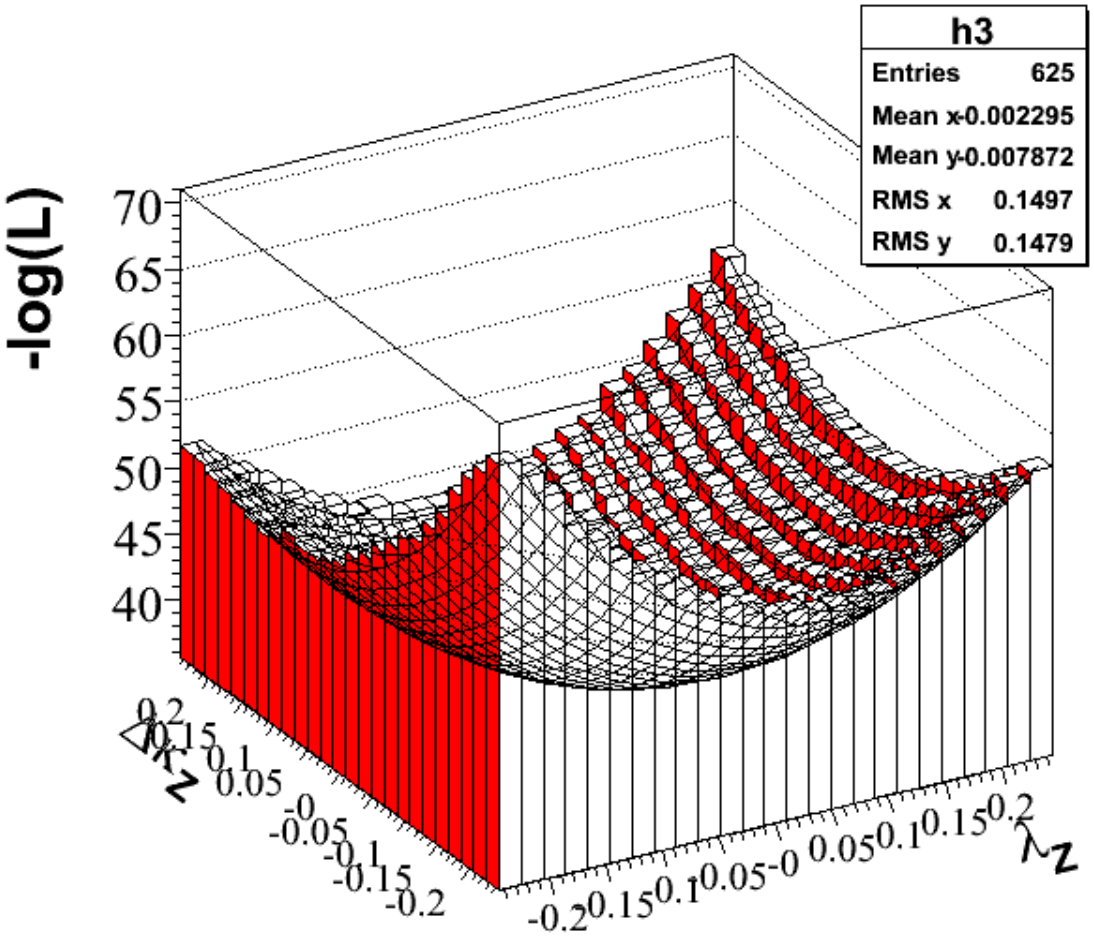

Figure 6.7: *Likelihood surface calculated for the HISZ parametrization. The overlayed surface is the fit to the likelihood used to interpolate the one- and two-dimensional anomalous coupling limits.*

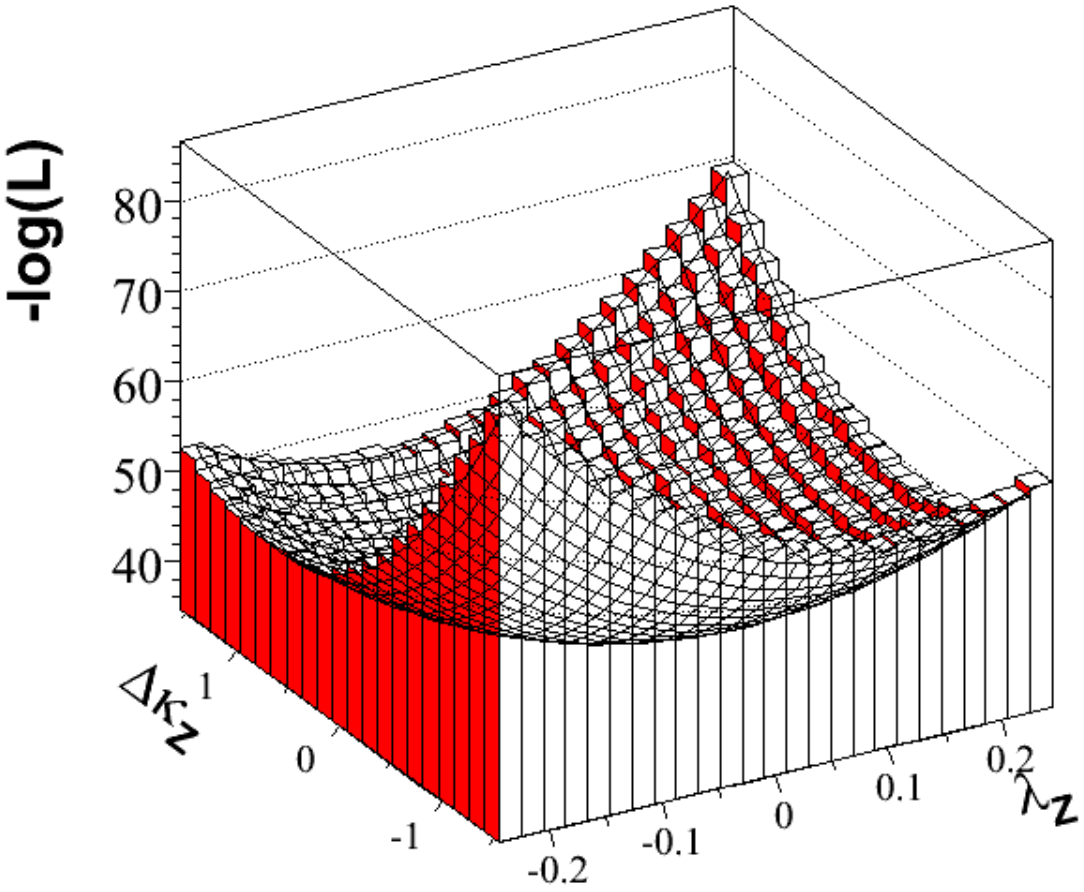

Figure 6.8: *Likelihood surface calculated for the EQUAL parametrization. The overlayed surface is the fit to the likelihood used to interpolate the one- and two-dimensional anomalous coupling limits.*

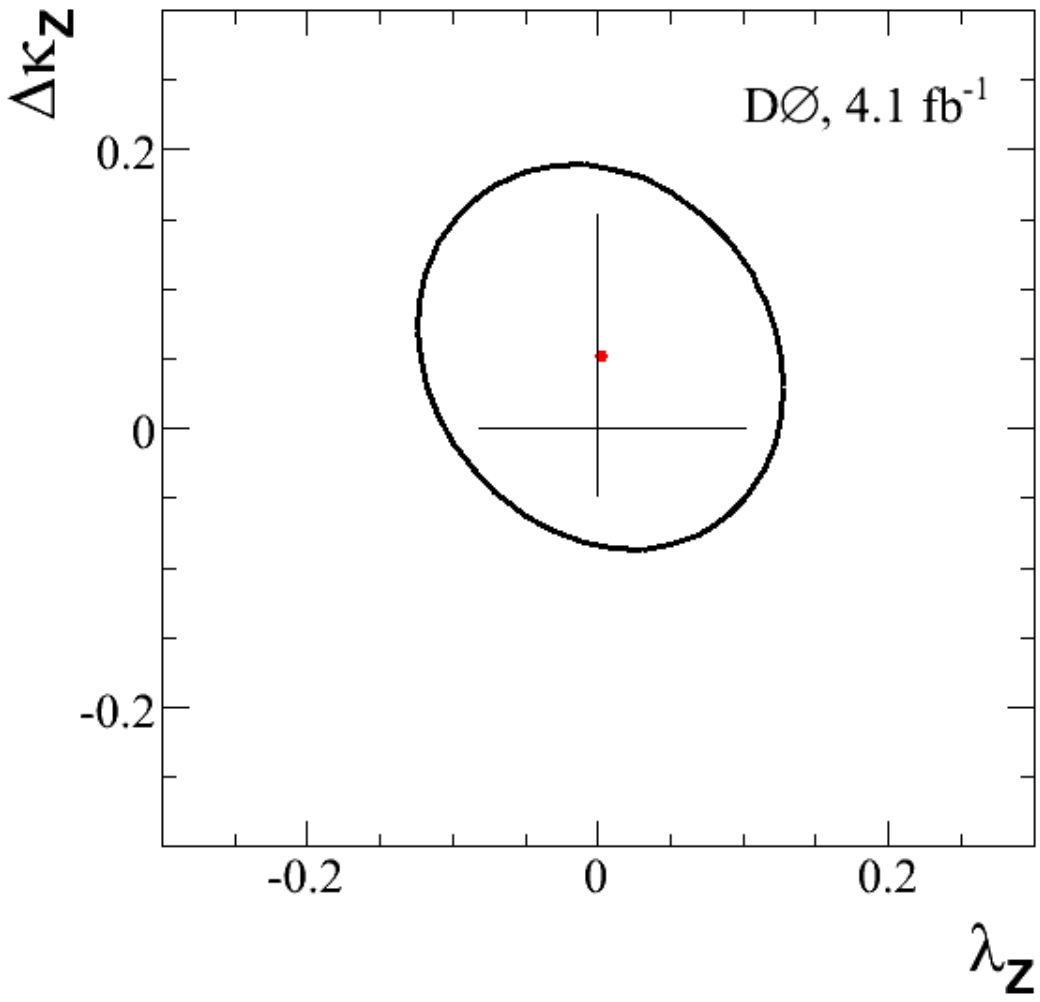

Figure 6.9: *Two-dimensional limit contour for the LEP paratemerization. The point corresponds to the minimum of the likelihood surface. The vertical and horizontal lines represent the separately calculated one-dimensional limits.*

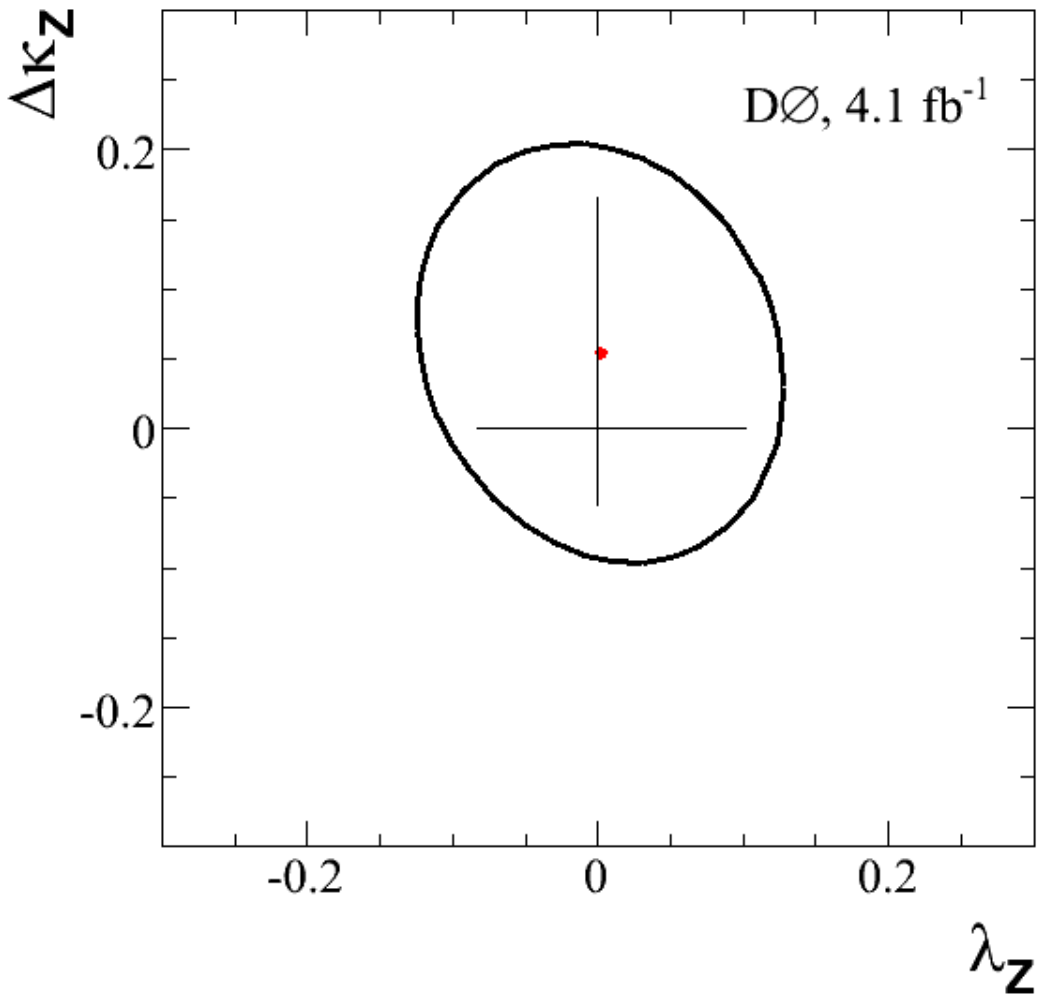

Figure 6.10: *Two-dimensional limit contour for the HISZ parametrization. The point corresponds to the minimum of the likelihood surface. The vertical and horizontal lines represent the separately calculated one-dimensional limits.*

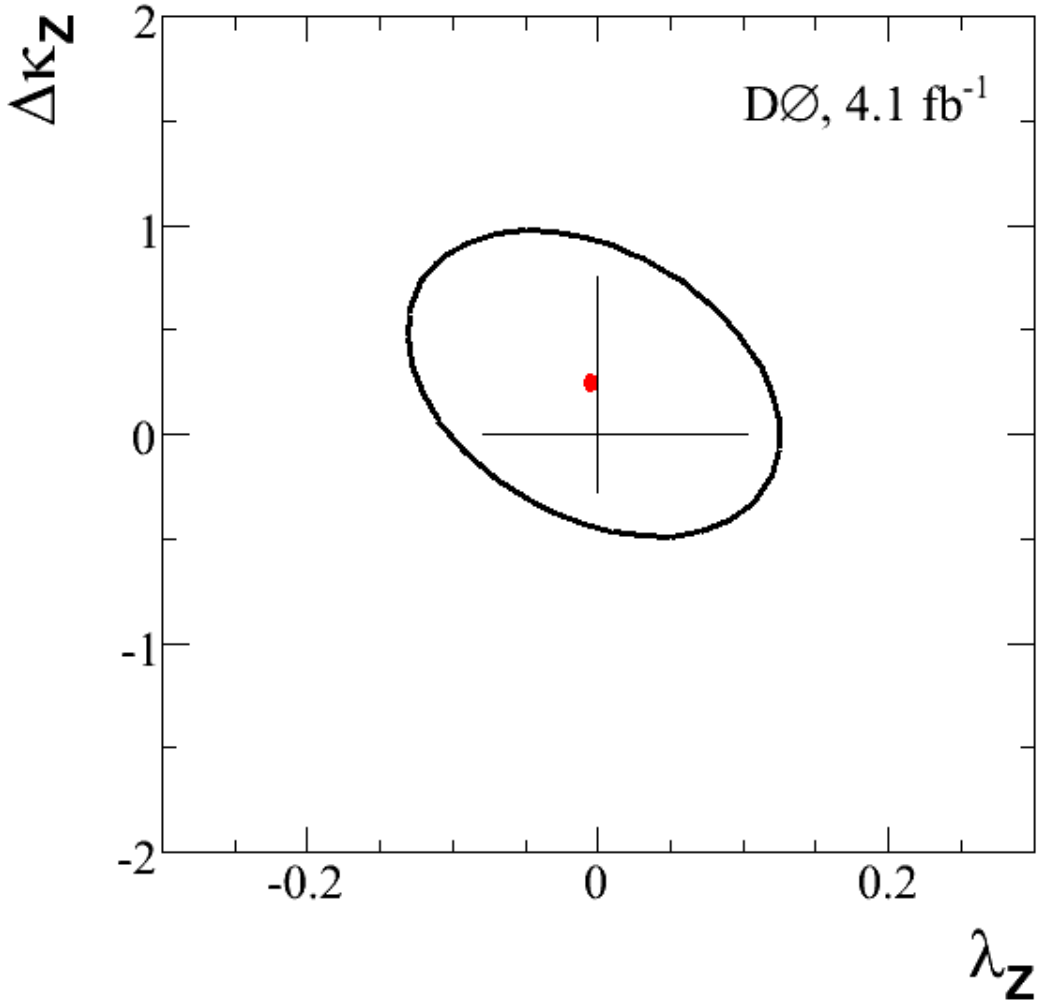

Figure 6.11: *Likelihood surface calculated for the EQUAL parametrization. The overlayed surface is the fit to the likelihood used to interpolate the one- and two-dimensional anomalous coupling limits.*

Chapter 7

Search for New Resonances Decaying into WZ Boson Pairs

As mentioned in the Introduction Chapter of this Dissertation, it is strongly believed that the standard model is only a low energy approximation of more general theory. There are different extension models developed in particle physics trying to describe interactions between fundamental particles at high energies and solve some of the puzzles of the Nature. Some of these models predict existence of new heavy gauge bosons that can decay to the pair of WZ bosons[4–7,55–58].

This chapter describes a search for such particles following models mentioned in Section 2.3. Similarly to the analysis described in the previous Chapter, only fully leptonic decays of the W and Z bosons are considered.

7.1 Data and MC Samples

Data and MC samples used in this analysis are the same as described in Section 5.1. The WZ production is considered here as a background process and estimated from the MC simulation.

The signal process of the W-like boson, usually referred to as a sequential standard model (SSM) W', is generated using PYTHIA with CTEQ6L1 PDFs for W' masses of 180, 190, 200 GeV and then up to 1 TeV in steps of 50 GeV. The width of the W' in the SSM

is determined by the relationship given in Eq. 7.1.

$$\Gamma_{W'}(M_{W'}) = \frac{4}{3}\frac{M_{W'}}{M_W}\Gamma_W \tag{7.1}$$

The SSM W' cross section is known to NNLO in α_S[59]. The cross sections, and SSM branching fractions of the $W' \to WZ$ for each mass point are summarized in Table 7.1. The samples are produced without interference with the standard model WZ production, although this effect is estimated[60] to be negligible. In addition to these samples, simulations with the non-SSM $W'WZ$ couplings and with different helicity of the W and Z bosons are produced to interpret the results in the $W'WZ$ coupling strength $vs.$ W' mass phase space and to study potential systematic effects on acceptance and efficiency of selection criteria.

Other new physics that can be discovered in this final state is the production of new Technicolor resonances that decay into WZ boson pair. These processes are simulated by the PYTHIA generator with the CTEQ6L1 PDF libraries. A conventional low-scale Technicolor parameter space is used: the mass of ρ_T is equal to the mass of ω_T and equal to standard axial and vector masses $M_V = M_A$. The mass of a_T is 10% higher than the mass of the ρ_T, and the mass of the excited η-like techniparticle is sufficiently high, so that the decay to it is suppressed. The charge of the up-type techni-quark is $Q_U = 1$, and the $sin\chi = 1/3$.

All signal and background Monte Carlo samples were overlaid with the Run II minimum bias events to simulate the effect of additional $p\bar{p}$ collisions. The luminosity profile of the minimum bias events are chosen to match the profile of Run IIa and Run IIb triggered data. The Monte Carlo simulations are re-weighted for data luminosity profile, beam-position, and Monte Carlo-data correction factors. The simulation samples are also subjected to the same selection criteria as that applied on data.

7.2 Object Selection

The physics objects used in this analysis are electrons, muons, and missing transverse energy. Four experimental signatures are considered: $eee\nu$, $ee\mu\nu$, $\mu\mu e\nu$, and $\mu\mu\mu\nu$. Electrons are

W' Mass, GeV	$\sigma(W')$, pb	SSM $Br(W' \to WZ)$
180	780	0.003
190	704	0.007
200	635	0.011
250	379	0.019
300	226	0.020
350	135	0.019
400	80.7	0.018
450	48.2	0.017
500	28.8	0.016
550	17.2	0.016
600	10.3	0.015
650	6.13	0.015
700	3.66	0.014
750	2.19	0.014
800	1.31	0.014
850	0.78	0.014
900	0.466	0.013
950	0.278	0.013
1000	0.166	0.013

Table 7.1: *The cross sections and the SSM branching fractions of the $W' \to WZ$ processes simulated in* PYTHIA *for $180 \leq M_{W'} \leq 1000$ GeV.*

reconstructed in the CC and EC, while muons are reconstructed in the muon system. The leptons are required to have tracks reconstructed in the central tracker.

7.2.1 Electron Identification

The same identification criteria are required for electrons from the Z and W boson decays. Those must be of "*Top_tight*" quality. The detailed requirements of this identification criterium in the CC and EC are given in Table 7.2.

Variables	CC	EC
$\mathcal{I}$ <	0.15	0.15
fr_{EM} >	0.90	0.90
$HMx7$ <	50	50
$\chi^2_{spatial}$ >	0.0	–
χ^2 >	–	0.0
E/p <	2.5	–
p_T^{track} >	5	5
$Lhood$ >	0.85	0.85

Table 7.2: *The selection criteria used to select "Top_tight" quality electrons in the CC and EC.*

7.2.2 Muon Identification

The "*Loose*" quality muons are used in this analysis.

Muon quality	nseg	Number of hits
"*Loose*"	$\lvert nseg\rvert = 3$	$N_A^w \geq 2$, $N_A^{sc} \geq 1$, $N_{BC}^w \geq 2$, $N_{BC}^{sc} \geq 1$ (allows 1 test to fail)
"*Loose*"	$nseg = 2$	$N_{BC}^w \geq 2$, $N_{BC}^{sc} \geq 1$
"*Loose*"	$nseg = 1$	$N_A^w \geq 2$, $N_A^{sc} \geq 1$

Table 7.3: *The requirements for "Loose" muon quality.*

The requirements for "*Loose*" quality are summarized in Table 7.3, where *nseg* is the same as defined in Table 5.4. The muon is further required to match to "*Loose*" quality track and satisfy "*NPTight*" isolation (see Section 5.2.3). The efficiencies for "*Loose*" quality

muons are shown in Fig. 7.1. While, the efficiencies for "*Loose*" quality track requirement as well as "$NPTight$" isolation are given in Fig. 5.3.

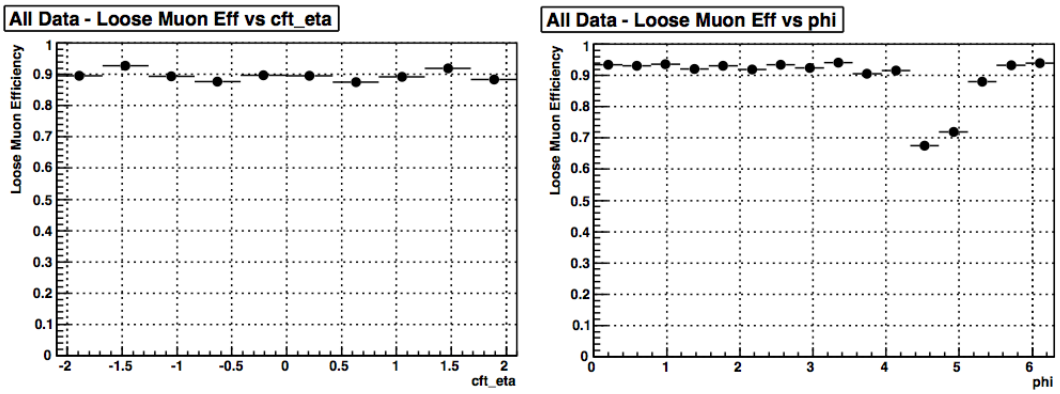

Figure 7.1: *The efficiency for "Loose" quality muons vs. η (left) and ϕ (right).*

7.3 Event Selection

A logical OR of single electron triggers is used for the $3e$ and $2e1\mu$ channels, while the $\mu\mu e$ and $\mu\mu\mu$ channels are selected using logical OR of single muon triggers. The trigger efficiencies to select $W' \to WZ \to \ell\nu\ell\ell$ signal events are calculated using the standard SPC files available for single electron and muon triggers. These efficiencies are estimated to be close to 100% for eee and $ee\mu$ signatures, $97\% \pm 1\%$ for $\mu\mu\mu$ signature, and $90\% \pm 3\%$ for $\mu\mu e$ signature. Combining channels together results in an overall trigger efficiency close to 100% within uncertainties.

Candidate event are selected with at least one reconstructed vertex with at least three associated tracks. The vertex is also constrained to lie within $\pm$60 cm of the detector origin. The presence of at least three charged leptons, electrons and muons, and significant missing transverse energy is required. The leptons must have the transverse momentum greater than 20 GeV and be within the acceptance of the calorimeter or the muon spectrometer in the case of electron and muon, respectively. While the imbalance of momentum in transverse plane must be greater than 30 GeV due to a neutrino in leptonic decay of the W boson.

Out of all possible electron pairs of "*Top_tight*" quality the pair with an invariant mass closest to the nominal Z boson mass is selected to be the electrons from the Z boson decay.

To select events with good $Z \to \mu^+\mu^-$ candidates loose quality muons are considered. A muon candidate must be matched to a loose quality track reconstructed in the central tracker and satisfy the "*NPTight*" isolation (see Section 5.2.3). Muons with opposite charge are considered as the candidates from the Z boson decay, and a pair with the invariant mass closest to the Z boson nominal mass is selected as Z boson decay candidates. For $2\mu 1e$ channel Z boson muon candidates are further required to be of medium quality to increase the trigger efficiency

The Z candidates are required to fall within the $\pm 3\sigma$ window around the nominal Z boson mass. The value of σ is obtained by fitting the dilepton mass in Z candidate data samples to the Gaussian and quadratic polynomial function with the parameterization given below.

$$f(m) = \text{Ampl} \cdot \epsilon^{\frac{(m-\text{Mean})^2}{2\text{Sigma}^2}} + am^2 + bm + c. \tag{7.2}$$

The results of the fits of the dielectron and dimuon mass distributions are given in Figs. 7.2 and 7.3. The σ values are measured to be 3.8 and 6.1 GeV for dielectron and dimuon masses, respectively. Therefore, the Z boson decay candidates are required to have mass between 80 and 102 GeV for dielectron channel, and between 70 and 110 GeV for dimuon one.

Once a Z boson candidate is identified, the highest transverse momentum lepton remaining in the event is identified as the lepton from the W boson decay. This leptons must be separated by $\Delta R > 1.2$ from the Z leptons to suppress $Z + jets$ and $Z\gamma$ backgrounds.

The electron from the W boson decay must satisfy "*Top_tight*" identification, while the muon must be of medium quality and pass "*NPTight*" isolation. In addition, the z-coordinate of tracks of three leptons in final state is required to be within 3 cm, *i.e.*, consistent with being produced in the same vertex. This requirement is 100% efficient and

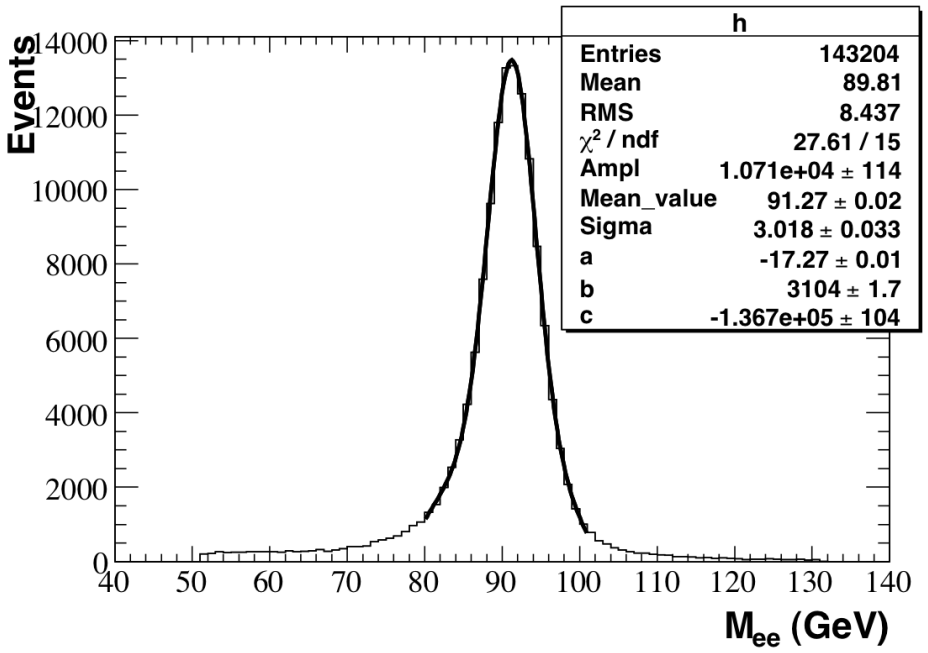

Figure 7.2: *Dielectron invariant mass from Run II data.*

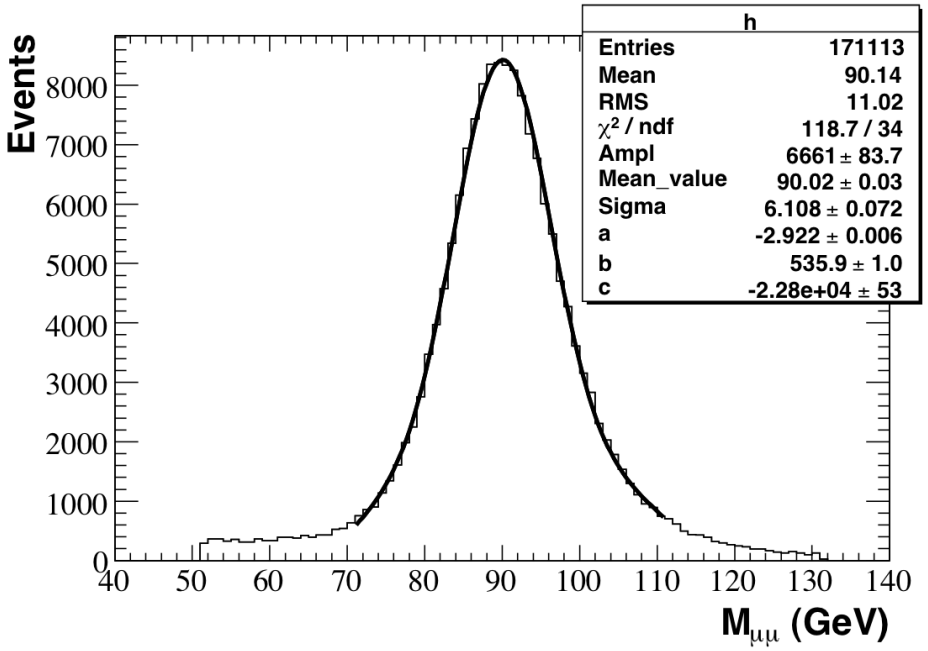

Figure 7.3: *Dimuon invariant mass from Run II data.*

helps to reduce contamination from cosmic muons and mis-reconstructed events.

7.4 Background Estimation and Signal Extraction

The backgrounds to $W' \rightarrow WZ \rightarrow \ell\nu\ell\ell$ final state can be divided into two distinct categories: physics background from the standard model WZ and ZZ production and instrumental backgrounds due to misidentification of a lepton from processes such as $Z + jets$, $Z\gamma$, $W + jets$, and $t\bar{t}$.

The major instrumental background originates from $Z + jets$ processes where a jet is misidentified as either an electron or a muon. The estimation of this contribution is described in Section 7.4.1 using a data-driven method. A $Z\gamma$ background estimation is addressed in Section 7.4.2. Monte Carlo (MC) simulation is used to estimate backgrounds from irreducible WZ production as well as from ZZ, $t\bar{t}$, and $W + jets$ processes. The latter two processes are found to have a negligible contribution to the signal.

7.4.1 Estimation of $Z + jets$ background

The estimation of the $Z + jets$ contribution is done in the same manner as described in Section 5.4.1. The misidentification ratio is measured in multijet sample for "Top_tight" electron identification and "$Medium$" quality muons with "$Loose$" track and "$NPTight$" isolation, following the procedure in Section 5.4.1. It is made sure that the selection of "$false$" lepton in this procedure does not overlap with the selection of leptons from signal process. Therefore, "$false$" electrons are selected with the requirements

- EM fraction > 0.9
- Isolation < 0.2
- $HMx7 > 50$
- $p_T > 15$ GeV.

While "$false$" quality muons must satisfy the criteria

- "$Loose$" quality
- "$Loose$" quality track
- $etHalo > 4.0$ GeV
- $etTrkCone5 > 4.0$ GeV
- $p_T > 15$ GeV
- Cosmic Veto applied.

The misidentification ratios for electron and muon are shown in Fig. 7.4.

The p_T spectrum of "$false$" lepton in the $Z +$ "$false$" lepton normalization sample is further multiplied by the measured misidentification ratios to get the estimated $Z + jets$ background.

7.4.2 Estimation of $Z\gamma$ contribution

The eee and $\mu\mu e$ channels can be mimicked by the $Z\gamma$ initial or final state radiation process. To estimate this background, a procedure described in Section 5.4.2 is followed. The rates at which photon can be misidentified as an electron in data, obtained from $Z(\mu\mu)\gamma$ FSR events, agree with one from MC simulation of $Z(\mu\mu)\gamma$ ISR events, as seen in Fig. 5.8. Then, the misidentification rates for "Top_tight" electron identification are estimated, and those are shown in Fig. 7.5.

To estimate $Z\gamma$ background contribution, here as well, $Z\gamma$ NLO Baur MC sample is used. The NLO cross section of $Z\gamma$ process, $\sigma_{\ell\ell\gamma}$, corresponds to generator level cuts $p_T^{\gamma} > 20$ GeV, $\Delta R(l_{1,2}, \gamma) > 0.4$ is 1.84 ± 0.13 pb. The DØ detector response is simulated by PMCS in order to calculate the acceptance of the signal selection criteria. The certified muon and electron identification efficiencies, obtained from data, are used to measure efficiency of the

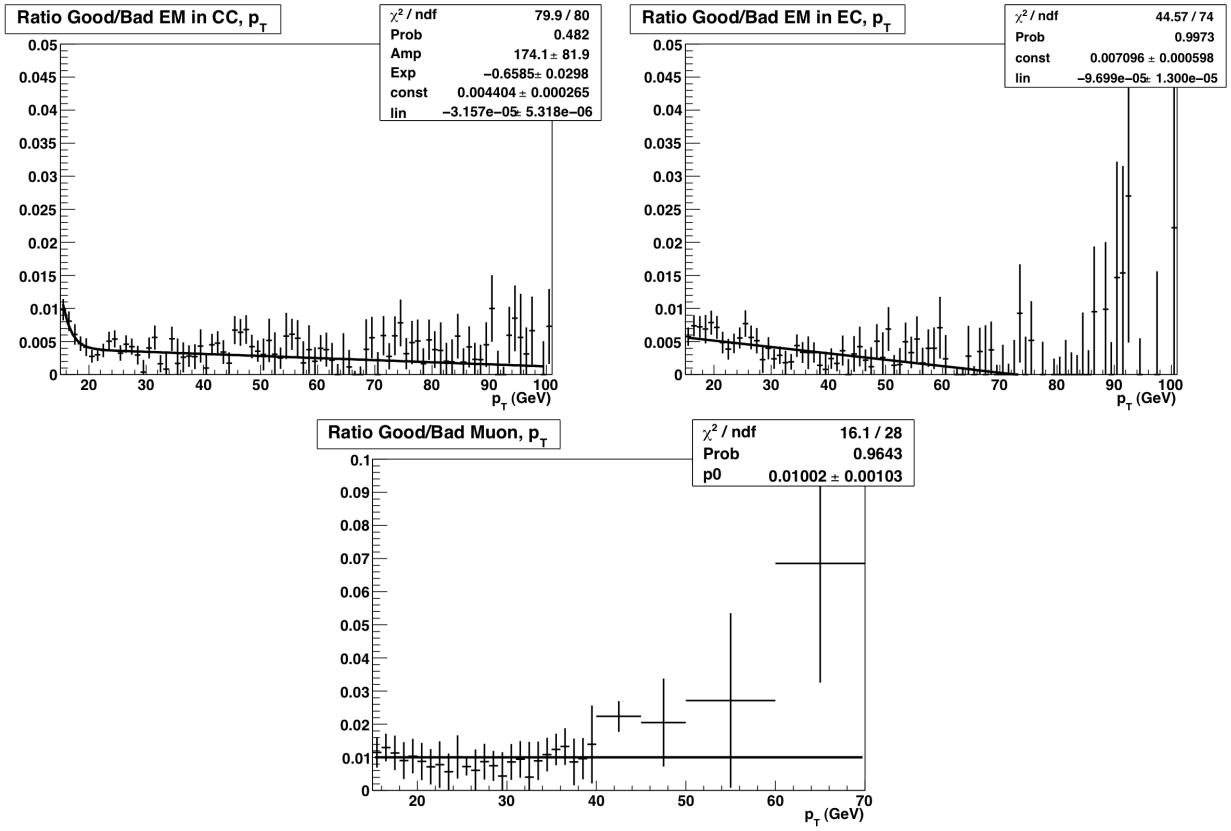

Figure 7.4: *The electron misidentification ratios vs. p_T for "Top_tight" identification in CC (top left) and EC (top right). The misidentification ratio for "Medium" quality muons with "Loose" track and "NPTight" isolation (bottom).*

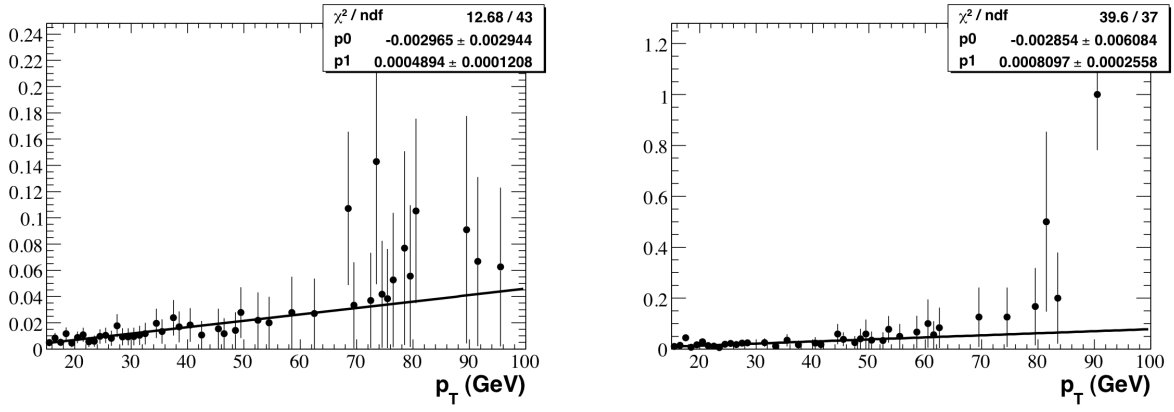

Figure 7.5: *The rate at which a photon is misidentified as an electron as a function of p_T for "Top_tight" electron definitions in the CC (left) and in the EC (right).*

selection criteria. Following Eq. 5.2, $Z\gamma$ background is estimated for eee and $\mu\mu e$ decay signatures, and the results are summarized in Table 7.4.

Channels	Baur+PMCS sample
eee	0.025 ± 0.001
$\mu\mu e$	0.069 ± 0.002

Table 7.4: *Estimated $Z\gamma$ events from Baur Monte Carlo sample processed via* PMCS. *The uncertainties are statistical.*

The signal selection requirement that induces the largest systematic uncertainty is the requirement on the $\not\!\!E_T$ in the event. As the $Z\gamma$ final state does not have true $\not\!\!E_T$, the efficiency of the $\not\!\!E_T$ requirement depends very strongly on how well the simulation describes the $\not\!\!E_T$ resolution in data and also how much the $\not\!\!E_T$ resolution depends on the composition and energy of the final state particles. To estimate these dependences, $\not\!\!E_T$ is plotted in three samples that do not have true $\not\!\!E_T$: the $Z \to \ell\ell$ data sample and the MC simulations of $Z\gamma$ initial state radiation and $Z + jets$ processes (see Fig. 7.6). The $\not\!\!E_T$ distributions are found to vary significantly in the tails that results in significant difference in the efficiencies of the $\not\!\!E_T$ requirement estimated from these samples (see Table 7.5).

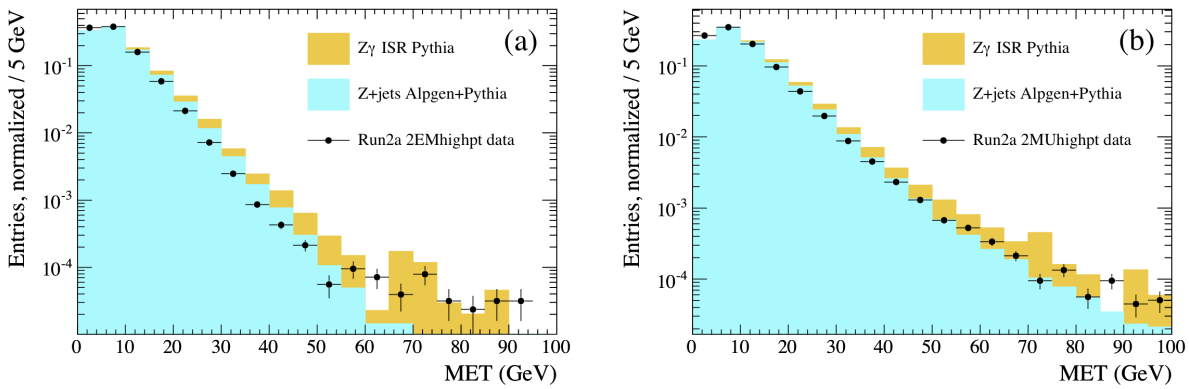

Figure 7.6: *The $\not\!\!E_T$ distribution obtained from data (black points), $Z\gamma$* PYTHIA *Monte Carlo simulation (yellow histogram), and $Z+jets$* ALPGEN+PYTHIA *Monte Carlo simulation (blue histogram) for $Z \to e^+e^-$ (a) and $Z \to \mu^+\mu^-$ (b).*

Channels	Data	$Z\gamma$ MC	$Z + jets$ MC
eee	0.005 ± 0.001	0.014 ± 0.001	0.009 ± 0.001
$\mu\mu e$	0.022 ± 0.003	0.035 ± 0.004	0.025 ± 0.002

Table 7.5: *The efficiency of the $\not\!\!E_T$ requirement obtained from the $Z \to \ell\ell$ data sample and the MC simulations of $Z\gamma$ initial state radiation and $Z + jets$ processes.*

In estimation of the $Z\gamma$ background, the $\not\!\!E_T$ efficiency from the Run IIb $Z\gamma$ PYTHIA simulation sample is used, as it has the exact composition and energy behavior of the background process. Relying on $\not\!\!E_T$ resolution from RunIIb sample can result in an overestimation of the background. Thus, a conservative 100% systematic uncertainty is assumed on this background contribution. As the background contribution to the signal is very small, this assumption does not significantly affect the results.

7.5 Results

7.5.1 Systematic Uncertainties

In this analysis several sources of systematic uncertainty are considered. The uncertainty on integrated luminosity is 6.1%. The uncertainty on the PDFs is estimated to be 5%. The uncertainty on electron identification efficiency due to the Monte Carlo simulation and p_T dependence is estimated to be 6% per electron. The uncertainty on the muon identification efficiency is 4% per muon The uncertainties due to same flavor leptons are considered to be fully correlated. A conservative systematic uncertainty of 15% due to the combined effects on trigger, lepton identification, and acceptance is taken as fully correlated between signal and background samples extracted from Monte Carlo simulation. $Z + jets$ and $Z\gamma$ contributions have the largest systematic uncertainties of 40% and 100% due to the fake rate estimation and limited statistics of the $Z +$ "$false$" lepton normalization sample for the former and the $\not\!\!E_T$ modeling in Monte Carlo simulation for the latter sources. The systematic uncertainties are summarized in Table 7.6. All systematic uncertainties are assumed not to depend on the WZ transverse mass.

Source	Uncertainty
Luminosity	6.1%
Acc$\times\epsilon_{\text{trigger}} \times \epsilon_{\text{ID}}$	20%
$Z + jets$	40%
$Z\gamma$	100%
Theory	5%

Table 7.6: *Systematic uncertainties.*

7.5.2 $W' \to WZ \to \ell\nu\ell\ell$ Event Yields

After the selection criteria are applied, two events are observed in the Run IIa data, and seven events are observed in the RunIIb data. This is consistent with the standard model prediction of 3.05 ± 0.11 and 7.17 ± 0.27 events (uncertainties are statistical) in Run IIa and Run IIb, respectively. The summary of observed events with expected backgrounds for Run IIa and Run IIb is given in Table 7.7. Data, signal and background events break down for four channels separately is given in Table 7.8.

	Data set	
Source	Run IIa	Run IIb
W'(500 GeV)	1.11 ± 0.02	3.24 ± 0.07
WZ	2.69 ± 0.11	6.31 ± 0.26
ZZ	0.28 ± 0.02	0.67 ± 0.06
$Z + jets$	0.05 ± 0.02	0.11 ± 0.03
$Z\gamma$	0.026 ± 0.001	0.068 ± 0.002
$t\bar{t}$	0.002 ± 0.001	0.008 ± 0.002
Total	3.05 ± 0.11	7.17 ± 0.27
Observed	2	7

Table 7.7: *Observed events, signal and background estimation for Run IIa and Run IIb data set. The uncertainties are statistical.*

The number of observed candidates and expected signal and background processes for the full data set with total statistical and systematic uncertainties is summarized in Table 7.9.

The transverse mass of hypothetical heavy resonance decaying into WZ boson pairs is

Mode	Data	Total	WZ	ZZ	$Z + jets$	$Z\gamma$	$t\bar{t}$	W'
eeeν	3	1.52 ± 0.10	1.4 ± 0.1	0.07 ± 0.01	0.02 ± 0.01	0.025 ± 0.001	0.003 ± 0.001	1.07 ± 0.03
ee$\mu\nu$	2	2.31 ± 0.11	2.0 ± 0.1	0.24 ± 0.03	0.07 ± 0.03	n/a	0.003 ± 0.001	1.17 ± 0.03
e$\mu\mu\nu$	2	2.21 ± 0.10	2.0 ± 0.1	0.10 ± 0.02	0.04 ± 0.01	0.069 ± 0.002	0.002 ± 0.001	0.83 ± 0.03
$\mu\mu\mu\nu$	2	4.19 ± 0.21	3.6 ± 0.2	0.54 ± 0.05	0.05 ± 0.02	n/a	0.001 ± 0.001	1.28 ± 0.04

Table 7.8: *Observed events, signal and background estimation for each signature separately for full Run 2 data set. The signal corresponds to 500 GeV of W' mass hypothesis. The uncertainties are statistical.*

Source	Total
W'(500 GeV)	4.35 ± 1.14
WZ	9.01 ± 1.48
ZZ	0.96 ± 0.17
$Z + jets$	0.17 ± 0.08
$Z\gamma$	0.094 ± 0.094
$t\bar{t}$	0.010 ± 0.003
Total	10.24 ± 2.13
Observed	9

Table 7.9: *Observed events, signal and background estimation with total uncertainties for the whole Run II data set.*

calculated as follows

$$M_T = \sqrt{((E_T^Z + E_T^W)^2 - (p_x^Z + p_x^W)^2 - (p_y^Z + p_y^W)^2)}. \quad (7.3)$$

The WZ transverse mass with two W' hypotheses overlaid is given in Fig. 7.8. The event display of one of the observed candidates with high WZ transverse mass ($M_T(WZ) =$ 202 GeV) is shown in Fig. 7.7

Dilepton mass distribution and W transverse mass for selected candidates and background events are shown on Figs. 7.9 and 7.10.

7.5.3 Limits on W' signal

As data agree with the standard model background prediction, limits on W' production are set using the modified frequentist approach implemented in the standard DØ likelihood fitter[61]. The fitter incorporates a log-likelihood ratio (LLR)[62,63] statistical method. The value of the confidence level for the signal CL_s is defined as a ratio of CL_{s+b}/CL_b, where CL_{s+b} and CL_b are confidence levels for the signal plus background hypothesis and the background-only (null) hypothesis, respectively. The LLR distributions for these hypothesis are obtained by simulating the outcomes using Poisson statistics. The confidence levels are evaluated by integrating the corresponding LLR distributions. Systematic uncertainties are treated as uncertainties on the expected number of signal and background events,

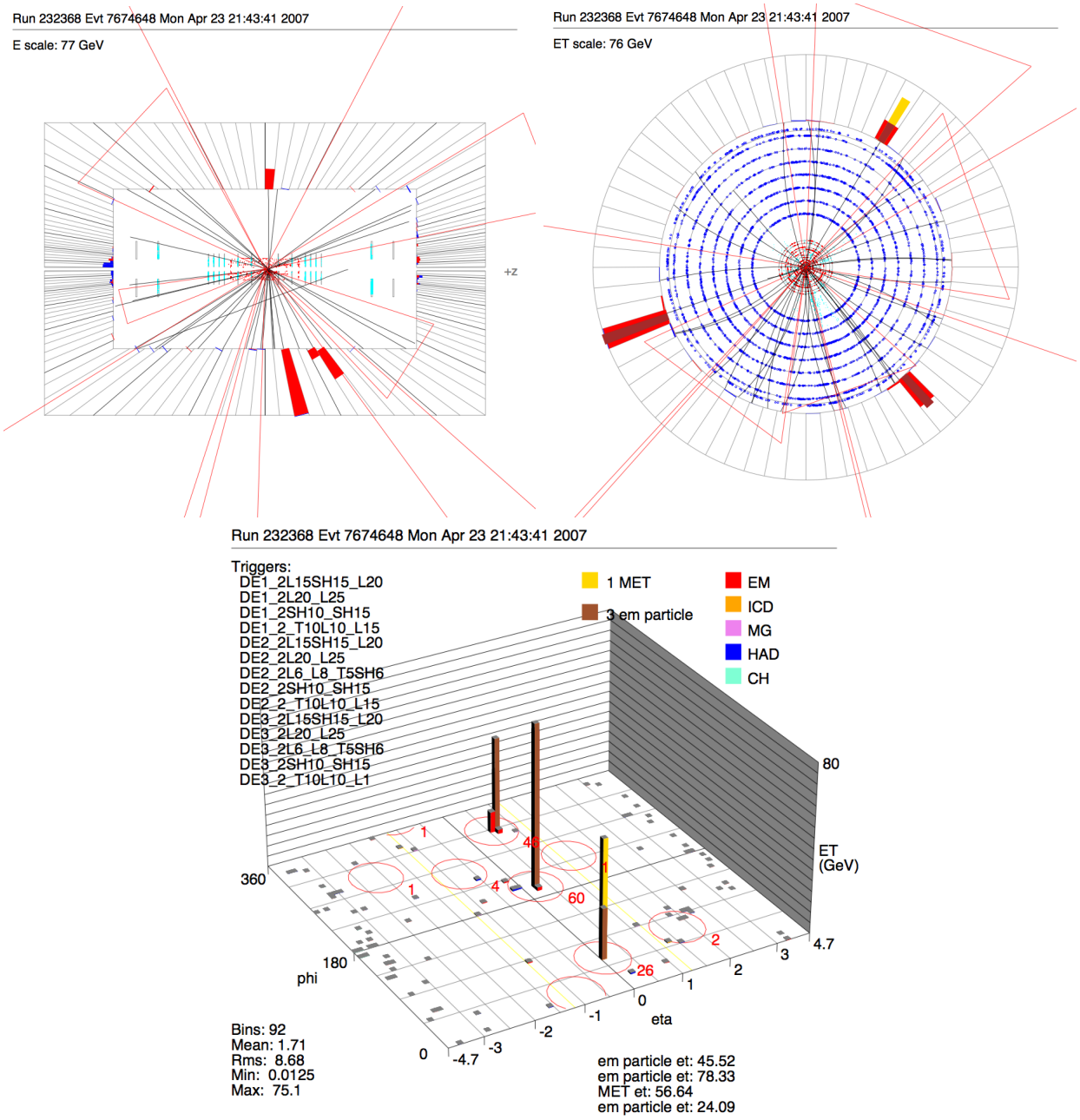

Figure 7.7: *Event display of a $W' \to WZ \to eee\nu$ candidate event is given in the $y-z$ plane (top left), the $x-y$ plane (top right), and 3D lego plot (bottom).*

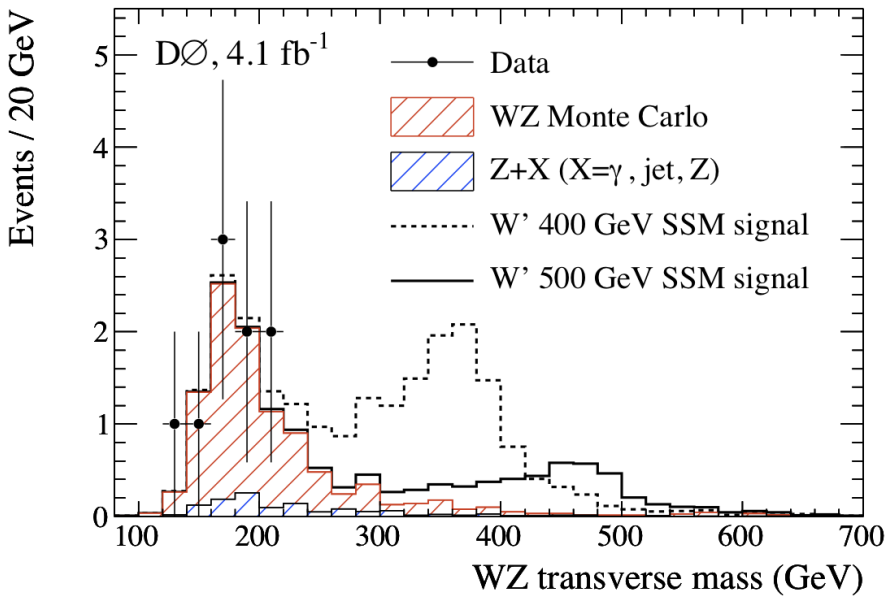

Figure 7.8: *WZ transverse mass is given as black circles with the standard model backgrounds overlaid. The expected W' SSM signal hypotheses for 400 GeV (dashed line) and 500 GeV (solid line) W' mass are displayed as a dashed and a solid line, respectively.*

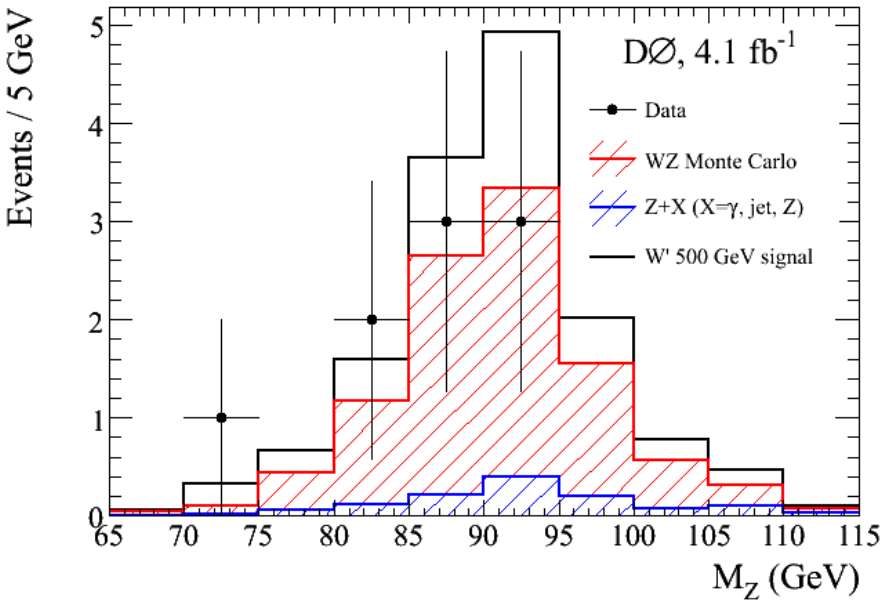

Figure 7.9: *Dilepton invariant mass is given as black circles with standard model backgrounds overlaid. The expected SSM W' boson signal hypothesis for 500 GeV mass is displayed as a solid line.*

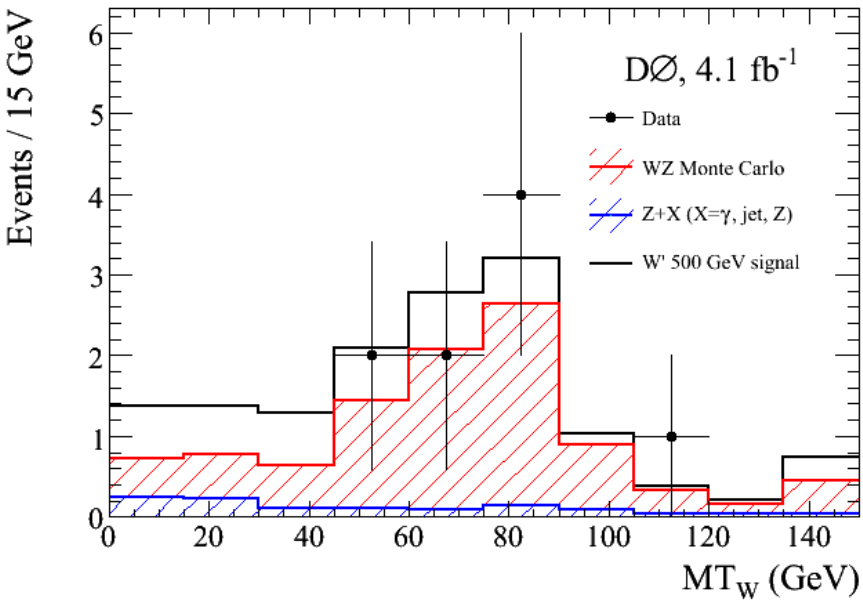

Figure 7.10: *W transverse mass is given as black circles with standard model backgrounds overlaid. The expected SSM W′ boson signal hypothesis for 500 GeV mass is displayed as a solid line.*

not the outcomes of the limit calculations. This approach ensures that the uncertainties and their correlations are propagated to the outcome with their proper weights. In limit setting procedure WZ transverse mass distribution is used from data, signal, and expected background processes (see Fig. 7.8). The distribution is re-binned so that no bins in the distribution have zero background prediction.

The limit as a function of the W' mass hypothesis is given in Fig. 7.11. The W' masses between 188 GeV and 520 GeV are excluded at 95% C.L. assuming the sequential standard model W'. That agrees well with the expected 95% C.L. limit on the SSM W' masses between 188 GeV and 497 GeV.

We also study the sensitivity to other models that predict a W' with stronger coupling to the WZ boson pair. Both W' production cross section and $Br(W' \to WZ)$ are affected by the variation of $W'WZ$ coupling. The upper bounds on the W' mass as a function of the $W'WZ$ coupling is given in Fig. 7.12 and the results are summarized in Table 7.10. The two dimensional exclusion limit as a function of $W'WZ$ coupling and W' mass is shown in Fig. 7.13.

$W'WZ$	Observed exclusion (GeV)	Expected exclusion (GeV)
1 (SSM)	520	497
4	767	752
9	903	881

Table 7.10: *Observed and expected exclusions for different values of relative coupling strength.*

The stronger couplings between W' and the WZ, predicted by other models, would also increase the width of W', that is no longer consistent with the SSM prediction given in Eq. 7.1. The robustness of our results to the width of the resonance is studied using the samples of W' with width up to 25% of the mass of resonance (see Fig. 7.14) while assuming the sequential SM expectation for each mass hypothesis. As seen in Fig. 7.15, the limits degrade but stay within 1 s.d. band around the expected limit. Thus, the results are valid for the models predicting $W' \to WZ$ resonance with width up to 25% of mass of the

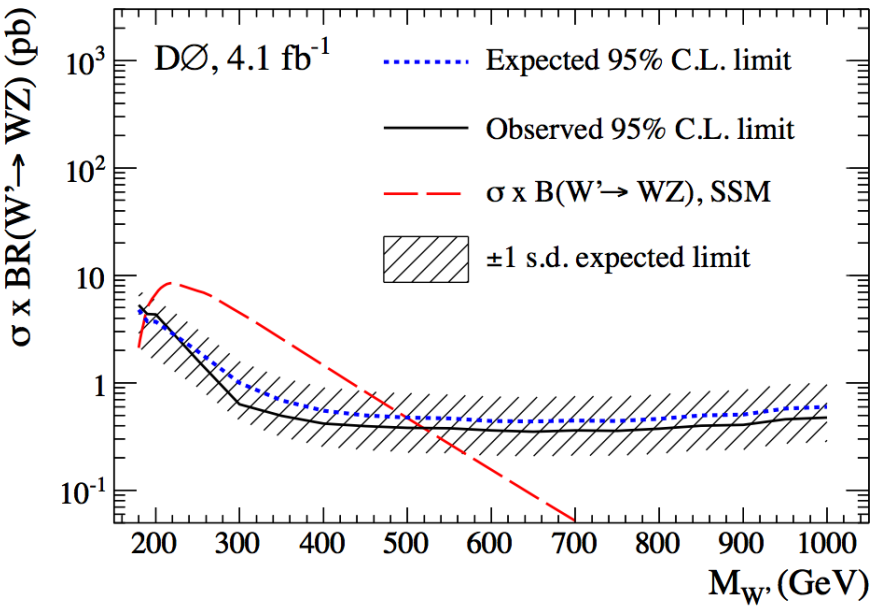

Figure 7.11: *Observed and expected 95% C.L. upper limits and ±1 s.d. band around the expected limits on the cross section multiplied by $Br(W' \to WZ)$ with the SSM prediction overlaid.*

resonance. The latter corresponds to the strength of the $W'WZ$ coupling of about 20 times that of the SSM value.

These results are robust to $\not\!\!E_T$ description in MC simulation. This is verified by artificially inflating the $\not\!\!E_T$ resolution by 30% in signal and background MC samples, Fig. 7.16, and recalculating WZ transverse mass, see Fig. 7.17. The limits worsened by 1%. As $\not\!\!E_T$ in MC simulation is described much better after applying data driven corrections than in this exercise, the systematic uncertainty due to the $\not\!\!E_T$ modeling is neglected in the analysis.

7.5.4 Limits on Technicolor

The results are also interpreted within the low-scale Technicolor model predicting $\rho_T \to WZ$ decay. As the final state bosons in techni-rho are longitudinally-polarized, the acceptance times efficiency of the selection criteria is checked for longitudinally-polarized bosons from the decay of the resonant states with masses 300, 700, and 1000 GeV and found these to be

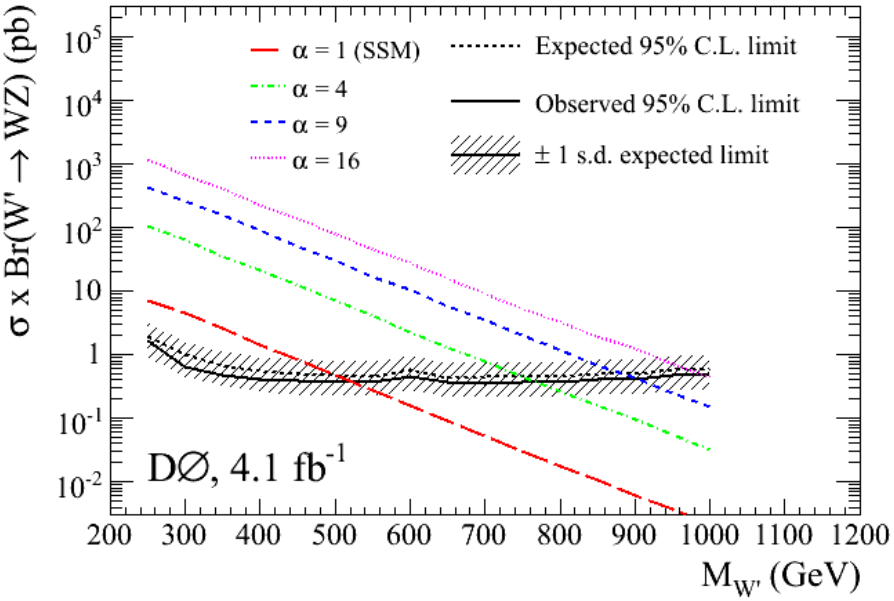

Figure 7.12: *Cross-section times branching fraction 95% C.L. upper limits for the* $W' \to WZ \to \ell\nu\ell\ell$ *production. The lines correspond to theoretical cross section times* $Br(W' \to WZ)$ *for different strengths of the trilinear* $W'WZ$ *coupling normalized to the SSM value* (α). *The dashed area illustrates the 1 s.d. band around the expected limits.*

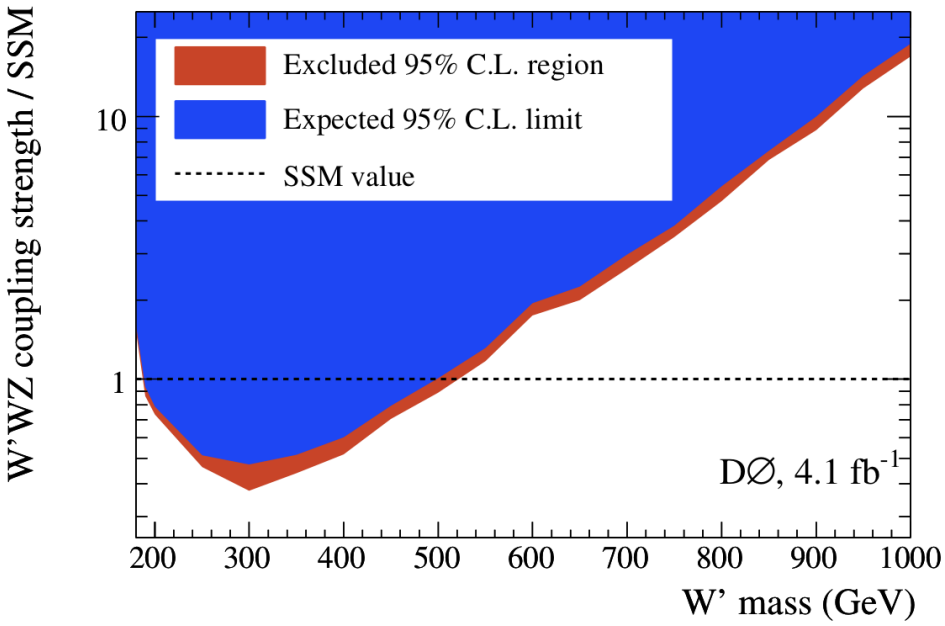

Figure 7.13: *Expected and excluded areas of the $W'WZ$ coupling strength normalized to the SSM value as a function of the W' mass.*

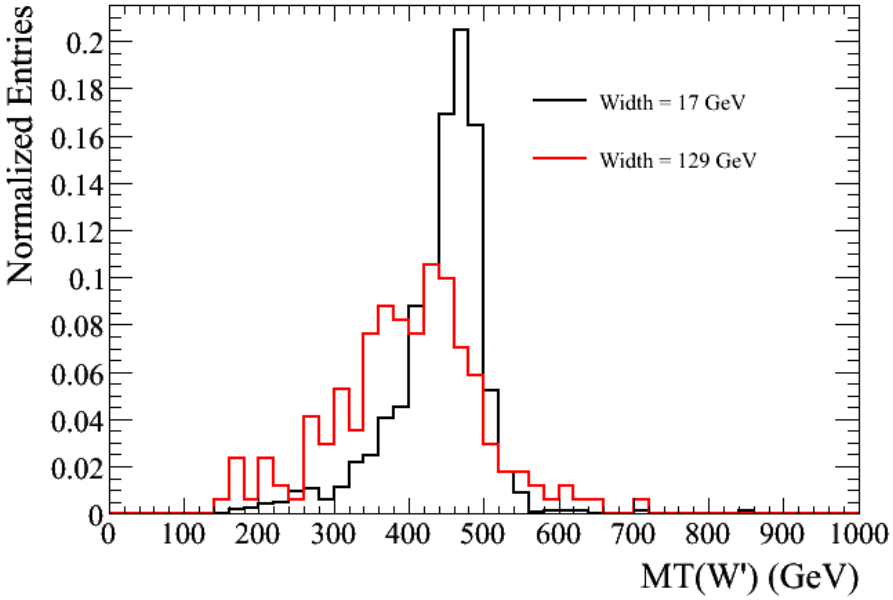

Figure 7.14: *The transverse mass of the W' boson of 500 GeV mass hypotheses with nominal width (black) and with the width of ∼25% of W' mass (red).*

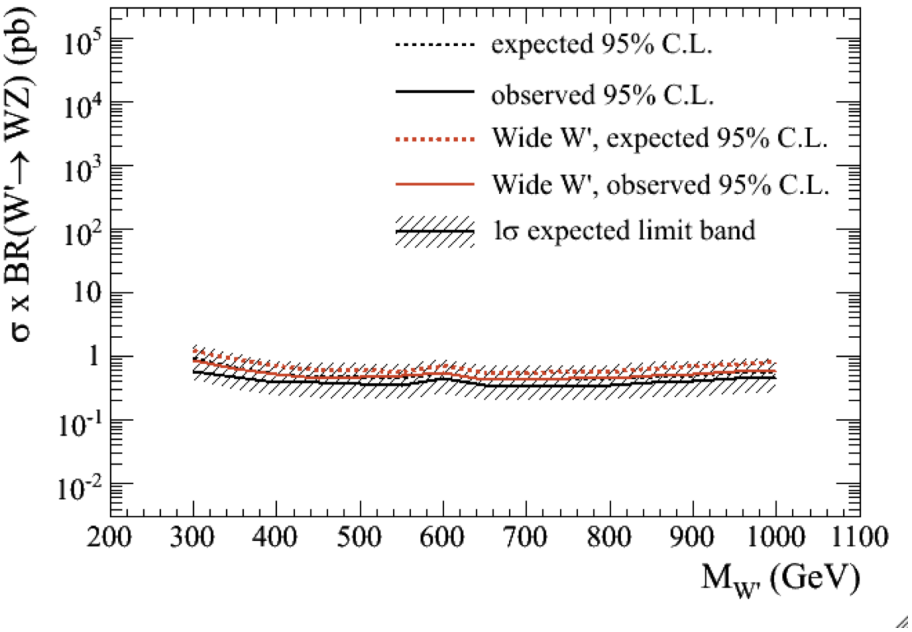

Figure 7.15: *The limits obtained for narrow (black) and wide (red) signal hypotheses. The width of wide signal corresponds to 25% of the mass.*

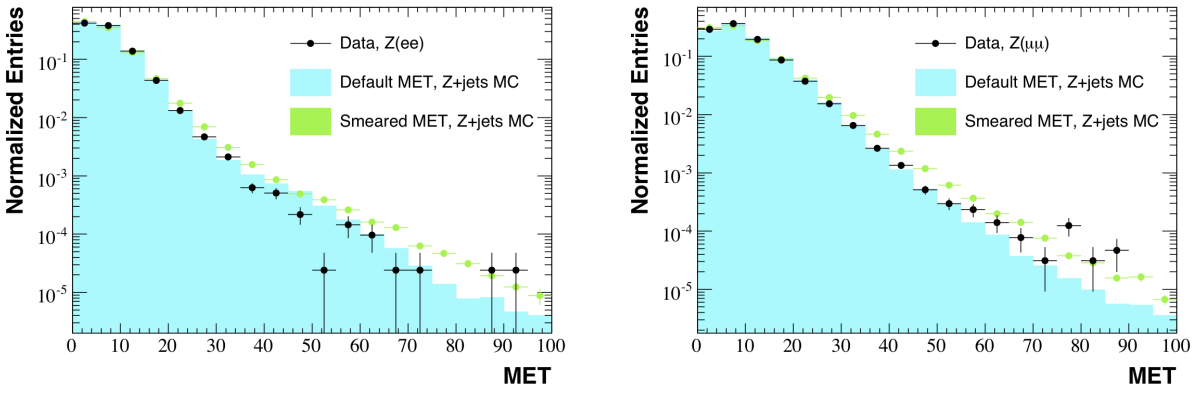

Figure 7.16: *$\not\!\!E_T$ distribution obtained from data (black points), and Z + jets* ALPGEN+PYTHIA *Monte Carlo simulation with the default $\not\!\!E_T$ (blue histogram) and 30% smeared $\not\!\!E_T$ (green points) for $Z \to e^+e^-$ (a) and $Z \to \mu^+\mu^-$ (b).*

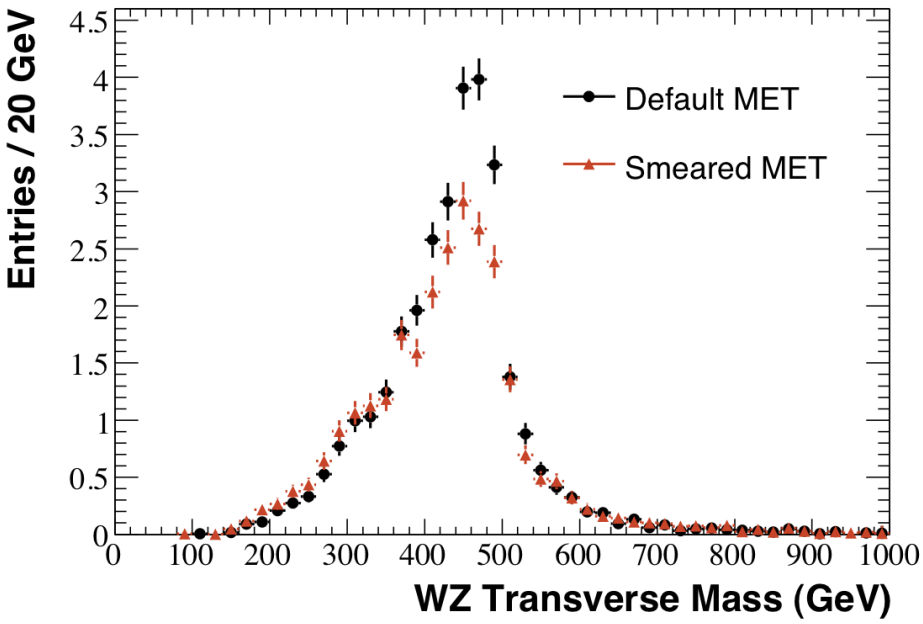

Figure 7.17: *WZ transverse mass for 500 GeV signal hypotheses for original resolution (black circles) and by 30% inflated resolution (red triangles) of $\not\!\!E_T$.*

the same compared with the values estimated from the $W' \to WZ$ MC samples.

The LO cross sections and branching fraction of the $\rho_T \to WZ$ process is obtained using PYTHIA generator. The NLO estimation is obtained using the constant k-factor of 1.3. Following a typical LSTC phenomenology the Technicolor resonances are generated with relations: $M(a_T) = 1.1M(\rho_T)$, $M(\rho_T) = M(\omega_T)$, $M(\eta'_T) >> M(\rho_T)$, $Q_U = 1$, $\sin(\chi) = 0.3333$, and $M_{V_{1;2;3}} = M_{A_{1;2;3}} = M(\rho_T)$. The branching fractions of $\rho_T \to WZ$ and $a_T \to WZ$ strongly depend on the relative mass of the techni-pion π_T: if $M(\pi_T) < 0.5M(\rho_T)$ the dominant ρ_T decay mode is $\rho_T \to \pi_T\pi_T$. If $0.5M(\rho_T) < M(\pi_T) < M(\rho_T) - M(W)$, then ρ_T decays mostly to $W\pi_T$. If the π_T is sufficiently heavy, so that $W\pi_T$ decay mode is kinematically forbidden, ρ_T mostly decays to WZ. Thus, the results are interpreted in two dimensional plane of the masses of the π_T and ρ_T (see Fig. 7.18). For $M(\pi_T) > M(\rho_T) - M(W)$, the ρ_T mass is excluded from 208 to 400 GeV at 95% C.L., while the expected exclusion is from 201 to 339 GeV.

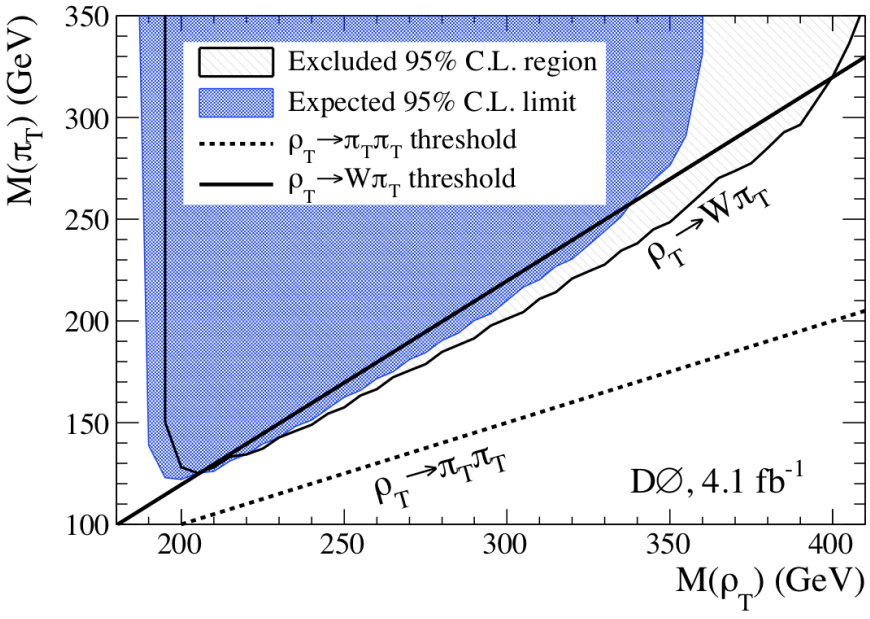

Figure 7.18: *Expected and excluded areas of the π_T vs. ρ_T masses are given with the thresholds of the $\rho_T \to W\pi_T$ and $\rho_T \to \pi_T\pi_T$ decays overlaid.*

Chapter 8

Conclusion

In summary, the thorough study of the diboson $WZ \to \ell\nu\ell\ell$ process at the $p\bar{p}$ Tevatron collider was described in this Dissertation. Collision events were recorded by the DØ detector and data correspond to 4.1 fb^{-1} of integrated luminosity. The detailed description of detection and reconstruction of collision data, selection of the events, and estimation of background processes were given. The analyses probe for both the SM predictions and new phenomena searches and several results are summarized below.

- The $p\bar{p} \to WZ$ production cross section of $3.90^{+1.01}_{-0.85}(stat + syst) \pm 0.31(lumi)$ pb is obtained, which is in a good agreement with the NLO prediction of 3.25 ± 0.19 pb[41]. This is the most precise measurement to date of the WZ cross section.

- No evidence for anomalous WZ production is found and 95% C.L. limits are set on CP-conserving coupling parameters, assuming a form-factor scale $\Lambda = 2$ TeV. The limits on WWZ couplings are interpreted for three commonly known relations between WWZ and $WW\gamma$ couplings:

  - LEP relation: $-0.08 < \lambda_Z < 0.10$ and $-0.05 < \Delta\kappa_Z < 0.15$
  - HISZ relation: $-0.08 < \lambda_Z < 0.10$ and $-0.06 < \Delta\kappa_Z < 0.17$
  - EQUAL coupling relation: $-0.08 < \lambda_Z < 0.10$ and $-0.28 < \Delta\kappa_Z < 0.76$

Those are most restrictive limits on WWZ couplings obtained in the direct measurement of the WWZ vertex that is only accessible at hadron colliders.

- For the first time a search for new heavy resonances decaying into WZ boson pair is performed. No evidence for such resonances is observed and these results are interpreted within some of the new phenomena models:

  - Limits are set on a hypothetical WZ resonance production cross section times $Br(W' \to WZ)$. These limits exclude sequential SM W' boson with mass between 188 GeV and 520 GeV. This is the first limit to-date on resonant $W' \to WZ$ production and is complementary to the previous searches of the W' decaying to fermions. These results are also valid for other models that predict a wider, compared to sequential SM, W'-like resonance with width value of up to 25% of the resonance mass. These results are also interpreted for the first time in terms of $W'WZ$ trilinear couplings.

  - The limits on the resonant WZ production cross section $\sigma \times B(W' \to WZ)$ yield stringent constraints on the low-scale Technicolor. A low-scale Technicolor resonance ρ_T is excluded for with mass between 208 and 408 GeV at 95% C.L. with heavy techni-pion hypothesis ($M(\pi_T) > M(\rho_T) - M(W)$). These are the most stringent constraints on a typical LSTC phenomenology model[64] when ρ_T decays predominantly to WZ boson pair.

The results of searches for new heavy resonances, described in Section 7, have been published[65] in Physical Review Letters and results on measurement of the WZ production cross section and limits on anomalous triple gauge couplings, described in Sections 5 and 6, are to be submitted to Physics Letter B. The results used in this analysis are also being used in combination with semi-leptonic WZ decay modes, *i.e.*, $\ell\ell jj$ and $\ell\nu jj$ decay signatures. These combined results are expected to be published in summer 2010.

Although no evidence for new physics is found, and the standard model is still the model for fundamental particles and their interactions, this Dissertation provides a significant impact to the field of high energy physics. Very precise measurements of WZ production and the agreement with the standard model prediction indicates that if new phenomena exists in the WZ production, it will require large data samples to be discovered in the future. The results of this Dissertation almost completely exclude the low-scale Technicolor with heavy techni-pions, thus, indicating that the origin of the electroweak symmetry breaking cannot originate from this model with the typical parameter space.

Finally, this Dissertation outlines numerous data analysis methods that will directly contribute to potential future discoveries at the experiments at the new energy frontier, the Large Hadron Collider (LHC). The author contributed significantly to future WZ analyses being a member of the CMS collaboration, and some of this work is summarized in Appendices A and B.

Bibliography

[1] B. . Abbott et al.

[2] D. Z. K. Hagiwara, R. D. Peccei and K. Hikasa, Nucl. Phys. B **282**, 253 (1987).

[3] J. W. K. Hagiwara and D. Zeppenfeld, Phys. Rev. D **41**, 2113 (1990).

[4] P. Langacker, Rev. Mod. Phys. **81**, 1199 (2009).

[5] K. Lane, arXiv:hep-ph/0202255v1 (2002).

[6] K. Lane and E. Eichten, Phys. Lett. B **669**, 235 (2008).

[7] K. Lane, Phys. Rev. D **60**, 075007 (1999).

[8] A. Abulencia et al., Phys. Rev. Lett. **98**, 161801 (2007), (CDF Collaboration).

[9] V. Abazov et al., Phys. Rev. D **76**, 111104 (2007), (DØ Collaboration).

[10] D. Acosta et al., Phys. Rev. Lett. **90**, 081802 (2003).

[11] A. Abulencia et al., Phys. Rev. D **75**, 091101.

[12] V. Abazov et al., Phys. Rev. Lett. **100**, 211803 (2008), (DØ Collaboration).

[13] V. Abazov et al., Phys. Rev. Lett. **98**, 221801 (2007), (DØ Collaboration).

[14] L. Lederman, Scientific American **264(3)**, 48 (1991).

[15] C. W. Schmidt and C. D. Curtis, IEEE Transactions on Nuclear Science **NS-26**, 4120 (1979).

[16] C. D. Curtis et al., IEEE Transactions on Nuclear Science .

[17] E. L. Hubbard et al., *Booster synchrotron*, FERMILAB-TM-0405, 1973.

[18] C. S. Mishra, Presented at Particles and Fields 92: 7th Meeting of the Division of Particles Fields of the APS (DPF 92), Batavia, IL, 10-14 Nov 1992.

[19] S. Nagaitsev et al., AIP Conf. Proc. **821**, 39 (2006).

[20] S. Abachi et al., Nucl. Inst. Methods **A338**, 185 (1994), (DØ Collaboration).

[21] S. Abachi et al., *The DØ Upgrade: The Detector and its Physics*, FERMILAB-PUB-96/357-E, 1996, (DØ Collaboration).

[22] V. M. Abazov et al., Nucl. Inst. Methods **A565**, 463 (2006), (DØ Collaboration).

[23] G. Bernardi et al., *Improvements from the T42 Algorithm on Calorimeter Objects Reconstruction*, DØ Note 4335, 2004.

[24] G. Borissov, *Ordering a Chaos or... Technical Details of AA Tracking*, All DØ Meeting, 2005.

[25] A. Khanov, *HTF: histogramming method for finding tracks. The algorithm description*, DØ Note 3778.

[26] H. Greenlee, *The DØ Kalman Track Fit*, DØ Note 4303.

[27] F. Fleuret, *The DØ Electron/Photon Analysis Package EMAnalyze*, DØ Note 3888.

[28] J. G. R. I. A. L. D. Chapin, H. Fox and J. Zhu, *Measurement of $Z \to ee$ and $W \to e\nu$ Production Cross Sections Using One Tight Central Electron"), NOTE = DØ Note 4897.*

[29] J. H. T. Andeen and H. Schellman, *Electron Level Energy Correction in DØ Reconstruction p14 pass 2*, DØ Note 5104.

[30] M. Aoki et al., *Electron like for p20 data*, DØ Note 5675.

[31] E. Busato and A. Bernard, *Jet Algorithms in DØ Run II Software: Description and Users Guide*, DØ Note 4457.

[32] L. Sawyer and A. L. Stone, *Missing ET Reconstruction: Variable and Methods*, DØ Note 3957.

[33] Common samples group, http://www-d0.fnal.gov/Run2Physics/cs/index.html.

[34] Common analysis framework, http://www-d0.fnal.gov/Run2Physics/cs/caf.

[35] J. Pumplin et al., JHEP **0207**, 012 (2002).

[36] T. Sjöstrand et al., Computer Phys. Commun. **135** (2001), arXiv:hep-ph/0010017.

[37] M. L. Mangano et al., JHEP **0307**, 001 (2003), arXiv:hep-ph/0206293.

[38] GEANT *Detector Description and Simulation Tool*, CERN Program Library Long Writeup W5013.

[39] J. K. B. Calpas and T. Yasuda, DØ Note 5939.

[40] T. G. J. Kraus and O. Atramentov, DØ Note 5691.

[41] Monte carlo for femtobarn processes, http://mcfm.fnal.gov/.

[42] The multijet samples used for determination of the misidentification rate are the standard QCD skims produced by the electron and photon identification group. For more information on the selection criteria and the description of the samples, see DØ Note 5761.

[43] A. Harel, DØ Note 4919.

[44] A. Harel and R. Wagner, DØ Note 4932.

[45] U. Baur and E. Berger, Phys. Rev. D **47**, 4889 (1993).

[46] *Parameterized Monte Carlo Simulation*, http://www-d0.fnal.gov/computing/MonteCarlo/pmcs/pmcs_doc/pmcs.html for more information.

[47] P. M. Nadolsky et al., Phys. Rev. D **78**, 013004 (2008).

[48] W. Beenakker et al., Phys. Rev. D **40**, 54 (1989).

[49] J. M. Campbell and R. K. Ellis, PRD **60**, 113006 (1999).

[50] T. Andeen et al., FERMILAB-TM-2365, 2007.

[51] C. Amsler et al., Phys. Lett. B **667**, 1 (2008 and 2009 partial update for the 2010 edition).

[52] G. Gounaris et al., CERN 96-01 , 525 (1996).

[53] R. S. K. Hagiwara, S. Ishihara and D. Zeppenfeld, Phys. Rev. D **48**, 2182 (1993).

[54] R. S. K. Hagiwara, S. Ishihara and D. Zeppenfeld, Phys. Lett. B **283**, 353 (1992).

[55] H. He et al., Phys. Rev. D **78**, 031701 (2008)).

[56] A. Belyaev, arXiv:0711.1919 (2007).

[57] K.Agashe et al., arXiv:0810.1497[hep-ph] (2008).

[58] M. Perelstein, Prog. Part. Nucl. Phys. **58**, 247 (2007).

[59] W. v. N. R. Hamburg and T. Matsuura, Nucl. Phys. B **359**, 343 (1991), Erratum-ibid. B **644**, 403 (2002).

[60] T. Rizzo, J. High Energy Phys. **0705**, 037 (2007), arXiv:0704.0235 [hep-ph].

[61] W. Fisher, FERMILAB-TM-2386-E.

[62] T. Junk, Nucl. Instrum. Methods A **434**, 435 (1999).

[63] A. Read, *Modified Frequentist Analysis of Search Results (The CL_s Method)*, 2000.

[64] K. Lane and S. Mrenna, Phys. Rev. D **67**, 115011 (2003).

[65] V. Abazov et al., Phys. Rev. Lett. **104**, 061801 (2010), arXiv:0912.0715v3 [hep-ex].

[66] *The Large Hadron Collider*, http://public.web.cern.ch/public/en/lhc/lhc-en.html.

[67] V. Khachatryan et al., *CMS Physics TDR: Volume I (PTDR1), Detector Performance and Software*, 2006, (CMS Collaboration).

[68] *Measuring Electron Efficiencies at CMS with Early Data*, CMS PAS EGM-07-001, (CMS Collaboration).

[69] *Observation of WZ production*, PAS EWK-08-003, (CMS Collaboration).

[70] K. Kaadze, for CMS Collaboration, published in the conference proceedings of Moriond EW 2009, arXiv:0905.1877 [hep-ex].

Appendix A

Optimization of electron identification efficiency with the CMS detector

In this Appendix, studies of optimization of electron identification criteria for the future WZ production search at the CMS detector are briefly summarized. The CMS detector is one of two multipurpose detectors at the pp Large Hadron Collider (LHC)[66] that has started to operate just recently. The description of the CMS detector can be found elsewhere[67].

In preparation for the data analysis at CMS number of significant changes were introduced to improve reconstruction of electrons. The Kalman Filter tracking algorithm has been replaced with Gauss Filter algorithm (GSF) which improved reconstruction for so-called GSF electrons. Unfortunately, due to some of these changes the probability of a jet with high electromagnetic energy content, so-called em-jet, to mimic an electron increased as well. As a result, the three electron final state in the WZ production is completely saturated by the $Z + jets \rightarrow 2e + jets$ process, and it does not contribute to a discovery potential of the WZ production at CMS. In order to change this situation, a more thorough investigation is needed to improve the discriminating power between electrons and em-jets at CMS. In this Appendix, a thorough study of discriminating power of standard CMS electron identification observables, developed by the CMS $e\gamma$ physics object group (POG), is described. An analysis of correlation between different observables is also performed. Finally, improved electron identification criteria that significantly help the discovery potential

of the WZ production with electrons in the final state are given at the end of this Appendix.

The studies were done using MC simulation of the WZ process, as a source of real electrons, and background processes that can produce misidentified electrons. Those are $Z + jets$, $W + jets$, $t\bar{t}$, and multijet productions. The first three processes were generated using ALPGEN generator interfaced with PYTHIA for hadronization and showering, while the last process together with the WZ production were generated entirely using PYTHIA generator. All Monte Carlo (MC) simulations are processed by GEANT software to simulate the CMS detector response.

The major background to WZ production at CMS is $Z + jets$ process, where one of the jets is identified as an electron from the W boson decay. The focus of this study is to develop powerful electron identification criteria that allow us to suppress $jet \rightarrow e$ misidentification.

A.1 Optimization of the electron selection criteria

Electron is reconstructed as a group of energy clusters, so-called super cluster (SC), in the electromagnetic calorimeter (ECAL) matched to a track from the CMS tracker. Electrons used in these studies must be within pseudorapidity range $|\eta| < 1.479$ (barrel) or $1.55 < |\eta| < 2.5$ (endap) of the ECAL and have momentum greater than 20 GeV. The efficiencies of identification criteria are measured with respect to the these initial requirements.

The focus of this study is to optimize officially available identification criteria for dentification of electrons from the Z and W boson decays, respectively. As standard observables used to identify electrons are usually strongly correlated between each other, a study of correlation is very important to keep the number of variables in the criteria to a minimum. This results in simpler selection criteria that are likely to work better in the initial CMS data taking conditions.

Based on different thresholds on identification variables, described in the following section, two simple selection criteria are defined. These criteria are referred to as "*Loose*" and "*Tight*" to select electrons from $Z \rightarrow ee$ and $W \rightarrow e\nu$ processes, respectively. The "*Loose*"

criteria is developed first by tuning the thresholds of some of the least correlated variables to keep the efficiency of each requirement high. The amount of correlation is estimated by changing the order of how the selection requirements are applied and re-evaluating the discriminating power of a given criterium. The "*Tight*" criteria is designed as the "*Loose*" with an additional requirement to improve the discriminating power. This is chosen to reduce possible systematic uncertainties and to make the process of extracting the efficiency from data easier.

A.1.1 Identification Variables

Variables that allow discriminating electrons from em-jets can be roughly divided into two classes: matching/shower shape and isolation discriminants. The variables are described below.

Track-ECAL Matching

The separation between a ECAL SC and a track is used to discriminate genuine electrons from em-jets. Em-jet can also produce energy cluster in ECAL due to, for instance, $\pi^0 \to \gamma\gamma$ decay that can be matched to a random track from charged hadron, *e.g.* $\pi^{\pm}$, in the jet. However, in this case the matching quality is expected to be worse than in case of genuine electrons. Therefore, for electron identification, matching in azimuthal and pseudorapidity planes are used and those are denoted as $\Delta\phi$ and $\Delta\eta$, respectively.

ECAL Energy Cluster Width

An electron brems extensively in the CMS tracker, which results in a rather wide shower in azimuthal plane due to a strong magnetic field. However, the width of a shower in pseudorapidity plane remains very narrow and can discriminate against jets, which tend to create rather large clusters in both η and ϕ directions. Two parameterization of the shower width are considered in this study. The first one, used in official electron identification developed by $e\gamma$ POG, is $\sigma_{\eta\eta} = \sqrt{cov_{\eta\eta}}$. It describes the width of the highest-energy cluster

of the SC, further referred to as a seed cluster. The second one is an energy-weighted width of SC in η direction, defined as follows:

$$\sigma_\eta = \frac{1}{E_{SC}} \sqrt{\sum_{i}^{N_{SCRecHits}} E_i(\eta_i - \eta_{SC})^2}, \tag{A.1}$$

where the summation is done over ECAL reconstructed hits contained in the super cluster.

E/p-based Variables

An electron deposits almost all of its energy in the ECAL, thus the track momentum at the outer edge of the tracker, p_{out}, should be similar to the energy of the seed of SC, E_{seed}. A jet is reconstructed combining information from the CMS tracker and the hadronic calorimeter (HCAL). It interacts with the ECAL much less intensively and most of its energy, carried after the tracker, is deposited in the HCAL. Hence, p_{out} and E_{seed} differ significantly for jets and can be used to discriminate them from electrons. A similar variable is also considered, used in official identification criteria, E/p, where E is a SC energy, and p is the initial momentum of a charged particle.

H/E-based Variables

One can form a powerful discriminant by using the HCAL and ECAL energies associated with an electron candidate, as the electron tends to deposit very little or no energy in the HCAL, while jet produces a wide energy deposition in the HCAL due to the hadron content. A variable used in official $e\gamma$ POG identification criteria is H/E. It peaks around 0 for electrons and can be quite large for em-jets. One can also define a variable that takes into account the width of the ECAL energy deposition by making a ratio of the energy deposited in the HCAL and ECAL in the cone of $\Delta R < 0.3$, excluding the SC energy, normalized to the SC energy as follows

$$EmHad = \frac{1}{E_{SC}} \left(\sum_{\Delta R=0.3} E^{ecal}_{RecHit} + \sum_{\Delta R=0.3} E^{hcal}_{RecHit} - E_{SC} \right). \tag{A.2}$$

This variable is also sensitive to the energy deposition profile, and thus, usually in considered a mix between isolation and identification discriminant.

Track Isolation

As electrons from the W and Z boson decays are isolated, the requirement of isolation from tracking activity can significantly suppress em-jets that usually contain a large number of soft tracks. This requirement can also discriminate from real electrons originated via semi-leptonic decays of heavy quarks which tend to be non-isolated as well. Several definitions of the track isolation requirements are considered using tracks around the electron candidates. Those are

$$Iso^{trk}_{Norm} = \frac{1}{p^e_T}\left(\sum_{\Delta R=0.3} p_T(trk) - \sum_{\Delta R=0.05} p_T(trk)\right) \tag{A.3}$$

and non-normalized version of the above

$$Iso^{trk} = \sum_{\Delta R=0.3} p_T(trk) - \sum_{\Delta R=0.05} p_T(trk) \tag{A.4}$$

In this study, the performance of track isolation discriminant with the larger radius of outer cone, such as $\Delta R = 0.6$, is also checked:

$$Iso^{trk}_{EWK} = \sum_{\Delta R=0.6} p_T(trk) - \sum_{\Delta R=0.02} p_T(trk) \tag{A.5}$$

A.1.2 Tuning the "*Loose*" criteria

The distribution of the $\Delta\eta$ and $\Delta\phi$ for signal and background, together with the em-jet rejection power are shown in Figs. A.1 and A.2. The optimal thresholds for "*Loose*" criteria are 0.009 (0.007) and 0.05 (0.05) for $\Delta\eta$ and $\Delta\phi$ for barrel (endcap), respectively.

The third discriminating variable selected in "*Loose*" identification criteria uses the width of EM shower. Comparisons of discriminating power of the different shower width variables defined in Section A.1.1 are shown in Fig. A.3.

As it can be seen, the $\sigma_{\eta\eta}$ variable is more powerful in barrel that can reject ∼70% of em-jets while loosing only a couple of percents of signal. The performance in endcap is

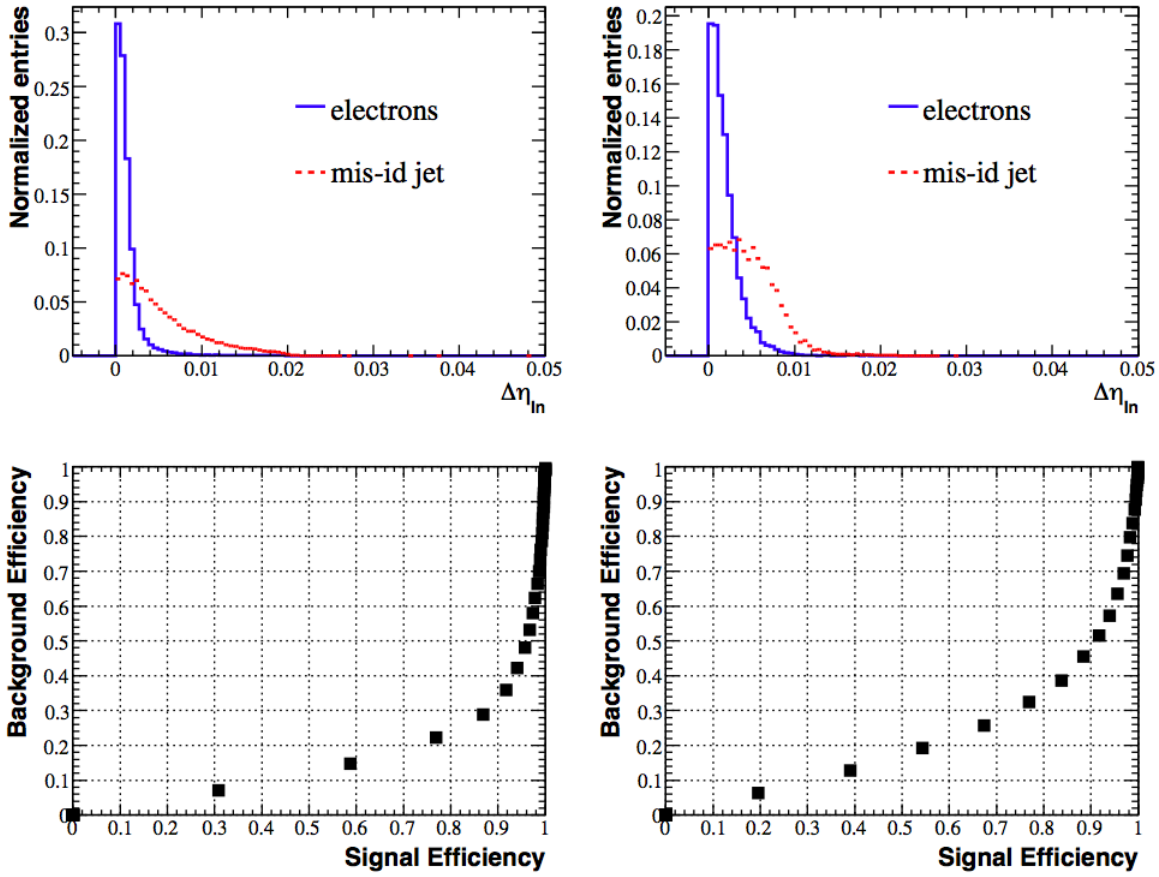

Figure A.1: *Distributions of $\Delta\eta$ for electrons (blue solid line) and misidentified jets (red dashed line) in barrel (top left) and endcap (top right). The performance of these discriminants in terms of efficiencies to select genuine electrons and misidentified jets are given below.*

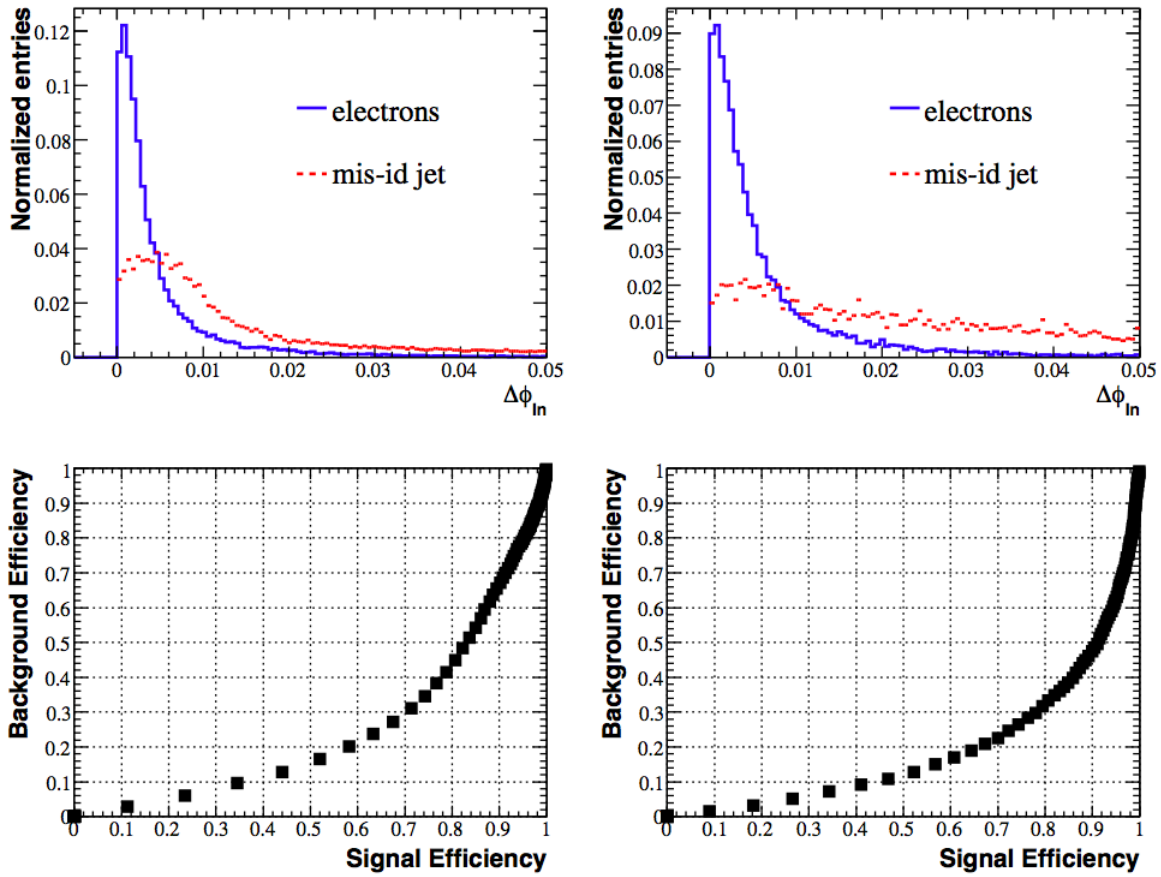

Figure A.2: *Distributions of $\Delta\phi$ for electrons (blue solid line) and misidentified jets (red dashed line) in barrel (top left) and endcap (top right). The performance of these discriminants in terms of efficiencies to select genuine electrons and misidentified jets are given below.*

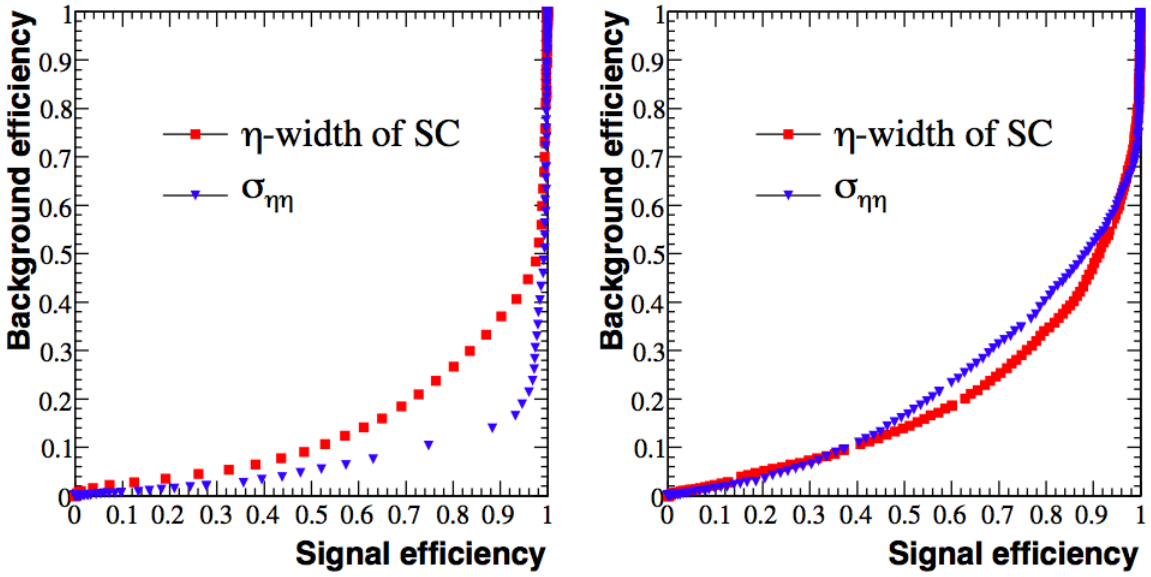

Figure A.3: *The background efficiency v.s. signal efficiency in barrel (left) and endcap (right) for η width of SC (red) and $\sigma_{\eta\eta}$ (blue).*

comparable between the two. Therefore, $\sigma_{\eta\eta}$ is chosen with thresholds $\sigma_{\eta\eta}$ <0.012 (0.026) for barrel (endcap). The distribution of $\sigma_{\eta\eta}$ in barrel and endcap and the performance are shown in Fig. A.4

As the next step, the E_{seed}/p_{out} and E/p discriminants, defined in Section A.1.1 are studied in the similar way. The results are shown in Fig. A.5. The E_{seed}/p_{out} has a better performance, and it is included to the "*Loose*" criteria with a requirement to be greater than 0.9 for both barrel and endcap. The distribution of this variable and efficiencies are shown in Fig. A.6.

It is possible to further improve the performance of the "*Loose*" identification by applying track isolation requirements, defined in Section A.1.1. These are studied in details by comparing the discriminating power for different cone sizes, varied from 0.5 to 0.05. The results are given in Fig. A.7.

The normalized track isolation variable, Iso^{trk}_{Norm}, offers the best performance, with an expense of making the efficiency to depend on the electron candidate p_T. That results in a

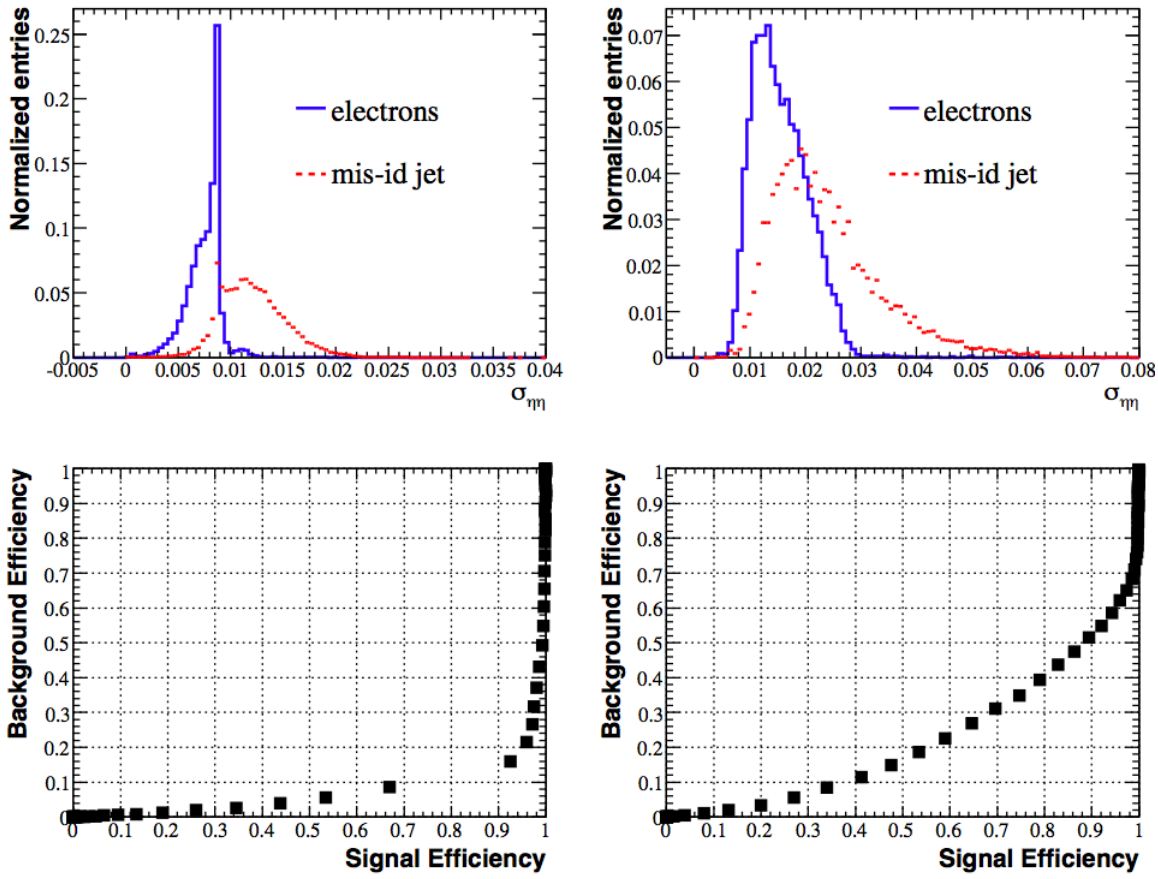

Figure A.4: *Distributions of $\sigma_{\eta\eta}$ for electrons (blue solid line) and misidentified jets (red dashed line) in barrel (top left) and endcap (top right). The performance of this discriminant in terms of efficiencies to select genuine electrons and misidentified jets are given below.*

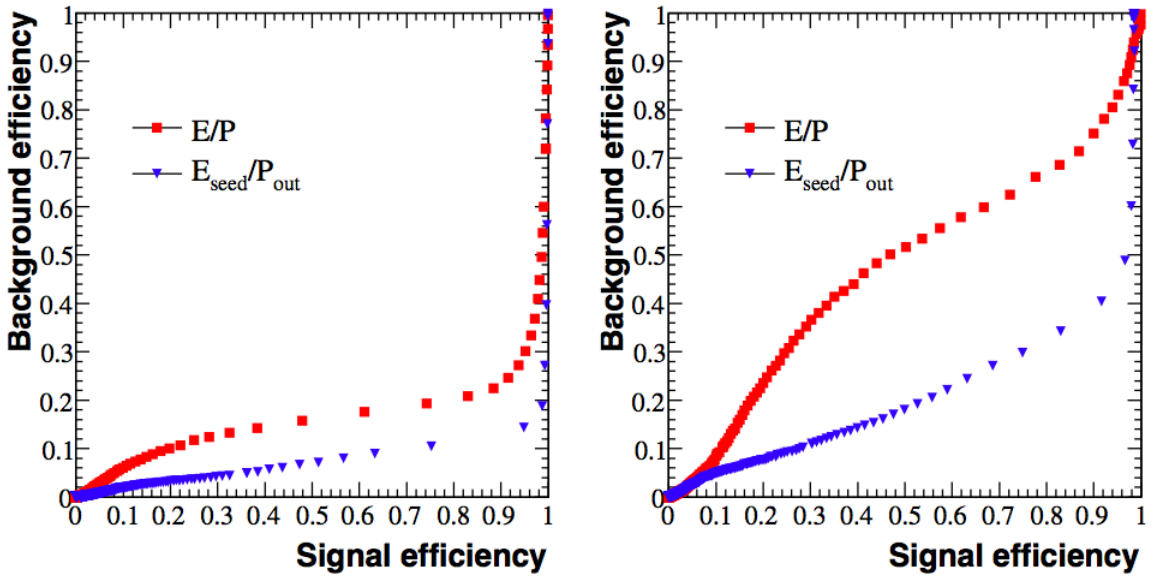

Figure A.5: *Background v.s. signal efficiency for barrel (left) and endcap (right) for E/p (red) and E_{seed}/p_{out} (blue).*

loss of efficiency at low p_T. However, the inefficiency is small for the p_T range characteristic to electrons from the heavy gauge boson decays. By introducing the isolation requirement, a significant background is rejected due to real non-isolated electrons produced from semi-leptonic decays of heavy flavor quarks, *e.g.* in $Zb\bar{b}$ production. The distribution of Iso^{trk}_{Norm} for signal electrons, misidentified light and heavy quark jets are given in Fig. A.8. The performance of track isolation variable chosen for "*Loose*" criteria is illustrated in Fig. A.9. The threshold for this requirement is chosen to be less than 0.1 and 0.2 for barrel and endcap, respectively.

A.1.3 Tuning the "*Tight*" criteria

The "*Loose*" criteria utilize variables that describe spatial- and energy-matching of a track to a SC, lateral energy deposition profile of a SC, and a track isolation requirement. Although, these requirements are sufficient to select a relatively clean sample of $Z \rightarrow ee$ events, the discriminating power is insufficient to suppress the background from misidentified jets from

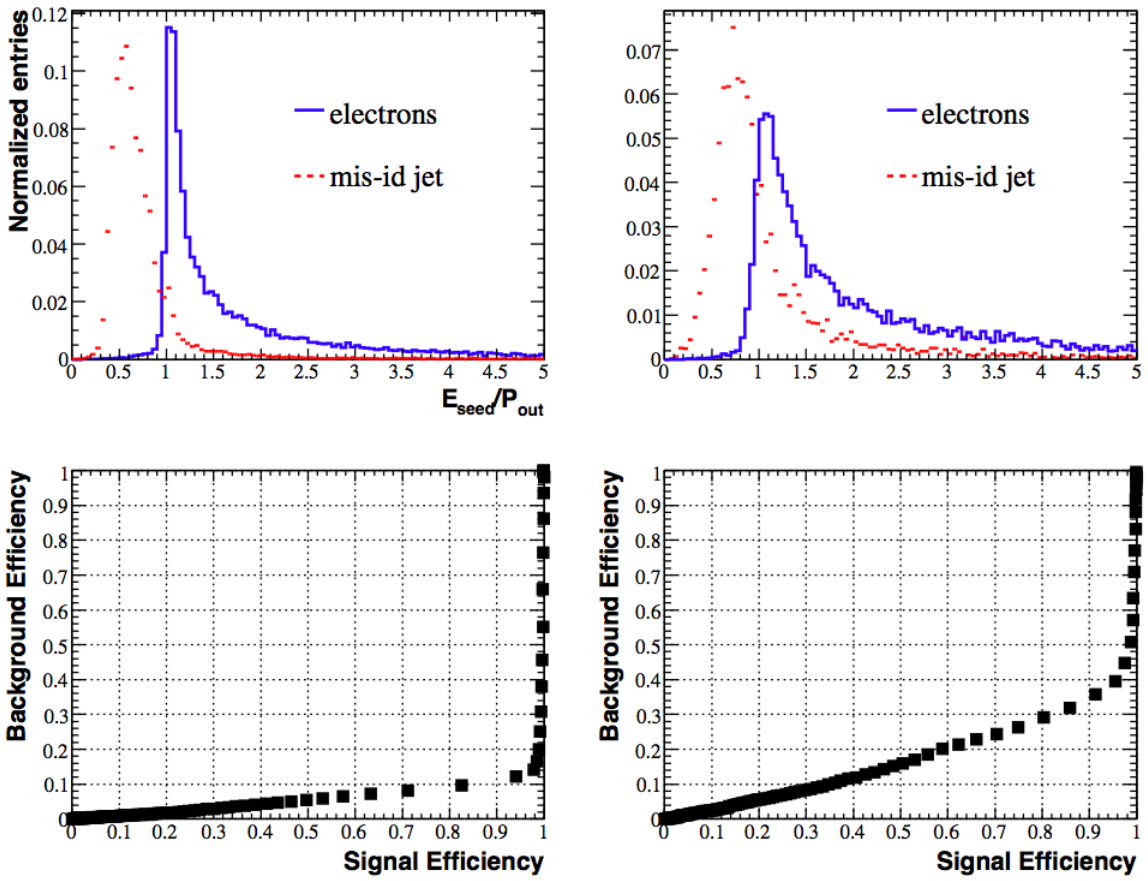

Figure A.6: *E_{seed}/p_{out} for electrons (blue solid line) and mis-identified jets (red dashed line) in barrel (left top) and endcap (right top). The performance of this variable for different thresholds is given in the bottom left plot for barrel, and bottom right plot for endcap.*

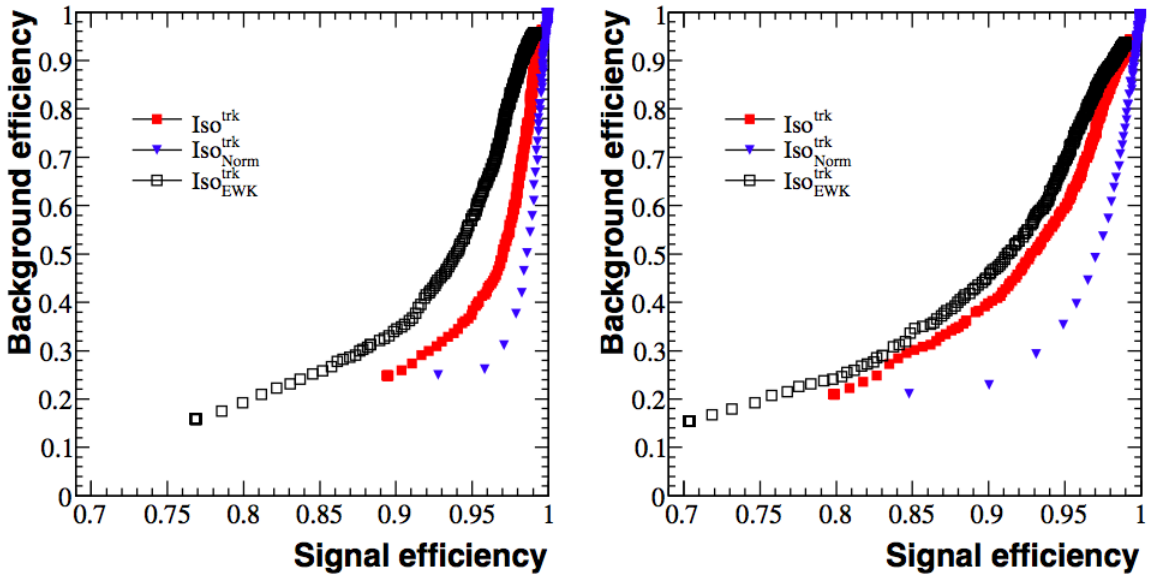

Figure A.7: *Performance of three track isolation variables for barrel (left) and endcap (right).*

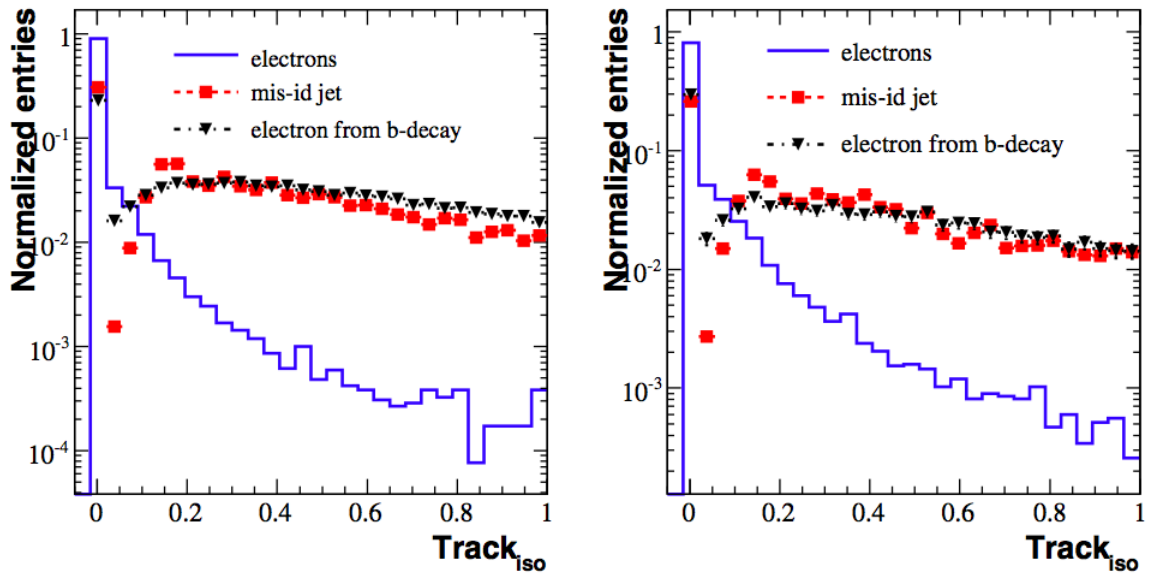

Figure A.8: *The distribution of the normalized track isolation defined in Eq. A.3 for signal electrons (blue solid line), misidentified light quark jets (red squares), and b quark jets (black inverted triangles) in barrel (left) and endcap (right).*

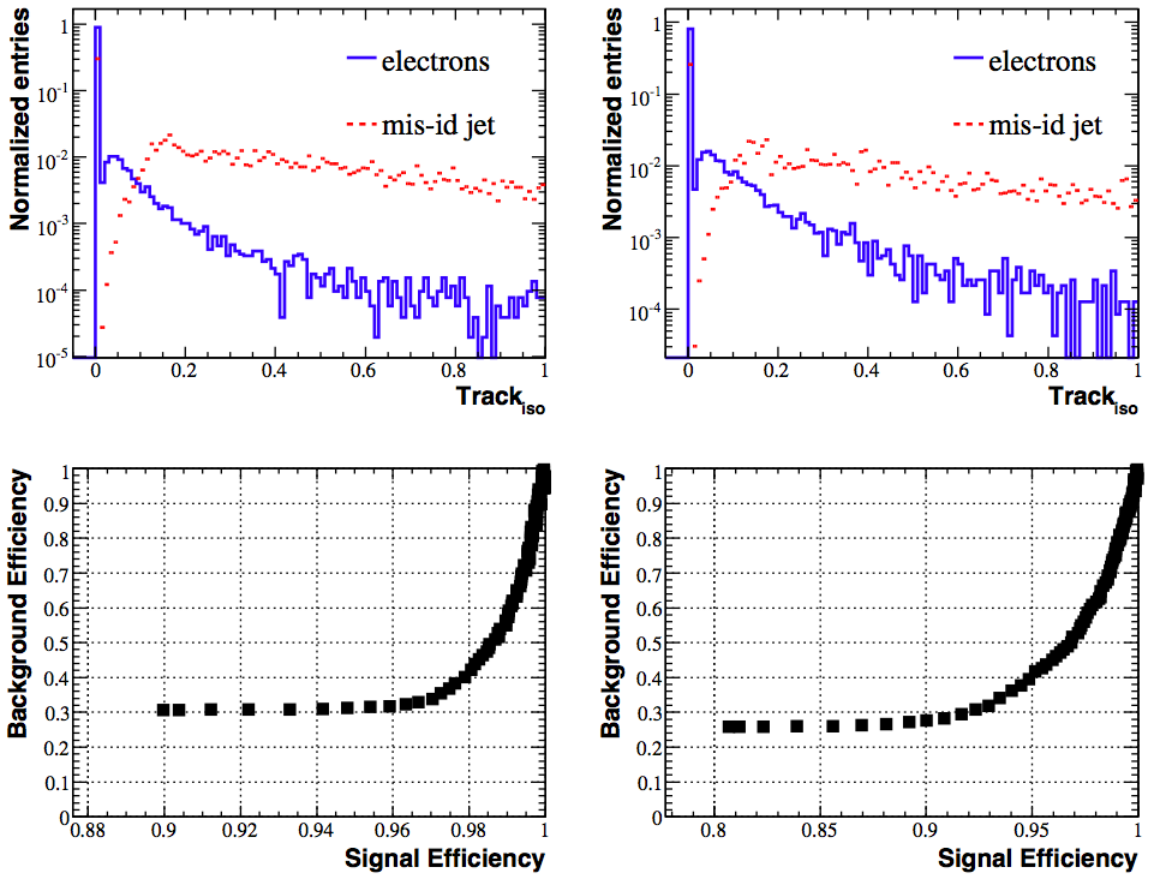

Figure A.9: *The Iso^{trk}_{Norm} discriminant for electrons (blue solid line) and misidentified jets (red dashed line) for barrel (top left) and endcap (top right). The signal v.s. background efficiencies obtained by varying the threshold are displayed in bottom left (barrel) and bottom right (endcap) plots.*

the $Z + jets$ processes. Therefore, a "*Tight*" criteria is introduced, that is based on the "*Loose*" selection with an addition of the requirement that takes into account the energy deposition in the HCAL.

The variable that is used by the official $e\gamma$ POG criteria is H/E. A $EmHad$ variable defined in Eq. A.2 is also studied, which is a mix of H/E and an HCAL+ECAL isolation in a relatively narrow cone of $\Delta R < 0.3$. As expected, these two variables are found to be correlated, although the $EmHad$ has much stronger discriminating power (see Fig. A.10), due to an additional requirement on the lateral energy profile in the 0.3 cone.

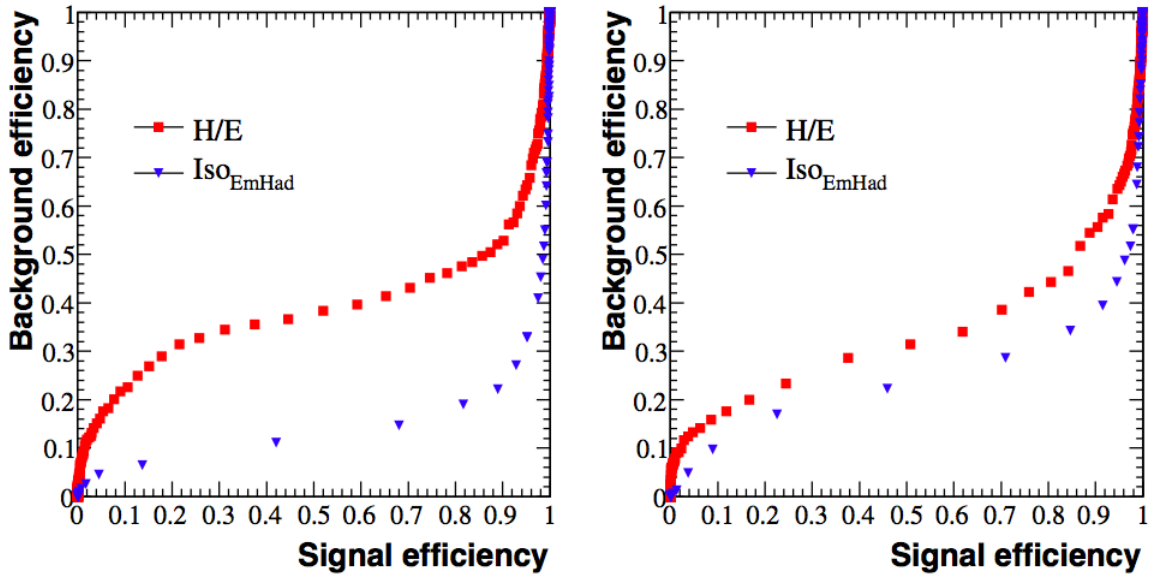

Figure A.10: *The H/E and EmHad variables for barrel (left) and endcap (right).*

The threshold of $EmHad < 0.18$ (0.1) for barrel (endcap) is used in "*Tight*" criteria (see Fig. A.11). Applying additional ECAL or HCAL isolation criteria after the "*Tight*" selection does not result in any substantial improvement in performance. Thus, $EmHad$ and track isolation requirements are sufficient to identify the isolated electrons in the p_T range corresponding to the W and Z boson decay products.

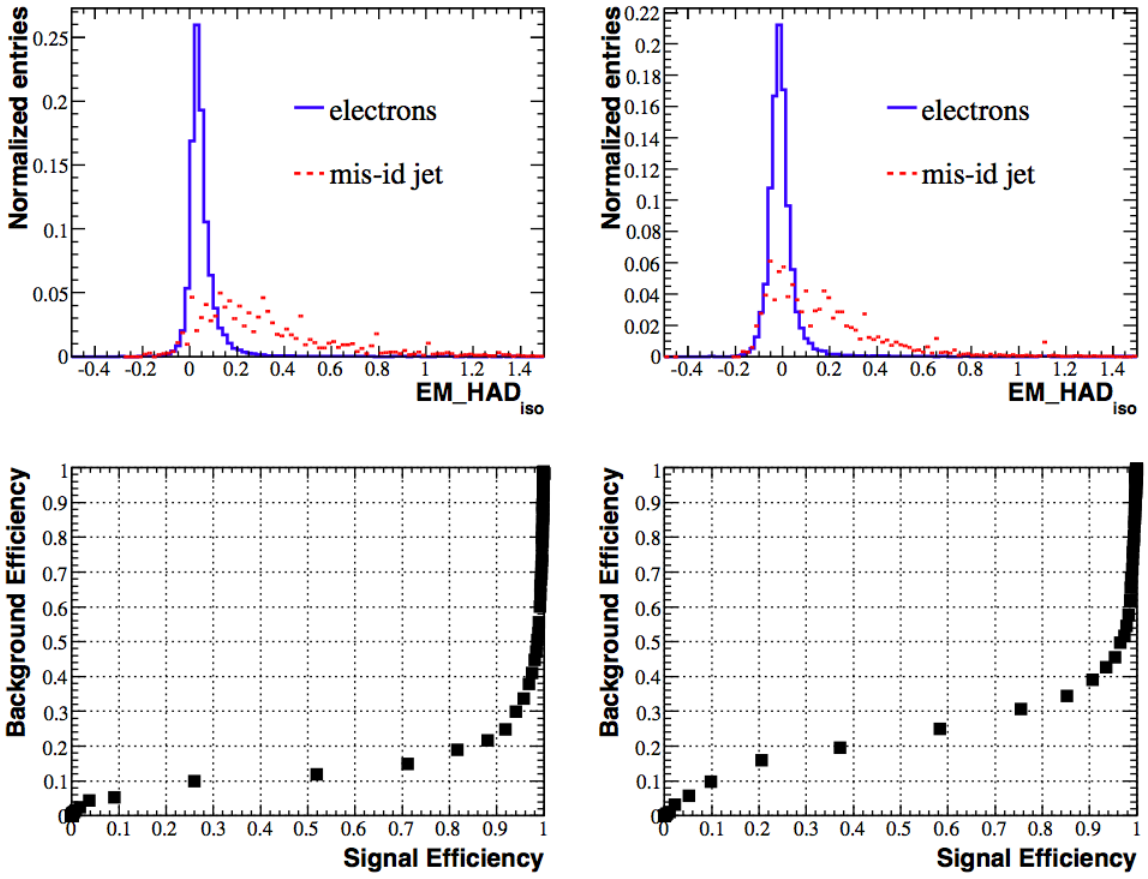

Figure A.11: *The EmHad for electrons (solid blue line) and mis-identified jets (red dashed line) in barrel (top left) and endcap (top right). The performance of the discriminator is given below for barrel (bottom left) and endcap (bottom right).*

A.2 Summary of Electron Identification

To summarize, "*Loose*" and "*Tight*" criteria are simple cut-based selections, that utilize some of the discriminants also used in official electron identification. Additional variables are also introduced and the thresholds on all discriminants are optimized in order to retain high signal efficiency and remove significant background due to misidentified jets. The "*Loose*" criteria is efficient to select electrons from the Z boson decay. The "*Tight*" selection differs from the "*Loose*" by one additional requirement. As a result, this criteria has stronger discriminating power against jets and can effectively be used to identify electrons from the W boson decays. The thresholds for barrel and endcap selection criteria are summarized in Table A.1.

Variables	Barrel	Endcap
"*Loose*"		
$\Delta\eta <$	0.009	0.007
$\Delta\phi <$	0.005	0.005
$\sigma_{\eta\eta} <$	0.012	0.026
$E_{seed}/p_{out} >$	0.9	0.7
$Iso^{trk}_{Norm} <$	0.1	0.2
"*Tight*"		
$EmHad <$	0.18	0.1

Table A.1: *The thresholds used in "Loose" and "Tight" criteria in barrel and endcap.*

Appendix B

Study of the Process $pp \to WZ \to \ell\nu\ell\ell$ with the CMS detector

An estimation of the sensitivity reach for observation of the WZ boson pair production at CMS in pp collisions at center-of-mass energy of 14 TeV is described.

Four experimental signatures of WZ decays are considered:

- $W \to e\nu$ and $Z \to ee$
- $W \to \mu\nu$ and $Z \to ee$
- $W \to e\nu$ and $Z \to \mu\mu$
- $W \to \mu\nu$ and $Z \to \mu\mu$

The major instrumental background to all four signatures is due to misidentified $jet(s)$ from associated production of $jet(s)$ and the Z boson. The $W+jets$ and $t\bar{t}$ processes are also considered but their contribution to $3\ell + \not{E}_T$ final state is found to be small. An additional background to WZ signal process arises due to the ZZ production with one of the leptons being mis-reconstructed or lost and the $Z\gamma$ process where a photon converts and produces a genuine electron. Both the WZ signal and background MC samples are processed with the full simulation of the CMS detector.

One of the major goals of this MC-based analysis is to meet all the recent updates and changes in the lepton identification at CMS. The lepton selection must have a high efficiency

for identifying genuine leptons from heavy boson decays and effectively suppress non-isolated leptons from heavy quark decays as well as other objects misidentified as leptons. In addition to this, the data-driven techniques are developed to estimated major instrumental background. These are going to play an important role in establishing the WZ signal with early data when the CMS experiment starts.

B.1 Identification of Final State Leptons and Event Selection

Electron candidates from the Z and W boson decays of the signal process are identified as "*Loose*" and "*Tight*", respectively. The details of these criteria are given in Table A.1.

Muon candidates are identified as a track reconstructed in the CMS muon detector matched to a track reconstructed in the CMS central tracker. To suppress non-isolated muons from heavy quark decays muons must be isolated in both central tracker and calorimeter. The track and calorimeter isolation are defined as follows

$$Iso_{\mu}^{trk} = \sum_{\Delta R=0.25} p_T(trk) - p_T(\mu) \tag{B.1}$$

$$Iso_{\mu} = \sum_{\Delta R=0.3} E_{RecHit}^{ecal} + \sum_{\Delta R=0.3} E_{RecHit}^{hcal} - E_{\mu} \tag{B.2}$$

The requirements of $Iso_{\mu}^{trk} < 2$ GeV and $Iso_{\mu} < 5$ GeV are applied to select muons from heavy gauge boson decays. The significance of the muon impact parameter in the transverse plane, also called as distance of closest approach, is additional discriminator against muons from heavy-quark decays. This variable is defined as $S_{IP} = IP/\sigma_{IP}$ and it is required to be smaller than 3.

The WZ events are selected by electron and/or muon triggers. Efficiency of the trigger requirement is $\approx 98\% \pm 2\%$. The events are accepted if they contain at least three charged leptons, electrons or muons, with $p_T > 15$ GeV and within acceptance of the calorimeter ($|\eta| < 2.5$) and muon detector ($|\eta| < 2.4$). The leptons must satisfy the identification

criteria described above. Out of all possible same-flavor and opposite-charge lepton pairs in the event the Z candidate is formed and event is retained if invariant mass of the Z boson candidate is within 50 and 120 GeV window. If more than one Z candidate is found in an event within 20 GeV window around the genuine Z boson mass the event is rejected. The pair of leptons with invariant mass with the smallest deviation from the Z boson mass is selected as the Z boson decay product. The highest p_T lepton out of the remaining leptons in the event is selected as a lepton from the W boson decay. This lepton must have a transverse momentum greater than 20 GeV. Additional isolation is applied for $2e1\mu$ and $2\mu1e$ signatures by requiring the spatial separation between electron and muon candidates of $\Delta R > 0.1$.

To further suppress events from background processes, an additional requirement of the transverse mass of the W boson candidate is imposed. The transverse mass is calculated as follows

$$M_T(W) = \sqrt{2\not{E}_T E_T^l (1 - cos(\Delta\phi_{\not{E}_T,l}))} \tag{B.3}$$

The distribution of W transverse mass for signal and background precesses is shown in Fig. B.1. Events are selected with the requirement $M_T(W) > 50$ GeV.

The candidate Z boson invariant mass after application of the whole event selection is shown in Fig. B.2 for four signatures separately.

B.2 Background Estimation and Signal Extraction

The contribution from ZZ diboson process is estimated from MC simulation. A very conservative 100% uncertainty on contribution from this process is assigned due to modeling of kinematics of the decay products. The $Z\gamma$ background is also estimated from MC. However, it can be determined from data once the final state radiation $Z\gamma$ signal is measured at CMS. 100% of systematic uncertainty is assigned on this background as well due to modeling the photon conversion probability. The background from processes without genuine Z boson, such as $W + jets$ and $t\bar{t}$, are estimated from MC simulation as well and found to contribute

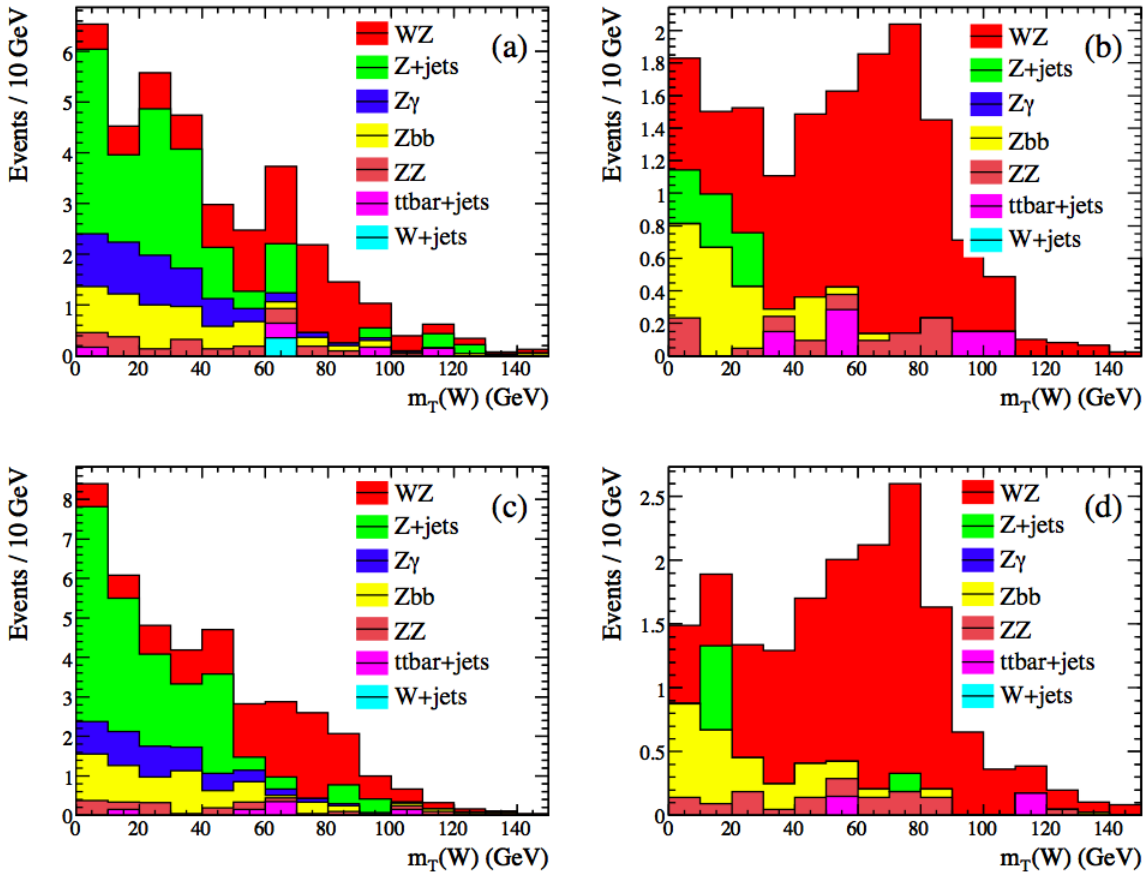

Figure B.1: *W transverse mass for 3e (a), 2e1μ (b), 2μ1e (c), and 3μ (d) categories. The distributions show the number of expected events for 300 pb^{-1}. Only events satisfying 81 $GeV < M_Z <$ 101 GeV are shown.*

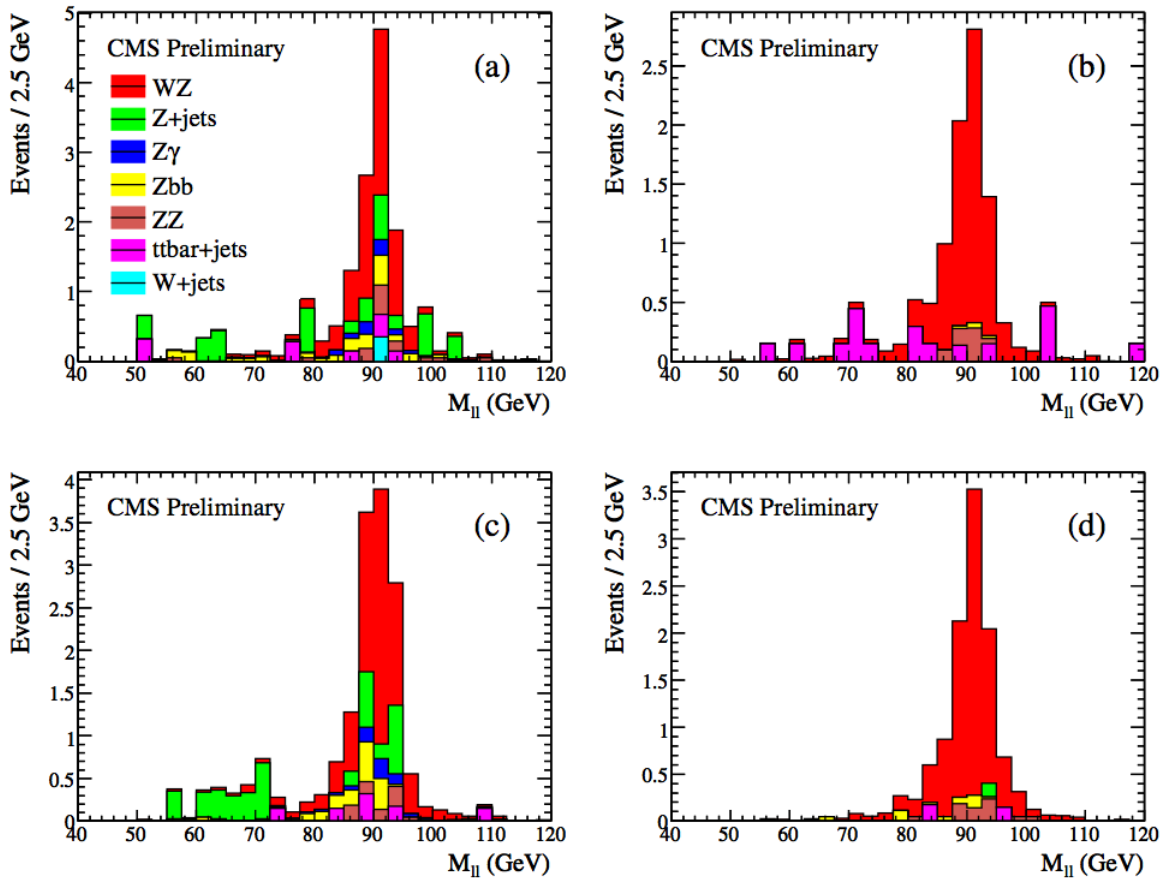

Figure B.2: *Z mass for* $3e$ *(a),* $2e1\mu$ *(b),* $2\mu1e$ *(c), and* 3μ *(d) channels. The distributions are normalized to integrated luminosity of 300* pb^{-1}.

at 6% level to the WZ signal.

A "*matrix method*" data-driven technique is used in this analysis to estimate the major instrumental background due to *jet* misidentification in $Z + jets$ processes. The idea of the method is to define two samples in data containing events with the Z candidate and an additional lepton. In the first sample the additional lepton is required to pass not very stringent criteria. In case of $Z + e$ sample electron must satisfy the "*Loose*" criteria. While for $Z + \mu$ sample muon must satisfy matching requirement between the tracker and the muon detector. The number of events in this sample, N_{loose}, consists of events with real isolated leptons, N_l, and events with misidentified jets, N_j.

$$N_{loose} = N_l + N_j \tag{B.4}$$

In the second sample more stringent criteria are applied on the third lepton that is "*Tight*" criteria for electrons and track and calorimeter isolation requirements for muons. That changes number of events in the sample to N_{tight}, defined as follows

$$N_{tight} = \epsilon_{tight} N_l + p_{fake} N_j. \tag{B.5}$$

Here ϵ_{tight} and p_{tight} are efficiencies of stringent criteria with respect to looser requirements for genuine isolated leptons and misidentified jets, respectively. The N_{loose} and N_{tight} are directly observable. To extract the number of $Z + jets$ events in the final state sample, ϵ_{tight} and p_{tight} are measured in control data samples.

The ϵ_{tight} is measured using "$tag - and - probe$" method with $Z \to ee$ and $Z \to \mu\mu$ events. The method is described in[68]. The efficiency is estimated $\epsilon_{tight} = 0.98 \pm 0.01$ for both electrons and muons.

The probability of a jet to be misidentified as a lepton depends on p_T and η as well as on the composition of quarks and gluons in the jet. Although the light quarks and gluons have similar misidentification rate (see Fig. B.3) this can differ from heavy quark misidentification rates. Therefore, the p_{fake} is measured in the $W + jets$ sample which

has the same jet composition as $Z + jets$. Although the statistical uncertainty is going to dominate the precision of p_{fake} determination.

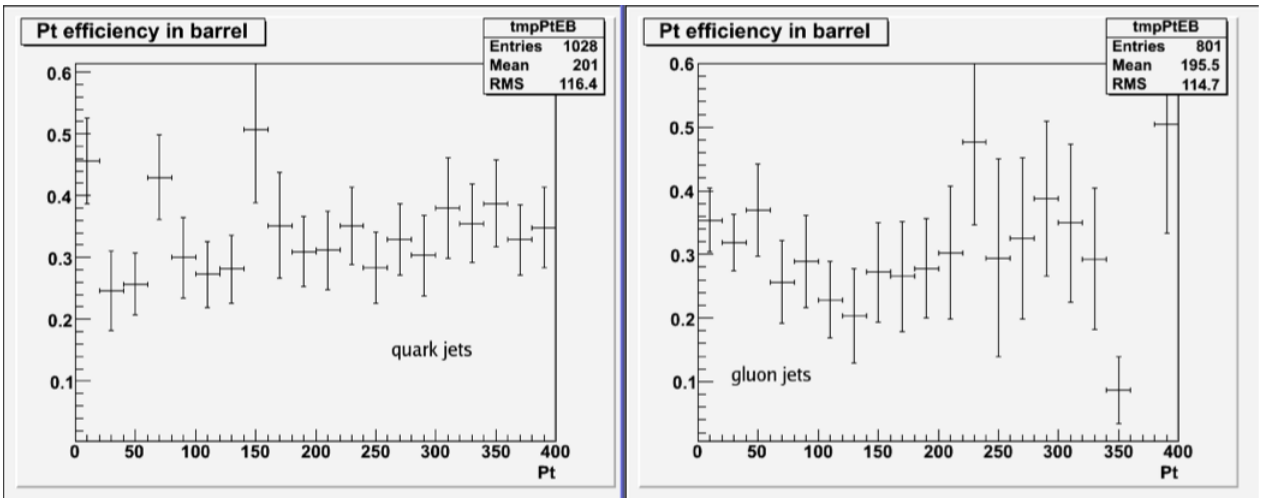

Figure B.3: *The misidentification probability p_{fake} measured in light-quark jets (left), and gluon jets (right) using multijet* ALPGEN *Monte Carlo simulation.*

To measure p_{fake} for electrons following selection criteria are applied on $W + jets$ events:

- event must be triggered by the single muon trigger
- event must not have the Z boson candidate with an invariant mass between 50 and 120 GeV
- event must have a muon candidate with $p_T > 20$ GeV within the acceptance of muon detector satisfying isolation and S_{IP} requirements; the transverse mass of the muon candidate and the $\not\!\!E_T$ in the event must greater than 50 GeV
- event must have only one electron candidate with $p_T > 20$ GeV satisfying "*Loose*" identification requirements and being isolated from the muon candidate by $\Delta R > 0.1$
- muon and electron must have the same charge to suppress $t\bar{t}$ events with real muon and electron from the W boson decays

The probability p_{tight} is then measured as the ratio of the p_T distribution of the electron candidates in this sample that also satisfy "*Tight*" criteria to the p_T distribution of the "*Loose*" quality electrons. This probability is shown in Fig. B.4. The uncertainties correspond to the statistics expected for data sample with integrated luminosity of 300 pb^{-1}. Thus, it is possible to extract p_{fake} with $\sim 10\%$ accuracy with early CMS data. A similar method can be used to extract the p_{fake} for the muons as well.

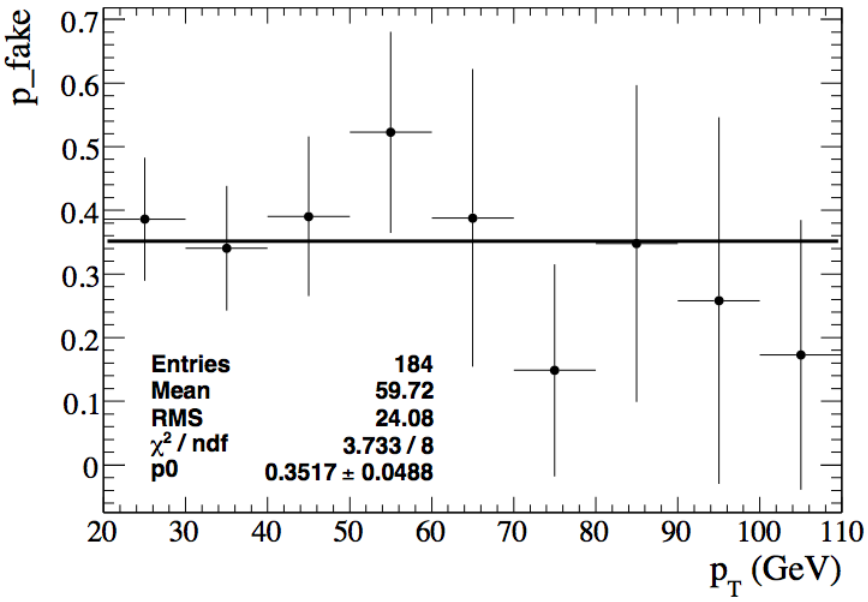

Figure B.4: *The probability that a misidentified jet, satisfying "Loose" electron identification requirement, will also pass "Tight" criteria.*

The obtained p_{fake} is further compared with p_{fake} measured in multijet sample samples. Both values agree with each other within statistical uncertainties and equal to $p_{fake} = 0.32 \pm 0.04$ for electrons and $p_{fake} = 0.08 \pm 0.01$ for muons.

Using the values of ϵ_{tight} and p_{fake} the system of Eqs. B.4 and B.5 is solved, and an estimate of background events from the $Z + jets$ processes, N_j, is calculated. The results of this method are shown in Table B.1, and they agree well with the expected background events from the Monte Carlo truth information.

	$3e$	$2e1\mu$	$2\mu1e$	3μ
$N - ZZ - Z\gamma - W + jets - t\bar{t}$	11.1 ± 1.3	8.2 ± 0.9	12.1 ± 1.2	10.5 ± 0.8
$N^{genuineZ}$ (matrix method)	3.2 ± 1.7	0.6 ± 0.8	4.6 ± 2.0	0.6 ± 0.9
N^{WZ}	7.9 ± 2.1	7.6 ± 1.2	7.5 ± 2.3	10.0 ± 1.2
WZ from MC	7.9	8.1	9.0	10.1

Table B.1: *Expected number of events for 300 pb^{-1} of integrated luminosity for signal and estimated background for 81 GeV $< M_Z <$ 101 GeV using data-driven technique. Uncertainties are systematic, associated with the background subtraction method only.*

B.3 Signal Significance

The distribution of the Z boson candidate invariant mass for all four channels combined after applying the final selection is shown in Fig. B.5.

To estimate the amount of data necessary to claim an evidence or observation of the WZ signal at CMS, 500,000 pseudo-experiments are performed for a given value of data that is varied from 100 to 500 pb^{-1}. For each pseudo-experiment a Poisson statistics is used to estimate the expected number of events for signal and for each background process separately, for each final state signature. The mean of the expected number of signal and background events is varied within systematic uncertainties following the Gaussian statistics. The significance of the signal in each pseudo-experiment is calculated using the likelihood ratio

$$S_L = \sqrt{2lnQ}, \text{ where } Q = \left(1 + \frac{N_S}{N_B}\right)^{N_S+N_B} e^{-N_S}. \tag{B.6}$$

Here, N_S and N_B are the expected number of signal and background events observed each signature. By summing the signal and background in four channels, no correlation are assumed between the channels which result in a conservative estimation of the sensitivity reach. However, the early re-discovery of the WZ signal is going to be done with very limited statistics, which makes correlations in systematic uncertainty negligible.

The distribution of S_L for a given luminosity is fitted with Gaussian function. The resultant mean and resolution width correspond to the most probable value of S_L and its uncertainty. The 68% and 95% C.L. bands around the mean are $\pm1\sigma$ and $\pm1.96\sigma$, respec-

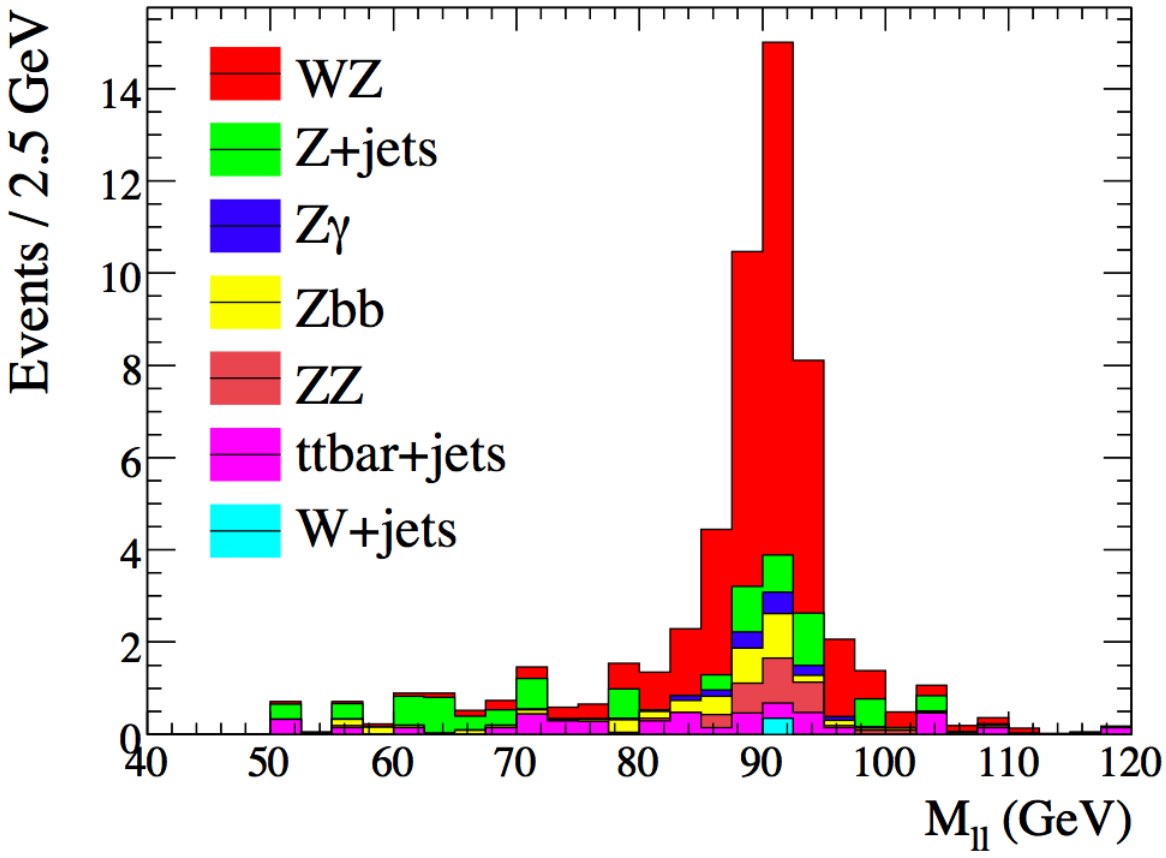

Figure B.5: *Expected Z candidate invariant mass distribution for the data set equivalent to 300 pb^{-1} of integrated luminosity.*

tively. To study the effect of the systematic uncertainties in this estimation all systematic uncertainties are doubled, and the limits are recalculated with new systematic uncertainties. The results are given in Fig. B.6 with four experimental signatures combined without taking into account any correlation between the channels. A 5σ significance of the WZ signal can be established with data equivalent from 100 to 350 pb^{-1} of integrated luminosity at 95% C.L.

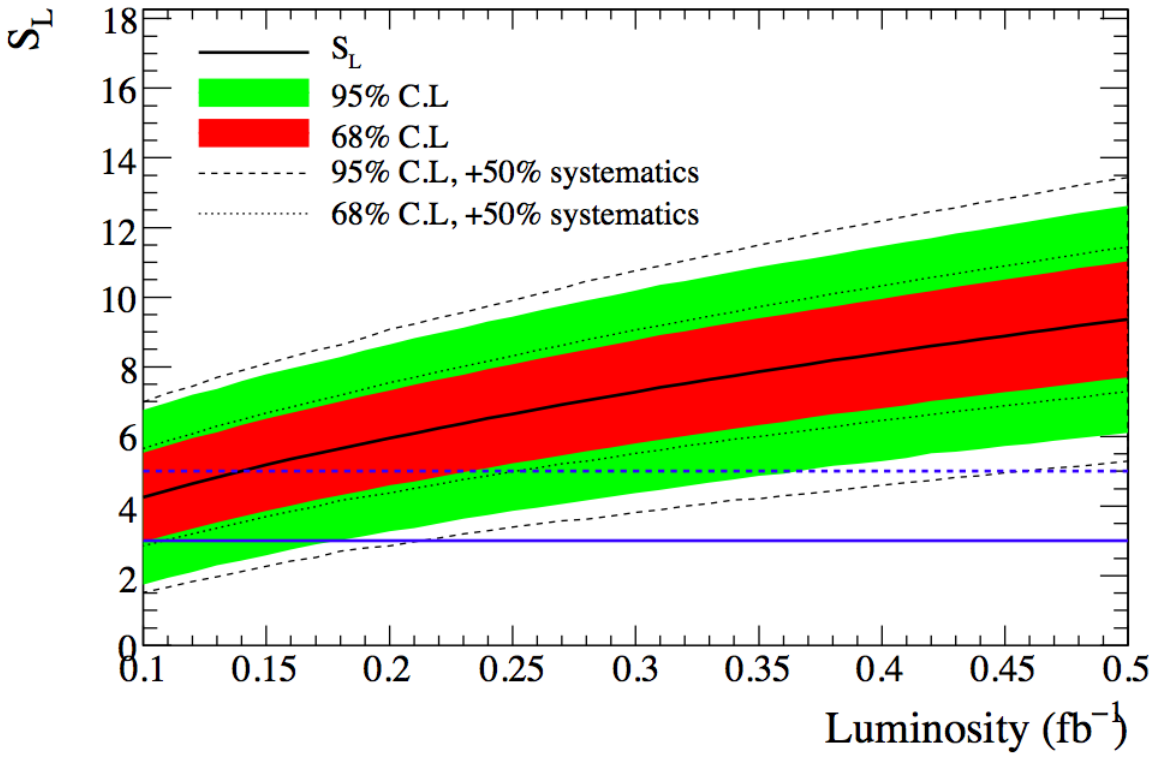

Figure B.6: *Expected value of S_L (black line) and its 68% (red band) and 95% (green band) C.L. bands as a function of integrated luminosity. The dotted and dashed lines correspond to 68% and 95% C.L. bands calculated for the case when the systematic uncertainty is twice as much as estimated.*

B.4 Conclusion

In summary, the methods to establish the $pp \to WZ \to \ell\nu\ell\ell$ ($\ell = e,\ \mu$) signal at CMS experiment using early data are developed. The MC sample of the signal and background

processes with the full simulation of the CMS detector are used. The event selection criteria are optimized in order to select events with three charged leptons and significant missing transverse energy. The major studies are done to improve electron identification criteria and reduce $j \rightarrow e$ misidentification. For that, the different discriminating variables are considered and the correlation between those are checked. The variables with the least correlation and high discriminating power are selected and two simple cut-based selections are developed in order to identify electrons from the Z and W boson decays. In addition to this, the data-driven techniques are developed to estimate the major instrumental background from $Z + jets$ processes. The sensitivity for the observing the WZ production at 95% C.L. is estimated as a function of integrated luminosity. It is shown that the 5σ significance of the signal can be achieved with less than 400 pb^{-1} of integrated luminosity of data. These studies are documented and published in here[69,70].